Doctoral theses at NTNU, 2019:106

Hans Kristian Hygen Meyer

Dielectric barriers under lightning impulse stress

Breakdown and discharge-dielectric interaction in short non-uniform air gaps

Doctoral thesis

Hans Kristian Hygen Meyer

ISBN 978-82-326-3810-9 (printed ver.)
ISBN 978-82-326-3811-6 (electronic ver.)
ISSN 1503-8181

NTNU
Norwegian University of
Science and Technology

NTNU
Norwegian University of Science and Technology
Thesis for the Degree of
Philosophiae Doctor
Faculty of Information Technology and Electrical
Engineering
Department of Electric Power Engineering

Doctoral theses at NTNU, 2019:106

NTNU
Norwegian University of
Science and Technology

Hans Kristian Hygen Meyer

Dielectric barriers under lightning impulse stress

Breakdown and discharge-dielectric interaction in short non-uniform air gaps

Thesis for the Degree of Philosophiae Doctor

Trondheim, April 2019

Norwegian University of Science and Technology
Faculty of Information Technology and Electrical Engineering
Department of Electric Power Engineering

NTNU
Norwegian University of
Science and Technology

NTNU
Norwegian University of Science and Technology

Thesis for the Degree of Philosophiae Doctor

Faculty of Information Technology and Electrical Engineering
Department of Electric Power Engineering

ISBN 978-82-326-3810-9 (printed ver.)
ISBN 978-82-326-3811-6 (electronic ver.)
ISSN 1503-8181

Doctoral theses at NTNU, 2019:106

Printed by NTNU Grafisk senter

Abstract

Dielectric-air insulation systems can reduce the carbon footprint of medium voltage switchgear, as they can replace SF_6-insulated systems. Such replacement is, however, not easy, as the devices are typically compact and complex, with strongly inhomogeneous electric fields. Withstand voltages are typically estimated with empirical models for discharge formation and propagation. Any dielectric surface can change the conditions for such evaluations, especially as the surfaces accumulate charge.

The aim of this work was to study the influence of dielectric surfaces on breakdown in non-uniform atmospheric air gaps. Short ($\leq$ 120 mm) rod-plane gaps with a polycarbonate barrier were used throughout. The development of pre-breakdown and breakdown processes were clarified with high-speed imaging, photomultipliers and fast current measurements. It was shown that breakdown around the 50 % level is governed by leader-like discharges rather than streamers.

Surface potential measurements demonstrated that streamers charge dielectric barriers in a way that is predictable with variations of saturation charge boundary conditions (zero or constant normal electric field at the air side of the interface). Such predictions allow utilization of beneficial surface charging effects in switchgear design.

Moreover, it was shown that drift-diffusion models can be used to simulate important discharge behaviour in dielectric-air insulation systems. Such models are computationally heavy, but can become useful for dielectric design of high voltage components as computer capabilities are improving. It was shown that 2D planar streamers charge dielectric surfaces to saturation within tens of ns. The streamer-exposed surface is charged mainly by drifting ions from the streamer channel, but also by electron emission processes from the dielectric surface.

The thesis is presented as a collection of seven peer-reviewed articles published in journals and conference proceedings, together with an overview document. The results presented in this thesis contribute to a better understanding on how dielectric barriers influence electrical breakdown in air.

Preface

The work in this thesis has been funded by the Research Council of Norway (RCN) and was carried out between August 2015 and December 2018, mainly at NTNU in Trondheim. Around four months of the time was spent on teaching duties at NTNU, and six months on course work. Parts of the thesis work were performed during a research stay in Switzerland at ABB Corporate Research Center (CHCRC) and HSR Rapperswil between November 2017 and April 2018.

The PhD work is a part of a research project, "Electrical insulation with low-GWP gases" (RCN project number: 245422), in collaboration with SINTEF Energy Research, ABB AS, Norway, and ABB Ltd., Switzerland.

Acknowledgement

This thesis work would not have been possible without the help of many people. I firstly want to thank Frank Mauseth at NTNU for being a very supportive and engaged supervisor. I also want to thank Atle Pedersen at SINTEF Energy Research for great co-supervising.

I have had access to many helpful people with interest and expertise. At SINTEF Energy Research, I especially want to thank Robert Marskar, Nina Sasaki Støa-Aanensen, Dag Linhjell and Lars Lundgaard. I would also like to thank the people in the mechanical workshop and service lab at NTNU, and MSc student Martine Husøy, who was a skilled companion in the lab.

Thank you to Jonas Ekeberg from ABB CHCRC for the great collaboration early on in the PhD. At the end of my PhD, I had the opportunity to work five months at ABB CHCRC, where I learned a lot from the many experts there. I especially want to thank Andreas Blaszczyk, who was my supervisor during the stay, and who always had an open door for discussions. Also Patrik Kaufmann, Thomas Christen, Elsi-Mari Borrelli, Christoph Winkelmann and Sergey Pancheshnyi who welcomed me in the VHVlab project. I also want to thank Michael Schueller at the University of Applied Sciences in Rapperswil. Also a thank you to the industrial partners in ABB Skien, especially Magne Saxegaard, Pouria Homayonifar and Elham Attar for coordinating the research project nicely.

I also thank everyone else who has been involved and interested with the project. Finally, a thank you to all colleagues and friends and to my family for all the support.

List of publications (with individual contributions)

I Hans Kristian Meyer, Frank Mauseth, Atle Pedersen, Jonas Ekeberg, *Streamer propagation in rod-plane air gaps with a dielectric barrier*, Conference on Electrical Insulation and Dielectric Phenomena (CEIDP), October 2016

Hans Kristian Meyer performed and planned the experiments with Jonas Ekeberg and Frank Mauseth. Atle Pedersen and Hans Kristian Meyer did the simulations. Hans Kristian Meyer wrote the paper, all contributed to discussions of the results.

II Hans Kristian Meyer, Frank Mauseth, Martine Husøy, Atle Pedersen, Jonas Ekeberg, *Breakdown in short rod-plane gaps under lightning impulse stress*, Nordic Insulation Symposium (Nord-IS), June 2017

Hans Kristian Meyer performed and planned the experiments with Martine Husøy and Jonas Ekeberg. Hans Kristian Meyer wrote the paper. All contributed to discussions of the results.

III Hans Kristian Meyer, Frank Mauseth, Atle Pedersen, Martine Husøy, *Surface charging of dielectric barriers under positive lightning impulse stress*, Conference on Electrical Insulation and Dielectric Phenomena (CEIDP), October 2017

Hans Kristian Meyer performed and planned the experiments with Martine Husøy. Hans Kristian Meyer wrote the paper. All contributed to discussions of the results.

IV Hans Kristian Meyer, Frank Mauseth, Atle Pedersen, Jonas Ekeberg, *Breakdown mechanisms of rod-plane air gaps with a dielectric barrier subject to lightning impulse stress*, IEEE Transactions on Dielectrics and Electrical Insulation, June 2018

Hans Kristian Meyer performed and planned the experiments with Jonas Ekeberg. Hans Kristian Meyer wrote the paper. All contributed to discussions of the results.

V Hans Kristian Meyer, Andreas Blaszczyk, Michael Schueller, Frank Mauseth, Atle Pedersen, *Surface charging of dielectric barriers in short rod-plane air gaps – experiments and simulations*, International Conference on High Voltage Engineering and Application (ICHVE), September 2018

Hans Kristian Meyer performed and planned the experiments with Michael Schueller and Andreas Blaszczyk. Andreas Blaszczyk implemented the software. Andreas Blaszczyk and Hans Kristian Meyer performed the simulations. Hans Kristian Meyer wrote the paper. All contributed to discussions of the results.

VI Andreas Blaszczyk, Thomas Christen, Hans Kristian Meyer, Michael Schueller *Surface Charging Formulations for Engineering Applications. Validation by Experiments and Transient Models*, The 12th International Conference on Scientific Computing in Electrical Engineering, October 2018

Hans Kristian Meyer performed and planned the experiments with Michael Schueller and Andreas Blaszczyk. Andreas Blaszczyk and Thomas Christen performed the simulations and wrote the paper.

VII Hans Kristian Meyer, Robert Marskar, Andreas Blaszczyk, Frank Mauseth, Atle Pedersen *Streamer and surface charge dynamics in non-uniform air gaps with a dielectric barrier*, IEEE Transactions on Dielectrics and Electrical Insulation, August 2019

Hans Kristian Meyer performed the simulations. The simulation code was written by Robert Marskar. Hans Kristian Meyer wrote the paper. All contributed to discussion of the results.

Contents

Chapter 1

Introduction

1.1 Medium voltage switchgear insulation

Medium voltage (MV) switchgear, or distribution switchgear, are devices that are used for connection and disconnection in the distribution grid. MV is typically defined as 1 to 36 kV. Switches, earthing switches, disconnectors, fuses and circuit breakers are typical components. Primary MV switchgear are those connected to the transmission lines, whereas secondary are connected to the low-voltage consumer grids.

The market for especially secondary medium voltage switchgear is large and competitive, and the producers are facing strict demands of cost and space efficiency, reliability and eco-friendliness. Secondary switchgear are mostly constructed as indoor metal-enclosures, typically with some insulating gas. Air is sometimes used at the lower voltage levels (e.g. 12 kV, see fig. 1.1), but SF_6 is the main insulating gas at higher voltage levels. Environmental concerns due its high global warming potential (GWP) have, however, motivated research efforts into alternative insulation systems. The European Union is expected to restrict the use of SF_6 in medium voltage secondary switchgear in near future [1].

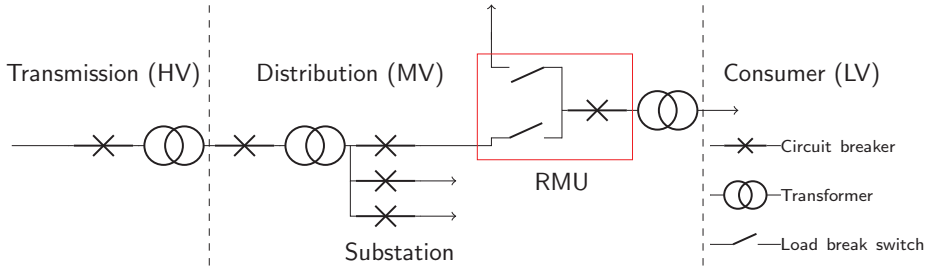

(a)

(b)

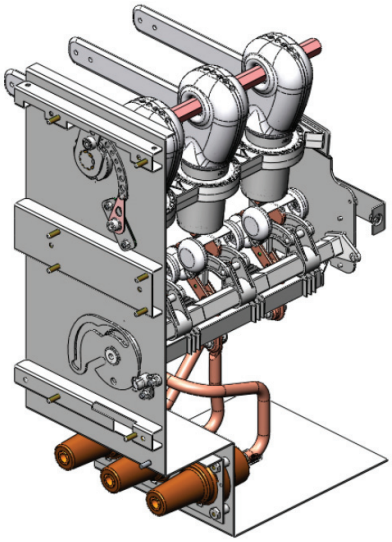

(c)

Figure 1.1: MV metal-enclosed switchgear ring main unit (RMU) a) Simplified distribution network showing location of RMUs in the network, see e.g. [2]. b) It is a challenge to design SF_6-free switchgear cabinets with similar compact sizes as the existing SF_6 solutions c) dielectric design of SF_6-free insulation systems is complicated by inhomogeneous geometries with dielectrics, triple points and short clearances between HV and ground. *SafeRing Air 12 kV, ABB AS electrification products division, 2016 product catalogue* [3].

1.1.1 Alternatives to SF_6

SF_6 is a very strong greenhouse gas. Emissions of SF_6 to the atmosphere comes mostly from the electric power industry, a few million kg per year [4]. 1 kg of SF_6 corresponds to around 22 500 kg of CO_2 in terms of greenhouse effects, which is roughly equivalent to the yearly CO_2-emissions of ten petrol cars. SF_6 is widely in use as electrical insulation in metal-enclosed MV switchgear today. Not only is it a strong dielectric and inert, non-toxic (except for some decomposition products) gas, it also has a high thermal conductivity and a low boiling point.

Research efforts have been invested in alternative insulation systems in the past decade, leading to the proposal of some alternative insulation gases with lower GWP, see e.g. [4]–[6] for a review of these. Although SF_6-free solutions are available, some even with atmospheric air as insulation, the MV market is dominated by SF_6-insulated switchgear. SF_6-insulated switchgears are dominant as they have been a mass product for decades. As the market will likely be incentivized to abandon SF_6-solutions, there is a need for renewed research efforts into alternative MV switchgear insulation systems.

1.1.2 Hybrid air-solid insulation (dielectric barriers)

Air at, or close to, atmospheric pressure has obvious advantages as electrical insulation and is used as insulating medium mainly at lower voltage levels in metal-enclosed MV switchgear. Generally, air-insulated devices require approximately three times more space than SF_6-insulated ones for similar designs. Replacing SF_6 with air is therefore challenging if the equipment size is not increased. Pressurizing the air increases the insulation strength, but high pressures are not economically or practically feasible in most MV switchgear products. The breakdown voltage of an air gap can, however, be significantly increased by either covering live parts with a dielectric material or introducing dielectric barriers between electrodes. Such dielectric design techniques do, however, rely on a detailed knowledge of the relevant discharge behaviour.

1.1.3 Scope of work

The aim of this work is therefore to understand the physical mechanisms relevant to electrical discharges in air gaps with dielectric barriers. Lightning impulse (LI) stressed short ($<$ 120 mm) rod-plane air gaps are used here as the LI tests are the most critical voltage tests for MV switchgear. Simple rod-plane gaps with and without a dielectric barrier are studied with experiments and simulation models. Although the tested geometries are far from real-life switchgear design (see for example fig. 1.1c), they can reveal a great deal about breakdown (BD) phenomena in non-uniform fields, and how these are affected by a dielectric barrier.

Although the rod-barrier-plane geometries are varied in this thesis, the aim is not to experimentally determine the optimal positioning, shape and material properties of the barrier from an engineering point of view. The aim is to characterize the relevant breakdown mechanisms and surface charge effects. Such characterization is needed to improve the breakdown prediction models that are used to design hybrid insulation systems.

1.2 Research questions

In this thesis, the following research questions are investigated:

- What are the characteristics of breakdown in LI-stressed short non-uniform air gaps with and without dielectric barriers?
- How can surface charge distributions on dielectrics after discharges in short LI-stressed rod-plane air gaps be predicted?
- What are the dynamics of surface charging by streamers in short LI-stressed non-uniform air gaps?

1.3 Structure

First, the theoretical background and relevant previous work is presented. Thereafter, experimental methods are presented. Throughout, short lightning impulse stressed rod-plane gaps with a dielectric barrier were used. The experimental activities fall into two main categories:

1. Diagnostics of pre-breakdown and breakdown phenomena
2. Surface potential measurements

The simulation work is then presented. The simulation activities also fall into two main categories:

1. Saturation charge (electrostatic) simulations
2. Drift-diffusion simulations of streamer-dielectric interaction

The published papers form the main body and results of the PhD work. The papers are included after the results, discussion and conclusion.

Chapter 2

Theory

The aim of this chapter is to review the relevant theory in literature for discharges and breakdown in non-uniform air gaps with dielectric barriers. There is a range of different discharge phenomena at play, many of which are not completely understood. Tailoring the insulation system to an acceptable withstand voltage requires an understanding of these breakdown mechanisms.

2.1 Breakdown voltage as a statistical parameter

Dielectric design is often a matter of avoiding breakdown of the insulation systems. Breakdown voltage in air is, however, a statistical parameter, as the availability of starting electrons is fluctuating. A "withstand" voltage level U_{W} is therefore typically defined as 2 % or less probability of breakdown [7]. Experimentally, it is more convenient to use the 50 % breakdown voltage, as it can be estimated from a smaller data set, e.g. with the up-and-down method [8]. U_{W} is, however, the parameter of interest in engineering design.

2.1.1 MV switchgear LI tests

LI tests represent the highest dielectric stresses in MV switchgear type tests. Dielectric barriers can conceivably inhibit discharges during LI events. LI stresses in tests and equipment life are short and few, so partial discharge (PD) erosion problems that can be critical during AC can be disregarded when dimensioning for LI.

IEC standards describe a procedure where 15 positive and 15 negative impulse shots are applied [9]. Two disruptive discharges are allowed at each polarity. The polarity reversal during such tests can be challenging, as accumulated charge on dielectric surfaces can increase local stresses. However, three conditioning impulses at 80 % of the peak value are allowed after a polarity reversal. These are intented to mitigate adverse surface charge effects.

To pass such tests, while keeping the dielectric design efficient, cheap and eco-friendly, a solid understanding of the relevant breakdown mechanisms is needed.

2.2 Townsend avalanche

Discharges in air start with an electron avalanche. At short distances or low pressure (up to ca. 5 bar·mm) the Townsend electron avalanche [10] dominates the BD process. As an electron is accelerated in a gas, it may gain enough energy to ionize neutral gas molecules (impact ionization). An effective ionization coefficient α is defined as the ratio between new electrons and distance in the field direction. It is called effective, as it also includes attachment of electrons (normally described with an attachment coefficient η). $\alpha = \alpha(E)$ is dependent on the electric field strength and can be estimated with empirical fit functions [11], see fig. 2.1.

If N_0 electrons start an avalanche, through ionization N electrons arrive at a distance x from the starting point. These create

$$\mathrm{d}N = N\alpha \mathrm{d}x \tag{2.1}$$

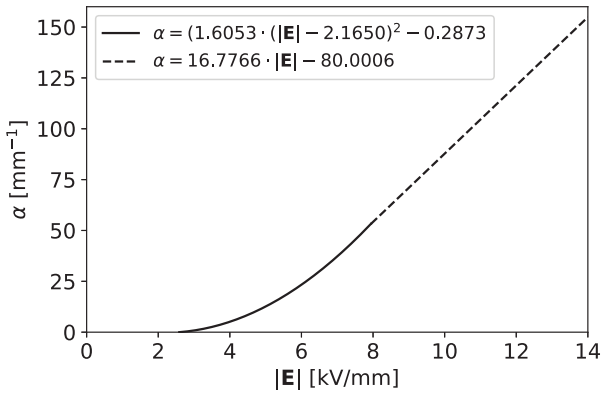

Figure 2.1: Effective ionization coefficient $\alpha(|\mathbf{E}|)$ curve fit. $\alpha(|\mathbf{E}|) = 0$ when the field strength is below the ionization threshold: $|\mathbf{E}| \leq 2.6$ kV/mm [11].

new electrons when propagating a distance dx further opposite to the field direction. By integration,

$$N = N_0 \exp\left(\int_0^d \alpha \mathrm{d}x\right) \tag{2.2}$$

electrons are created in the avalanche over a distance d. In streamers (section 2.3), avalanches start with a free electron in air, so $N_0 = 1$.

2.3 Streamers

The theory of streamers dates back to Raether, Meek, Loeb and Dawson [12]–[15]. If an electron avalanche grows to a critical size ($N_{\mathrm{crit}} \approx 10^6 - 10^8$ electrons), its internal field can sustain discharge processes in comparably low background fields:

$$\exp\left(\int_0^d \alpha \mathrm{d}x\right) \geq N_{\mathrm{crit}} \tag{2.3}$$

Then the field around the space charge head is high enough (ca. 2.5 to 2.6 kV/mm for 1 bar air [7], [16]) to support further electron avalanche

processes in the vicinity. These so-called streamer discharges can either be cathode-directed (positive) or anode-directed (negative), see fig. 2.2.

2.3.1 Streamer structure

The streamer consists of an ionizing front, and a quasi-neutral, weakly ionized channel [17]. The ionizing front is a ca. $1/\alpha$ thick layer, with high local field strengths. This is where the electron avalanches discussed in section 2.2 take place. A charge separation occurs here – the fast electrons leave the slower positive ions behind, which results in a charged region at the streamer front. An example can be seen in fig. 2.3 (simulation of positive streamers) – a net positive charge surrounds the channel (fig. 2.3a), and ionization takes place at the front of each channel branch (fig. 2.3b). The electric field is screened in the channel connecting the streamer head to the anode. The net charge surrounding the channel produces an ambipolar electric field that contains the plasma [16], [18].

2.3.2 Positive streamers

For positive streamers, the electron avalanches propagate towards the positively charged streamer head (see fig. 2.2a), leaving behind new positive charge a little closer to the cathode (the positive ions are one to two orders of magnitude slower than the electrons [19]). As the process continues, the space charge wave continues until it meets the cathode or until the background field is not able to sustain the ionization processes.

2.3.3 Negative streamers

Electron avalanches from negative streamers start from the negative space charge head and propagate outwards from the streamer head, into a lower field region (see fig. 2.2b). Negative streamers therefore require higher background fields in air ($E_{\mathrm{st},-} \approx 1\,\mathrm{kV/mm}$) than positive ($E_{\mathrm{st},+} \approx 0.5\,\mathrm{kV/mm}$) ones to propagate [7], [20], [21].

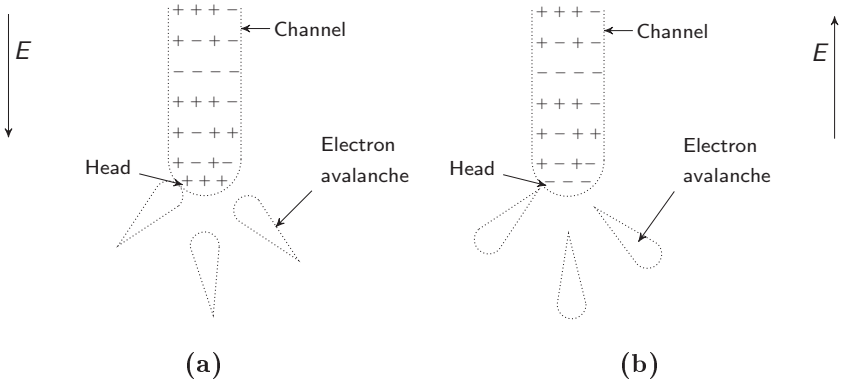

Figure 2.2: Streamer propagation a) positive (electron avalanches moving towards streamer head) b) negative (electron avalanches moving from streamer head into the low field region). Direction of background field E indicated.

2.3.4 Streamer similarity laws

Streamers are multi-scale phenomena: at atmospheric pressure, they have space charge layers of a few tens of µm and are able to propagate in the meter ranges. Furthermore, the time-scale of the physical processes are in the ps range, whereas the velocity is in the mm/ns scale. Streamers follow a similarity law: they exhibit physical similarities at different gas pressures when scaled appropriately for gas density [22]. For example, so-called sprites in the upper mesosphere or low ionosphere are a form of streamer discharge, with diameters in the meter range and propagation lengths of hundreds of m. The similarity law does not, however, hold near material boundaries. The influence of dielectric boundaries in air gaps will be discussed in section 2.7.

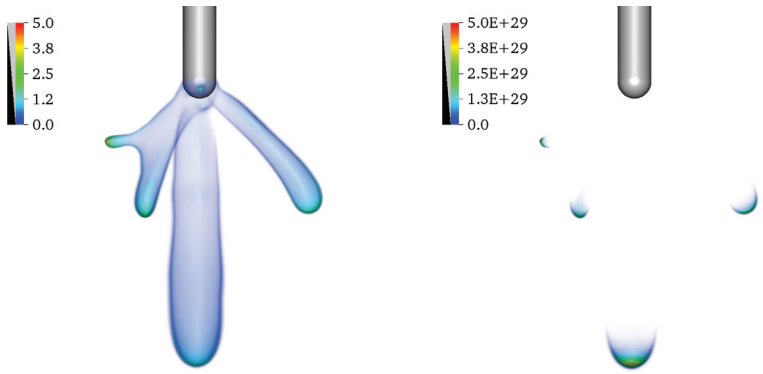

Figure 2.3: Computer simulation of 3D positive streamers [23] (run on 4096 cores on a super-computer). a) Charge density in C/m^3 b) Electron source term in $1/(m^3 s)$. 15 ns simulation time, $2\,cm^3$ domain, with a hemispheric 0.5 mm radius rod electrode protruding 1 cm from the top domain face. Top face and rod 15 kV, bottom face grounded, homogeneous Neumann boundary conditions on sides. The branching is modeled by applying a stochastic pre-ionization level of up to $10^{14}/m^3$.

2.3.5 Other streamer discharge terminology

Corona discharge

The term corona is generally used to describe non-disruptive gas discharges near a HV electrode. In non-uniform fields in atmospheric air, conditions for corona are met if the electric field surrounding the conductor exceeds 2.6 kV/mm. Corona discharges are the cause of the crackling noise that can sometimes be heard near HV overhead lines. In the context of LI breakdown, the initial streamers form a tree-like structure, which is typically called first corona or streamer corona [16]. Other terminology includes glow corona (continuous light) and burst corona (light pulses at intervals of some tens of µs) [24]–[26]. Glow and burst corona were not studied in this thesis, and will therefore not be discussed further here.

Stems

Streamers often emanate from short, bright channels at the electrode known as stems (see e.g. [27]). The stems can become starting points for thermal discharges [28] (the relevant thermal discharges are discussed in sections 2.4 and 2.5).

Trichel pulses

Trichel pulses are a type of negative, repetitive streamer-like discharge. As the discharge develops, a negative space charge forms which shields the cathode, effectively stopping the discharge. After the space charge drifts away, a new discharge starts, and so on. The pulse frequency increases with voltage, typically around 10 kHz to a few MHz.

2.4 Sparks (secondary streamers)

The remaining plasma filaments after a primary streamer can be reilluminated by a secondary streamer [29]–[31]. If the secondary streamer crosses the gap, breakdown can occur due to excessive channel heating, which is also sometimes called streamer breakdown or spark breakdown. This type of breakdown is governed by ohmic heating, thermal shocks and induced pressure waves, and not by the streamer mechanism itself [32]. As will be shown later in this thesis, the spark mechanism was only observed in the most uniform and short air gaps. Mostly, a leader-type discharge (see section 2.5), propagating around the injected streamer charge was seen, as in [31]. Therefore, detailed discussions on the spark breakdown mechanism are not included in this thesis.

2.5 Leaders

The streamer channels can be heated ohmically, causing the field to gas density ratio E/n to increase, which in turn accelerates ionization. When a

thermal detachment temperature $T_{\mathrm{det}} \approx 1500\,\mathrm{K}$ is reached, thermal detachment of negative ions enhances the conductivity and a first leader section is formed [33]. The applied potential will be transferred to the leader head, which becomes the starting point for new streamers (see fig. 2.4). This ionization activity in front of the leader head supplies the necessary energy to advance the leader further into the gap. The leader is ca. one to two orders of magnitude slower than streamers, moving a few 10^{-2} mm/ns [34]. The velocity v_{L} of the leader is typically nearly proportional to the current I_{L} flowing through it [33]–[35]:

$$v_{\mathrm{L}} = \frac{1}{q_{\mathrm{L}}} I_{\mathrm{L}} \tag{2.4}$$

where q_{L} =20 µC/m to 50 µC/m represents the average charge necessary for a unit length advancement of the leader channel. Upon contact with the counter-electrode, the voltage breaks down and an arc follows. In a rod-plane gap, the process of breakdown under positive lightning impulse can occur either through secondary streamer breakdown or leader-type breakdown [28], [31]. The process of positive breakdown can be summarized:

1. Primary streamers incept at the rod electrode, leaving space charge that distort the field. It is followed by a dark period with low current and light emission.

2. A secondary streamer initiates. If it crosses the gap, it will lead to channel heating breakdown.

3. If this streamer is arrested, a leader can initiate from a different part of the rod and propagate to ground, causing leader breakdown.

According to [16], the dark period between primary streamers and thermal discharges is a result of the kinetics of gas heating and of field distortion by the injected streamer space charge. The initial ohmic heating of streamers and stems is only partly transferred into kinetic energy of the air molecules, and most of it is stored as vibrational energy. The conductivity of the channel is only increased sufficiently when the vibrational energy is

transferred to thermal energy after a relaxation time. The injected corona space charge also contributes to the dark period as it shields the field around the inception region.

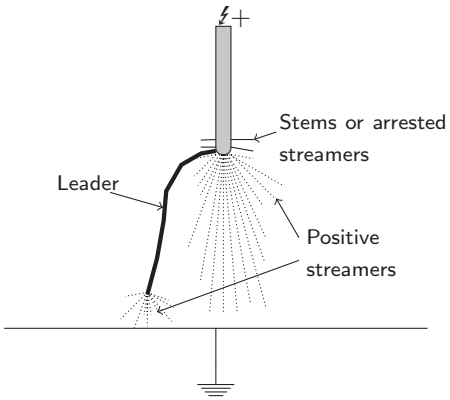

Figure 2.4: Illustration of positive leader breakdown in a rod-plane gap. Leader channels typically propagate around the space charge left by initial primary streamers [16]. The leader channel heats up and expands due to current passing through the channel to feed streamers at its head.

2.5.1 Leader-type channels (short leaders)

Leaders in atmospheric air are normally assumed to exist only in gaps larger than 1 m, and not for 1.2/50 µs LI [7]. Leaders along insulating surfaces are an exception, however, and can be observed from a few cm. This is explained in terms of the higher capacitive current flowing in surface discharges, which facilitates thermal ionization.

Recently, observations of leader-type channels in short rod-plane gaps were reported [31]. It is not clear how to distinguish these from conventional long leaders, as they have similar properties (similar structure, velocity, current and luminosity, see section 5.1.2). In [28], where leader-type channels in short non-uniform air gaps are discussed, any streamer channel which is heated by a streamer corona is regarded as a leader.

2.5.2 Characteristics of breakdown at negative polarity

Less is known about negative than positive lightning impulse breakdown in air. More research exists on positive breakdown, as it typically occurs at lower voltage magnitudes, and is therefore more critical in high voltage applications. Negative breakdown of longer gaps often involves a system of streamers and leaders of both polarities after the dark period [34]. Typically, the negative leader propagation is driven by space stems, bright spots from which streamers of both polarities propagate. A dense network of streamer connects the negative leader and stem. These stems can sometimes become leaders, which then approach the main leader with increasing velocity.

2.6 Breakdown voltage prediction

As computer capabilities are improving, prediction models based on first principles may find applications in dielectric design. One such model is used in this thesis to study streamer and surface charge dynamics in non-uniform air gaps, see sections 2.8 and 4.2.

In conventional dielectric design, however, breakdown voltage prediction typically involves evaluation of semi-empirical or empirical criteria that will be discussed below.

2.6.1 Streamer inception

A useful design criterion when optimizing high voltage devices is to avoid streamer inception. It can be calculated using eq. (2.3) along an electrical field line Γ (see for example [36]–[38]):

$$\int_{\Gamma} \alpha(|\mathbf{E}|)\mathrm{d}x = \ln N_{\mathrm{crit}}. \tag{2.5}$$

Alternatively, eq. (2.5) can also be calculated as a first order partial differential equation to find the inception regions, see [39], [40]. Empirical expressions for $\alpha(|\mathbf{E}|)$ are typically used [11] (see fig. 2.1).

2.6.2 Streamer propagation

Once incepted, a streamer discharge is able to propagate without a strong background field. The propagation distance d_s in strongly inhomogeneous fields with electrode clearance of ca. $5\,\mathrm{cm} < d < 1-2\,\mathrm{m}$ is estimated using an assumption of constant field strength $\mathrm{E_{st}} \approx 0.4\,\mathrm{kV/mm}$ to $0.7\,\mathrm{kV/mm}$ in the channel [7], [19], [21], [41], [42]. For negative streamer propagation, up to $E_{\mathrm{st}} = 1.2\,\mathrm{kV/mm}$ is used [43]. Using the equal area rule

$$E_{\mathrm{st}} \cdot d_s = \int_0^{d_s} E(x)\mathrm{d}x \tag{2.6}$$

the propagation distance d_s is estimated. To estimate the withstand voltage U_W of a gap of length d,

$$U_W = U_0 + E_{\mathrm{st}} \cdot d \tag{2.7}$$

is used [44]. The offset $U_0 \approx$ 20–30 kV is an empirical value needed when fitting breakdown data to a linear curve with slope E_{st}. A typical physical interpretation of U_0 is that it is the excess streamer head potential needed to cause breakdown [44]. Equation (2.7) is sometimes called the streamer stability field criterion.

2.6.3 Leader inception

Models to estimate leader inception and propagation voltages in inhomogeneous gaps have been suggested, see e.g. [16], [27], [28], [45], [46]. The model described in [28] (which is adapted from the SF_6 model in [27]) appears strongest from a physical point of view as it does not include any fit parameters. In the model, streamer and leader channel gas heating dynamics along a single streamer channel and the resulting field distributions are calculated iteratively. Conditions for leader inception and propagation are met as long as the heated channel enables further propagation.

2.6.4 Leader propagation

If the gap is long enough, leader inception may not be sufficient to cause breakdown. In these gaps, leader propagation is the limiting factor. Often, an assumption of a leader stability field of ca. $E_L \approx 0.1\,\mathrm{kV/mm}$ is used to estimate required clearances for atmospheric air gaps larger than around 1 meter [7], [35]. It was shown very recently in [28] that leader propagation models for air provide reasonable breakdown voltage prediction in short ($<$ 1 m), non-uniform air gaps. In the model, the channel field is not constant as one would expect from the streamer stability criterion eq. (2.7). The model shows no explicit dependence on the streamer stability field E_{st}, so it was stated in [28] that the typical breakdown voltage slope of ca. 0.4 to 0.5 kV/mm is likely a result of complex heating mechanisms during leader propagation.

2.6.5 Discharge regimes in short LI-stressed air gaps

The prediction of breakdown voltage relies on an understanding of the different discharge regimes discussed here, and the transitions between them. In fig. 2.5, the breakdown (red), discharge (red and yellow) and no-discharge (green) regimes are illustrated for a rod-plane gap of up to 200 mm with rod hemispheric radius 3.5 mm.

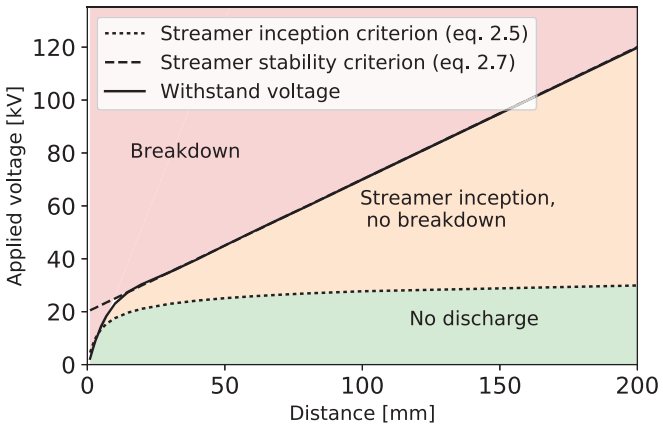

Figure 2.5: Discharge regimes of a short rod-plane gap with a 3.5 mm rod radius. The withstand voltage is estimated with the streamer inception and streamer stability criterion (eq. (2.5) and eq. (2.7)), assuming $U_0 = 20\,\mathrm{kV}$ and $E_{\mathrm{st}} = 0.5\,\mathrm{kV/mm}$. A Python script described in section 4.1.1 was used to calculate inception voltage. Breakdown can occur by either secondary streamer crossing and heating or leader-type channel initation [31].

Streamer inception can be too conservative

In fig. 2.5, it can be seen that the inception integral eq. (2.5) may lead to very conservative estimates of withstand voltage, as it is possible to have streamer inception but no breakdown (yellow region). A dielectric design strategy only based on avoiding streamer inception (eq. (2.5)) will therefore result in unnecessarily large (or over-pressurized) devices.

Transition between leader-type channel inception BD and secondary streamer BD

As will be discussed later (section 5.1.2), leader-type channels dominate 50% BD in these rod-plane gaps from clearances of ca. 40 mm and upwards.

A similar transition region was reported in [31], where streamer and

leader-type BD were observed occurring at the same time in a 30 mm rod-plane gap. It was also shown in [31] that higher LI voltage levels will favour streamer BD over leader-type BD. Furthermore, streamer BD is dominant in shorter or more uniform gaps, while leader-type discharges are more promoted under non-uniform conditions.

A comprehensive BD prediction approach would include a model for predicting the transition to leader-type BD (as in [28]), but such modeling is not in the scope of this thesis.

Transition between leader-type channel inception BD and leader propagation BD

Arrested leader-type channels were only observed in this work when dielectric barriers impeded the channels significantly (see section 5.1.6). It is therefore assumed that leader-type channel initiation automatically leads to BD in short rod-plane gaps. In larger gaps (above ca. 1 m), leader or leader-type channel inception may not automatically cause breakdown, in which case breakdown voltage will be limited by leader propagation (which requires ca. 0.1 kV/mm [7]).

2.7 Dielectric barriers in air gaps

A dielectric barrier can increase the shortest discharge path to ground x_s (see figs. 2.6a and 2.6b) if it is assumed that the streamer will not puncture the barrier. Such barriers can significantly increase the withstand voltage of rod-plane gaps [47]–[50]. Jørstad [50], [51] tested a range of barrier positions and sizes in rod-plane gaps, and showed that linear regression of the 50 % LI breakdown voltages to x_s was consistent with the streamer stability criterion (eq. (2.7)). However, it was also shown that the size and position of the barrier are of great importance. Placing small barriers close to the HV rod can, for example, reduce the breakdown voltage compared with a barrier-less gap. It has generally been shown that the optimal position of a dielectric barrier in a rod-plane gap is in the upper 15-30 % of the gap (i.e., closer to the rod than the ground plane) [47].

In addition to increasing the shortest discharge path, dielectric barriers can acquire surface charge (see fig. 2.6c), which will also influence the insulating properties of the system. The surface charge may, for example, affect leader inception voltages [52]. The interaction between discharges and dielectric surfaces and the resulting charge accumulation are therefore important characteristics for air gaps with dielectric barriers. In [53], for example, it was shown that streamer inception and propagation criteria can provide reasonable AC breakdown voltage estimates of barrier-insulated gaps if surface charge is taken into account.

In MV switchgear, it is also conceivable that the surface charge accumulation during transient overvoltages can be used to the advantage of the insulation system. Detailed knowledge on discharge-dielectric interaction is necessary to realize such designs.

Therefore, discharge-dielectric interaction mechanisms and a surface charge prediction method based on electrostatic simulations will be discussed in this section. In the following section, section 2.8, a fluid model for simulation of streamer and surface charge dynamics will be discussed.

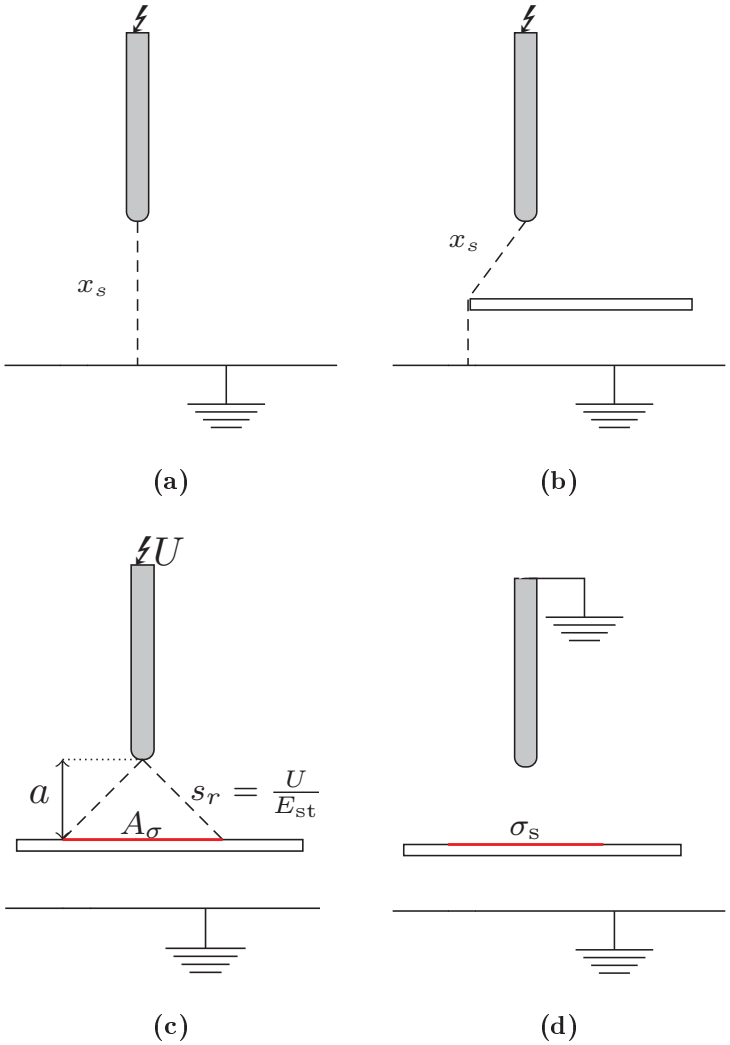

Figure 2.6: a) The shortest inter-electrode distance x_s in a rod-plane gap b) x_s is elongated by an insulating barrier c) the area A_σ of the barrier getting charged by a streamer is a function of the streamer range $s_r = U/E_{st}$ (eq. (2.11)). A_σ is circular with radius $\sqrt{s_r^2 - a^2}$. d) Grounding the electrode with a residual surface charge density σ_s on the barrier can result in back discharges.

2.7.1 Discharge-dielectric interaction

In fig. 2.7, different mechanisms that can affect streamers near dielectrics are illustrated. Bulk and surface conduction (1) may transport charges away from high-field regions if the conductivity is significant. Electron emission from the surface (2) can increase the streamer attraction to the surface [54], and contribute to surface charging. The relevant emission mechanisms are photo-emission, ion bombardment and Schottky emission. Surface charge (3) can alter the electric field distribution significantly (as can space charge). Dielectrics with greater ϵ_r than the surrounding gas also exert attractive forces on charges in the gas due to polarization (4).

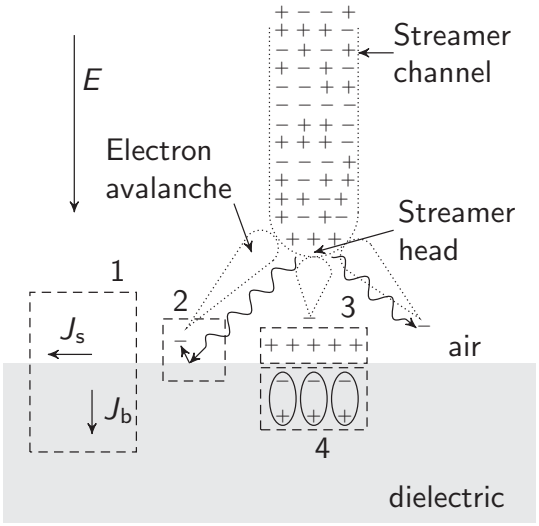

Figure 2.7: Near dielectric surfaces, several mechanisms affect positive streamer development. 1: Surface and bulk conduction (J_s, J_b), 2: Electron emission from the surface by photo-electric emission, Schottky emission or ion bombardment. 3: Surface charge. 4: Polarization.

Predicting surface charge accumulation is of importance in many high-voltage MV switchgear designs, where dielectric surfaces are present in the

form of barriers or mechanical parts (e.g. shafts and spacers, see fig. 1.1c). The surface charge can alter the background field significantly, which in turn can affect discharge behaviour. The effect can be favorable from the point of view of dielectric strength if the surface charge screens exposed points. However, the charge can also have adverse effects, for example if the surface charge leads to a puncture of the dielectric.

2.7.2 Saturation charge on dielectric surfaces

Accurate predictions of charge generation and accumulation is central to an efficient hybrid air-solid insulation design. Efficient methods for engineering predictions often involve calculating extremal cases. When it comes to surface charging of dielectric barriers, zero normal electric field in air $E_{\mathrm{n,air}}$ at the dielectric boundary is such an extremal case:

$$E_{\mathrm{n,air}} = 0 \tag{2.8}$$

The condition is known as saturation charge [43], as no electric field lines in air lead onto the surface. At interfaces, Gauss' law can be expressed as

$$\epsilon_{\mathrm{ins}} E_{\mathrm{n,ins}} - \epsilon_{\mathrm{air}} E_{\mathrm{n,air}} = \sigma_s \tag{2.9}$$

where σ_s is the surface charge, ϵ_{ins} is the permittivity of the dielectric and $E_{\mathrm{n,ins}}$ is the normal electric field at the dielectric side of the gas-dielectric boundary. The saturation charge hypothesis allows the calculation of the unknown saturation charge density σ_{sat}:

$$\epsilon_{\mathrm{ins}} E_{\mathrm{n,ins}} - \sigma_{\mathrm{sat}} = 0 \tag{2.10}$$

The region of the surface where this condition is applied is estimated by assuming that the propagation is limited by the maximum streamer range

$$s_r = U/E_{\mathrm{st.}} \tag{2.11}$$

where the stability field $E_{\mathrm{st.}} \approx 0.4\,\mathrm{kV/mm}$ to $0.6\,\mathrm{kV/mm}$ is the background field required for stable positive streamer propagation [21], [43] and U is the applied voltage. $E_{\mathrm{st}} = 1$ to $1.5\,\mathrm{kV/mm}$ is used for negative streamers [7].

As eq. (2.10) is just an electrostatic boundary condition, the computation of saturation charge is computationally inexpensive. It can therefore be applied to predict charging in high-voltage components.

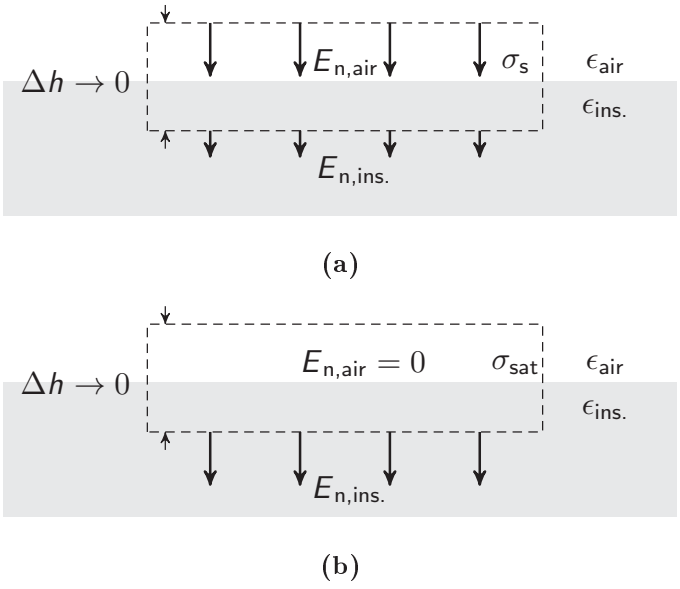

Figure 2.8: Zero normal electric field on the surface boundary in air ($\Delta h \to 0$), also called saturation charge. a) before saturation charging ($\sigma_{\mathrm{s}} < \sigma_{\mathrm{sat}}$) b) after saturation charging ($\sigma_{\mathrm{s}} = \sigma_{\mathrm{sat}}$).

Deviations from saturation charge

As long as there are field lines onto the dielectric and a supply of charges in the air, charge will accumulate on the surface. It is, however, conceivable that a discharge is not able to produce enough charged species to charge the surface to saturation during the voltage pulse. Alternatively, that the produced charges recombine before they can charge the surface to saturation. Moreover, the surface charge itself can quench discharge activity as the dielectric surface becomes charged. Some dielectric surfaces can also

be difficult to reach for the charge particles if the paths to them are mechanically obstructed. The streamers are also branched and not continuous sheaths, so areas in between branches may not be charged to saturation. The branches will be reflected in the surface charge pattern [55], [56].

During a discharge, the space charge in the discharge channels will represent a significant contribution to the electric field distribution. A highly conductive leader discharge (see section 2.5) can, for example, be approximated as an extension of the high voltage electrode. It is also possible to have super-saturation (more than saturation charge) of the surface if there is enough charge in the streamer channel to keep a normal field component onto the surface after saturation is achieved.

Lastly, the surface charge distribution can be rearranged if the surface charge density is high enough to initiate new discharges when the active electrode potential is reduced. Such discharges are known as restrikes or reverse or back/backward discharges [56]–[61].

The surface charge will eventually decay by conduction or neutralization.

Saturation charge in DC fields

Calculating the electric field resistively will produce saturation charge on the entire interface, if the dielectric has a much lower conductivity than the gas. This may, for example, be the case when there is a DC leakage current in the gas, and has been observed experimentally [62], [63]. As this type of charging is many orders of magnitude slower than a LI, it is not directly relevant to this thesis.

The surface charging dynamics relevant for LI in non-uniform fields will be investigated in detail with fluid simulations later in this thesis (see next section (section 2.8) and section 5.3).

2.8 Simulations of streamer-dielectric interation

Simulating streamer discharges with fluid models in high-voltage devices can be useful for predicting the insulation properties of the device. However, the high spatial and temporal resolution requirements for such simulation

models have limited their application. Simulation of full 3D atmospheric air domains with arbitrary electrode and dielectric surfaces have only recently been achieved with computer clusters [64]. The underlying mathematical low-temperature plasma models of the simulation models are also in need of validation [65]. Nevertheless, the models can be used to gain insight in the dynamics of streamer-dielectric interaction. A fluid model was, for example, used to study unexpected flashover on linksticks during live-line work on high voltage overhead lines, by using a 2D rotationally symmetric subset of the geometry [66].

Generally, the first-principles streamer models are either particle models or fluid models (or hybrids) [54], [65]. Only a drift-diffusion model, where particles are described with their average density, will be discussed here.

2.8.1 Drift-diffusion models

Drift-diffusion models can be used to model electrical discharges in a fluid approximation, see e.g. [64], [66]–[80]. They solve for the density n_i of each charged species i with the drift-diffusion-reaction continuity equation:

$$\frac{\partial n_i}{\partial t} + \nabla \cdot (\mathbf{v}_i n_i - D_i \nabla n_i) = S_i, \tag{2.12}$$

So eq. (2.12) is a set of equations, the size of which depends on the number of species in the underlying plasma model. $\mathbf{v}_i$ is drift velocity, D_i diffusion coefficients. Ion diffusion is typically neglected as streamer timescales are in the tens of ns. S_i is a source term that models the reactions and recombinations. These reactions are described with a plasma model, e.g. the one described in [81]. A classic model for atmospheric air is the three-species model by Morrow and Lowke [67]. The main restriction is that temperature and pressure are below levels where thermal ionization takes place, as streamers are non-thermal discharges. Often, it is assumed that the density of charged species n_i is negligibly small compared to the neutral gas density, and that the neutral gas is at rest. However, streamers may affect the surrounding gas convection, and can even be used to control the air flow over an airplane wing [82].

The resulting charged species density is used in the calculation of electric potential Φ with Poisson's equation:

$$\nabla \cdot (\epsilon_r \nabla \Phi) = -\frac{\rho}{\epsilon_0} \tag{2.13}$$

which is based on the assumption that the streamer currents are so small, that magnetic fields (and terms in the Maxwell equations associated with time dependencies of the magnetic fields) are negligible [17]. ρ is the free charge density, ϵ_0 vacuum permittivity, ϵ_r relative permittivity.

In air, a significant part of the ionization is produced by photons. They can, for example, be modeled with different approximations to radiative transport equations (RTEs) instead of solving the complete photo-ionization integral, see e.g. [83].

Surface charging can be modeled by e.g. assuming that all incident charge carriers (charge flux F_σ) onto a dielectric surface become surface charge σ:

$$\frac{d\sigma}{dt} = F_\sigma \tag{2.14}$$

This is a simple but efficient way to model surface charging in drift-diffusion models. More elaborate modeling includes surface trapping, bulk conduction etc., see for example [72], [74], [84].

Equations (2.12) to (2.14) and RTEs are coupled through the chosen plasma kinetics model, and appropriate boundary conditions and initial conditions must be defined.

Computational resources

Drift-diffusion simulations of streamers in atmospheric air in realistic geometries are computationally heavy, especially in 3D. Streamers span several spatial and temporal scales, with typical minimum resolutions in the low or sub µm and ps range when streamers propagate on dielectric surfaces [54]. Computer clusters and adaptive computational meshes are typically necessary for non-symmetrical geometries, often requiring thousands of cores for 3D geometries (see fig. 2.3). The drift-diffusion code implementation used in this thesis will be discussed in section 4.2.

Chapter 3

Experimental Methods

In this chapter, the experimental methods used in the PhD work will be presented. Two different lab setups with LI-stressed rod-barrier-plane gaps have been used. Firstly, a discharge diagnostics setup in the high voltage lab at NTNU with optical and electrical diagnostics of discharges. Secondly, a setup for measuring surface potentials in the high voltage lab at the University of Applied Sciences in Rapperswil, Switzerland (HSR).

3.1 Rod-plane gaps with a dielectric barrier

The most widely used experimental arrangements with inhomogeneous field distributions are variations of the rod-rod (or point-to-point) and rod-plane (or point-to-plane) gap. The degree of field non-uniformity in these geometries can easily be varied by altering the rod radius and/or gap clearance. The rod-plane gap also has the advantage of being polarity dependent.

To investigate the influence of a dielectric barrier in non-uniform fields, rod-plane gaps with a quadratic polycarbonate (Lexan) barrier of width 600 mm, thickness 5 mm and relative permittivity $\epsilon_r = 3$ were used in this work (see fig. 3.1). The rod axis was always perpendicular to the ground plane, while the barrier surface was kept parallel to the ground plane. The HV connection was field graded with a toroid of outer diameter of 200 mm. The

following parameters were varied during the experiments (see fig. 3.1):

1. Rod tip position relative to the ground plane (from 10 to 120 mm)
2. Rod tip radius (2, 3.5 and 10 mm)
3. Barrier upper surface position relative to the ground plane (barrier height) (from 5 to 40 mm)
4. Barrier overhang (0 to 300 mm)
5. Rod length (260 or 500 mm) and toroid inner radius (20 or 30 mm)
6. 1.2/50 µs LI voltage level (ca. −160 to 100 kV)
7. Two different aluminium ground planes: a 1000x1000 mm plane at NTNU and a 600x1000 mm plane at HSR

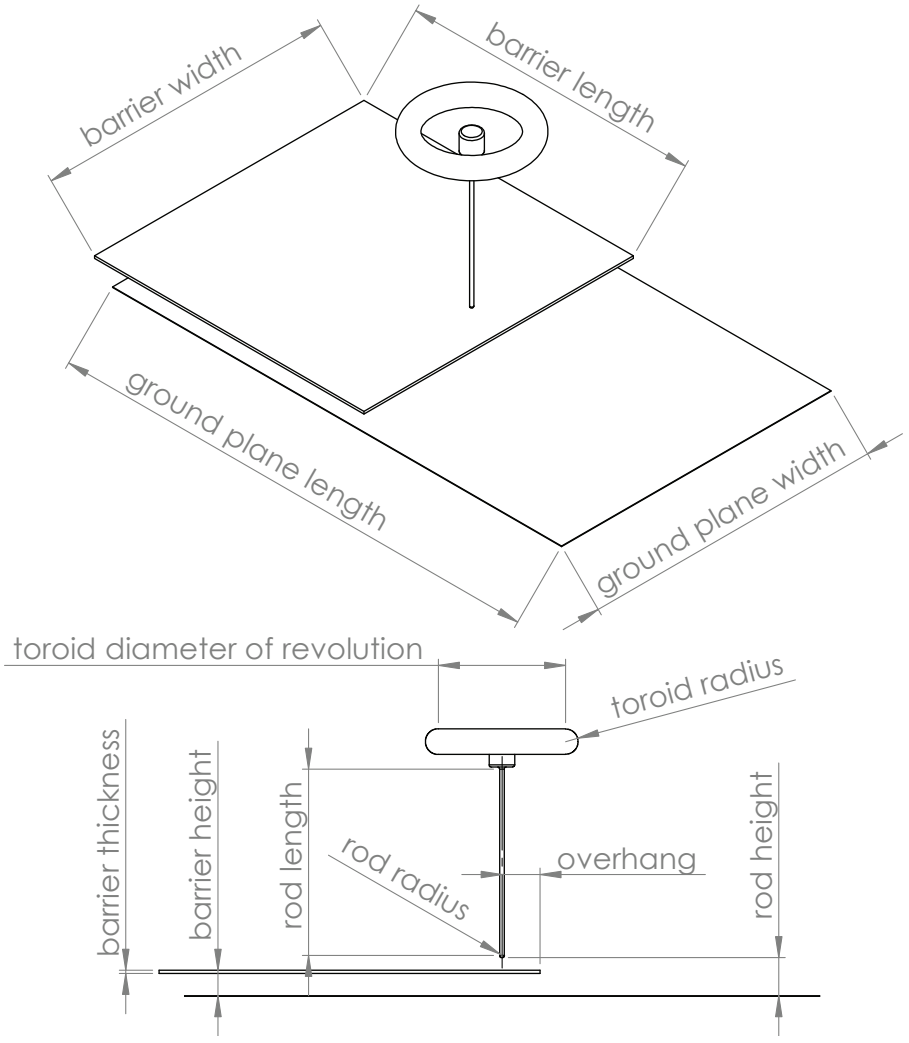

Figure 3.1: Rod-barrier-plane gaps. All geometric parameters can influence the electric field distribution and therefore also the discharge development and surface charge distribution.

3.2 Pre-breakdown and breakdown diagnostics

To understand the nature of discharges in non-uniform gaps with a dielectric barrier, a set-up for optical and electrical diagnostics of discharge activity was built in the high voltage lab at NTNU, see fig. 3.2. The set-up was covered with dark sheets to limit the light pollution. Pressure, humidity and temperature were logged, but they did not vary much in the lab during the experiments. The set-up was adapted from a previous setup built in the NTNU lab to study streamers in transformer oil, see e.g. [85].

Between measurements, the surface was cleaned with a lint-free cloth steeped in isopropyl alcohol (2-propanol) to remove surface charge. After the alcohol was assumed to be evaporated (ca. 15 min.), surface potential probes were used to verify that the surface potential was below a few hundred volts. The alcohol has a low conductivity, comparable with deionized water (a few µS/m [86], [87]), but likely enough to neutralize the charge. The advantage of 2-propanol over water in this case is the rapid evaporation.

A 12 stage 1.2 MV 60 kJ impulse voltage generator was used to generate lightning impulses over the rod as depicted in fig. 3.2. A high speed camera, a PMT and a current measuring system were used to evaluate the discharge activity.

3.2.1 High-speed camera

A high-speed camera and low background light is needed to image the development of streamer discharges, as they are fast and faint. Cameras with intensified charge-coupled devices (ICCDs) are suitable for this purpose. An Imacon 468 with 7 ICCDs equipped with an 85 mm f/1.4 Nikkor lens was used was used in this work. Incoming light is divided into 7 channels in the camera, each leading to an ICCD image sensor. The minimum exposure time of each frame is 10 ns. Each camera frame can be programmed (start time and duration) to capture the desired events. The delay from the impulse trigger signal to the camera trigger pulse was controlled with a Stanford Research Systems DG645 digital delay generator. A typical pattern used in this work is shown in fig. 3.3 – one long frame to capture the

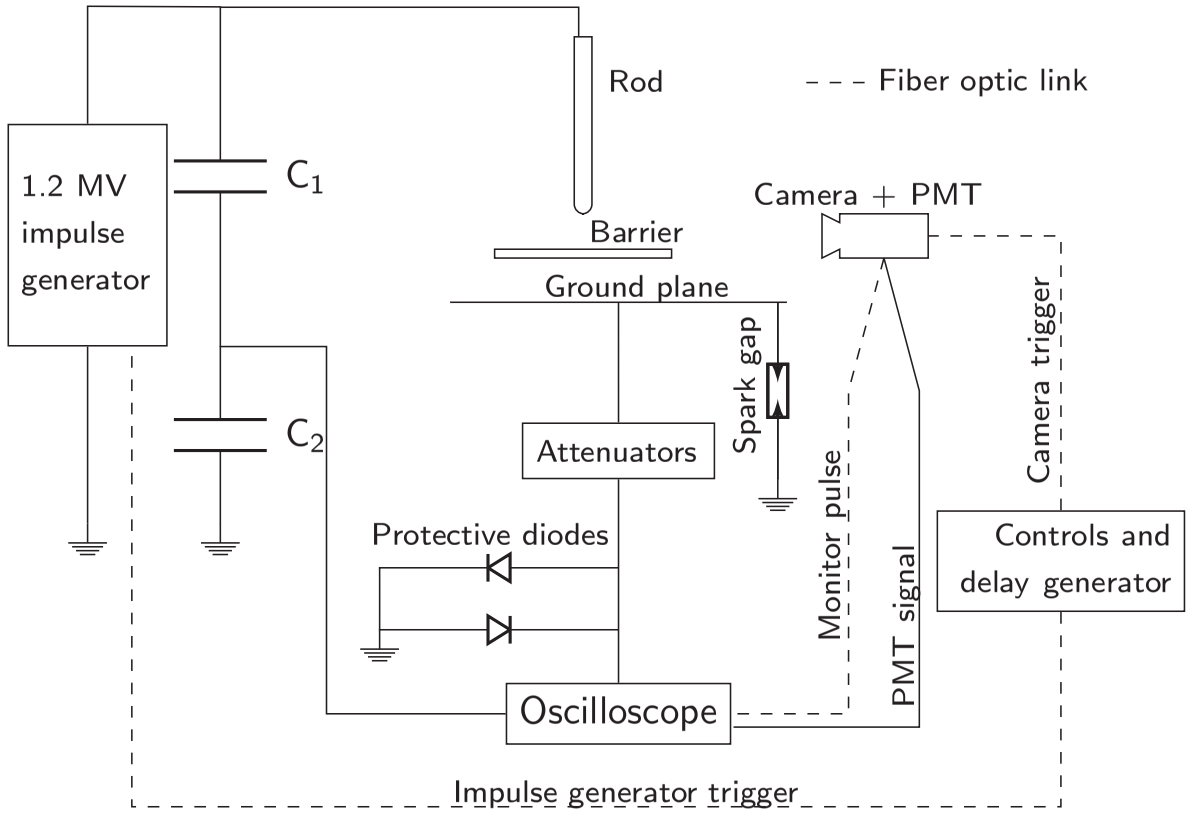

Figure 3.2: Experimental setup, pre-breakdown and breakdown diagnostics of rod-plane gaps with a dielectric barrier. Impulse generator, camera, PMT, current measurement with attenuators (ca. -60 dB) and current measurement protection (spark gap and diodes) are shown. The camera was placed inside a Faraday cage. Black curtains were used to limit light pollution (not shown in figure).

accumulated light, and a series of back-to-back short frames to capture the spatiotemporal discharge development. Some luck and patience was needed to capture good image series, especially since the barrier had to be cleaned in-between LIs. If the barrier was not cleaned, the deposited surface charge would, in most of the tested geometries, inhibit inception. By cleaning the barrier, the discharge would typically occur at roughly the same time on the impulse. This made it easier to pre-progam the frames correctly. For streamer discharges, the frames were typically programmed to capture discharge development at the impulse front.

The streamer discharge event spans some tens of nanoseconds. On this time scale, the propagation times in the cabling and the internal delay in the PMT must be taken into account when assessing the measurements and images. In this work, the delays were compensated in the digital post-processing. The delays in the cables were found using a signal generator and a reference cable. The camera sends a gate pulse to indicate the frame sequence time position (see fig. 3.2). The camera gate pulse was calibrated to the PMT signals using a fast diode and a pulse generator. See fig. B.1 in appendix B for illustrations of this procedure.

Image post-processing

As the discharges are faint, the image brightness and contrast were enhanced with photo-editing software. These parameters were adjusted to the same levels in each image series to normalise the evaluation of discharge intensity. Images of background light were subtracted to normalise intensities of the ICCDs.

3.2.2 Photo-multiplier tube (PMT)

A continuous measurement of light emission can be helpful for detecting and characterizing discharges. This is possible with PMTs. These use a series of dynodes to multiply the photo-electric current produced by incident photons, allowing detection of even single photons. PMTs can also be equipped with filters, which offer the possibility to study the spectra of

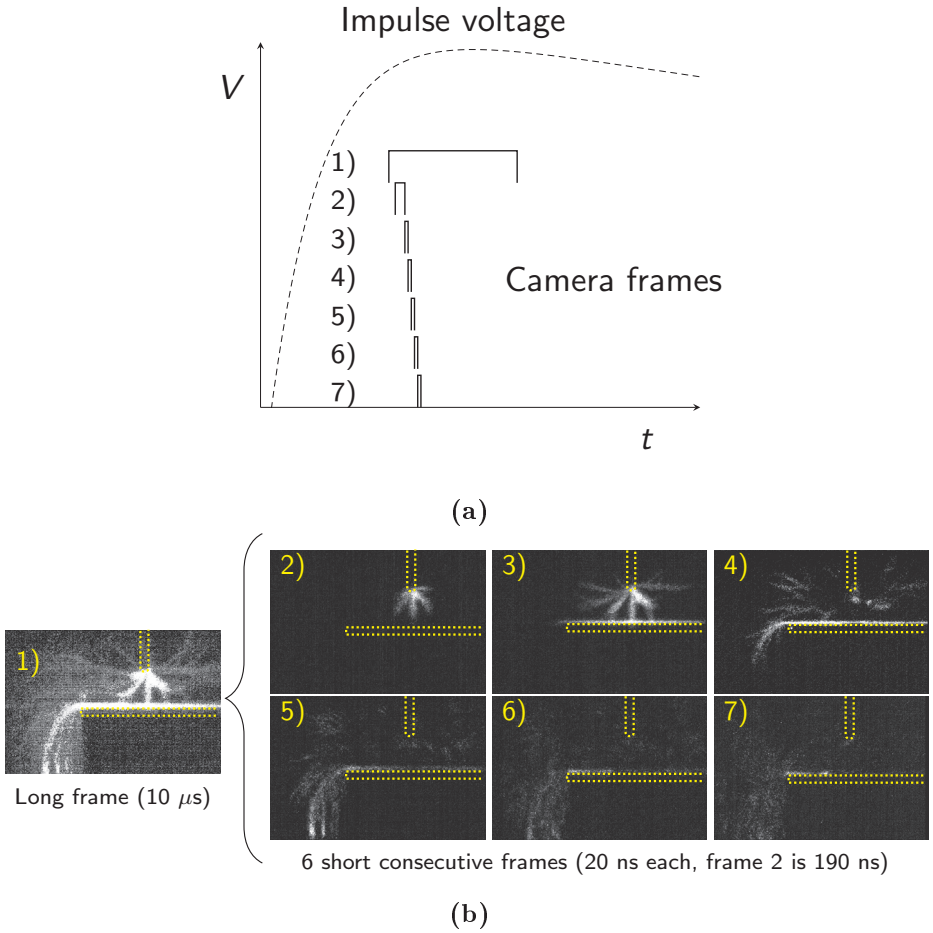

Figure 3.3: Illustration of camera frames programming to LI. Frames numbered from 1 to 7. a) Imacon 468 has seven ICCD frames. One frame, 1), was typically used to get an accumulated picture of the discharges. The remaining frames 2)-7) were used to capture the spatio-temporal development (the frame lengths are not to scale in the figure). b) Example of image series (streamer propagation in 60 mm rod-barrier-plane gap, barrier surface at 40 mm above ground, overhang 40 mm. 75.37 kV LI applied).

discharges. In this work, three different PMTs were used: Philips 56UVP (160-650 nm), Philips 56TVP (360-850 nm) and Philips 56AVP (380-680 nm). Only one PMT was used at a time, and it was placed around 2 m from the test object. The PMT power source was a variable 2.5 kV DC power supply. Two low-pass light filters were also used to study the spectra of the emitted light, with cut-off wavelengths of 610 and 495 nm. When no light filter was used, different paper filters were used to limit the saturation of the PMT.

3.2.3 Fast current measurement

Knowing the amplitude and shape of the discharge current is useful to detect and characterize discharge events. The current flowing through the ground plane has been measured in this work, see fig. 3.2.

The current was measured over the characteristic impedance of a 23 m 50 Ω signal cable (RG-214) with around 400 MHz bandwidth, connected to the ground plane. The RG-214 cable was used as it was observed that the fastest current rise-times were around 8 ns, which corresponds to ca. 30 MHz. With a standard RG-58 BNC cable, the damping is 8 dB per 100 m at 30 MHz, so the current amplitude would be reduced significantly (RG-214 cables have 3.2 dB damping per 100 m at 30 MHz).

A series of T-type 13 GHz attenuators with up to 59.8 dB damping were used in combination with spark gaps in the NTNU lab (430 V) and diodes in anti-parallel (type 1N4149) for oscilloscope overvoltage protection. The diodes act as small signal surge arrestors, arresting the fastest discharge transients before the spark gap triggers. The spark gap therefore triggers when the current exceeds 430 V / 50 Ω = 8.6 A. The spark gap voltage or attenuation can be modified to measure different current ranges, but a practical upper limit is given by the thermal rating of the first attenuator, 5000 V for 400 ns.

At the set-up in HSR, a Pearson 6585 high frequency (200 MHz) current transformer was used. The grounding cable for the ground plane was passed through the current transformer. At HSR, the current measurement was only used to detect discharges, as there was no PMT in that set-up.

Such detection prevented unnecessary surface charge measurements. It was confirmed that surface charge was only produced when a current pulse was observed during the LI.

Different oscilloscopes were used throughout the experiments, with sampling rates from 500 MS/s to 5 GS/s. Some problems were encountered when measuring voltage both at the oscilloscope and the control system of the impulse generator. The last voltage dividing stage before the impulse generator is 100 to 1 MΩ. Adding another oscilloscope in parallel with 1 MΩ impedance effectively lowers the resistance of the lower arm of the voltage divider. The problem was solved by using a 10 MΩ probe when connecting the oscilloscope, and adding a ferrite core to choke noise in the cable shield of the oscilloscope cable.

Development of the current measurement system

Measuring on the ground plane has some disadvantages. The larger charging current can be a problem, and it is more challenging to shield the plane than the rod from electromagnetic noise [88]. Measurement on the HV side is complicated as electrical isolation is needed, e.g. with a fiber optic link. Attempts were made in this work to add a fiber optic measurement link. It was, however, difficult to find a reliable and cheap enough solution with high bandwidths. Instead, the current was measured on the ground plane.

The noise and capacitive currents should not differ for the same geometry, and are normally scalable with applied voltage. Some attempts were made to filter the noisy part of the current measurement digitally. Different filters were tried, but the noise pulse and discharge pulse had sometimes similar frequency components. The best filtering method was to subtract a scaled current measurement where no discharge activity was seen. The original current measurement was also plotted in the results, as the performance of the filtering methods was unclear. Where current measurements were discussed, weight was mostly given to measurements where the current pulses appear after the initial noise, e.g. during leader propagation.

A setup where the HV was applied to the plane was also made, by an MSc student [89]. When the HV is applied to the plane, the rod can be

screened, resulting in less noise in the measured ground current.

3.2.4 Inception and breakdown voltage estimation

50 % inception and breakdown voltages of different rod-plane gaps and rod-barrier-plane gaps were estimated using the up-and-down method [7], [8] with 20 shots (barrier cleaned and discharged between shots) and steps of 0.5 kV. The results were corrected for pressure, temperature and humidity according to [9]. Breakdown was detected by voltage pulse collapse, whereas inception was detected with a PMT.

3.3 Surface charge measurements

Charge density and polarity after a discharge can be visualized using Lichtenberg dust figures. This method can, however, not be used to estimate charge magnitudes.

Non-contacting methods measuring the voltage or electric field above the surface are often employed to measure surface charge indirectly. The calculation of surface charge density distributions from probe readings is an inverse problem that requires accurate measurements with low noise levels. Probe types include capacitive probes, field-nullifying probes or electro-optic probes. The surface charge density distribution can be estimated with different methods of deconvolving the volt- or fieldmeter outputs [90]–[97]. Finite element method (FEM) software like COMSOL Multiphysics will, for example, produce surface charge density distribution estimates when applying the measured potential or field distributions as boundary conditions on the surface. However, if this approach is used, it must be assumed that the influence of the probe on the measurement is negligible.

3.3.1 Surface potential probe

The surface potential or fieldmeter outputs are also directly useful if they are analyzed with appropriate methods. Surface potential measurements with a field-nullifying Trek 3455ET probe driven by a Trek 341B ±20 kV amplifier

were used in this work (see [98]–[102] for other research with similar probe types). Such instruments operate a HV feedback mechanism that drives the housing to the same voltage as the surface seen by the probe sensor. By doing so, the probe itself can be considered as an extension of the potential it is measuring. In a way the probe operation is analogous to the saturation charge concept described in section 2.7.2, as it zeroes the electric field in the air between the surface and the probe housing. The measured potential should not exceed ±20 kV, as this may cause electrostatic discharging to the probe housing. The Trek 3455ET probe influence on the measurement is typically a few % [99], [101], whereas probes with grounded housings will affect the measurement much more (e.g. the Trek probe 3550A, voltmeter 354A, which was shortly tried in this work and used in [97]). However, the probe-to-surface distance should be as small as possible to resolve sharp gradients in surface potential. The probe reading will be an average of the part of the surface seen by the probe [103], which can roughly be approximated as a conical region stretching from the circular probe aperture (ca. 1.5 mm diameter aperture for the 3455ET probe used here).

3.3.2 Robotized scan

Typically, the dielectric surface is scanned with a robot stage to get a two-dimensional image of the charge distribution. Initially in this project, a surface charge measurement set-up was built in the NTNU high voltage lab. Here, the probe was simply moved manually with steps of 10 mm along a single axis, and the surface potential was sampled with an Agilent logger.

Later on, in the high voltage lab in Rapperswil, a measurement set-up (figs. 3.1 and 3.4) with the probe mounted on a Velmex two-axis robot stage was built. After the LI was applied to the rod-barrier-plane gap, the barrier and plane were moved along a rail to the robot (fig. 3.4a), at which point a scan was initiated (fig. 3.4b). The time from LI application to measurement was around 2-3 minutes. The scan and data acquisition were managed with a LabView routine and a NI-cDAQ 9171 data acquisition (DAQ) device. In most cases, the robot was simply scanned along the center axis, as the discharge pattern was highly symmetrical. Some 2D scans were also made

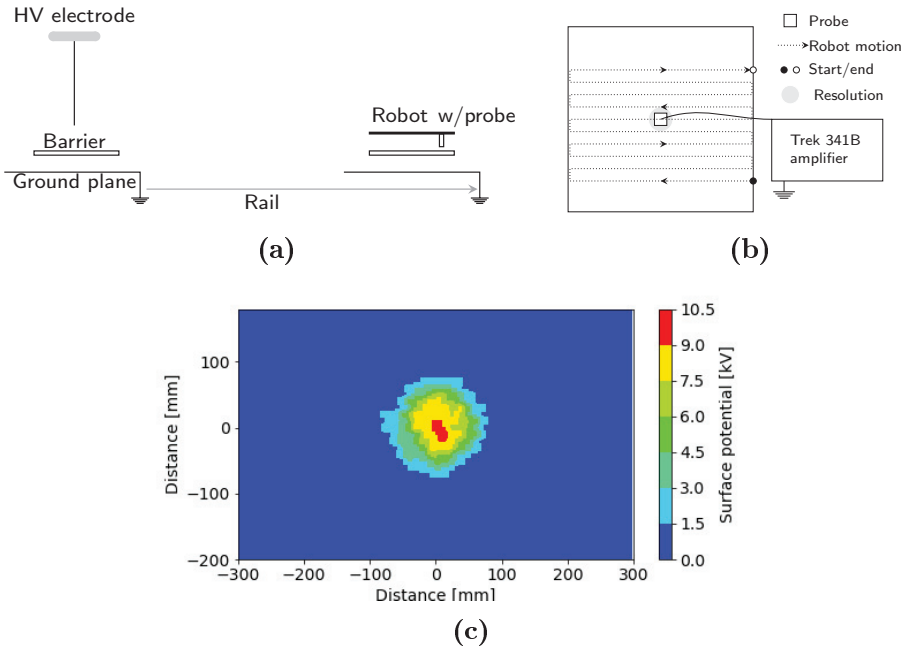

Figure 3.4: Surface potential measurements a) Rail system to measure surface potential in rod-plane gaps with a dielectric barrier after a LI, top view. After LI application, the barrier and plane are moved from the HV electrode to the probe for measurement. b) Illustration of robot scan pattern over the dielectric barrier, front view. The resolution of the probe is given by the probe-to-surface spacing. c) Example 2D surface potential scan (contour plot), 60 mm gap with 3.5 mm rod radius, barrier on ground plane, after applying a 65 kV 1.2/50 µs LI. The measured surface potential can be directly compared with simulations when the procedure described in section 4.1.2 is used, and if it is assumed that the probe influence on the measurement is negligible (the probe influence is typically a few % [99], [101]).

in a pattern similar to that illustrated in fig. 3.4b.

The velocity of the motors was 6000 steps/s, which corresponded to a speed of 30 mm/s. The sample rate of the DAQ was 100 samples/s. As the DAQ and motor did not always start at exactly the same time, the respective starting times of the robot and the DAQ were logged in LabView. When plotting the results, the DAQ samples taken during the dead time of the motor were removed.

Chapter 4

Numerical Methods

In this work, two main simulation models were used. One is an engineering tool called Virtual High Voltage lab (VHVlab) [104], which is designed for breakdown voltage prediction in medium or high voltage equipment. It implements, among other things, saturation charge conditions (eqs. (2.8) and (2.10)) with a boundary element method (BEM) solver. For some geometries, COMSOL Multiphysics (a commercial finite element method (FEM) solver) was used for saturation charge simulations as well.

The other main simulation tool used here is a newly developed drift-diffusion model for streamer discharges called PlasmaC [64]. The code is scalable to thousands of computer cores and enables simulation of discharges in 3D geometries with arbitrary dielectric and electrode shapes. However, only 2D simulations were used in this work to limit the computational effort.

4.1 Electrostatic simulations

4.1.1 Inception and breakdown voltages

The inception voltages were calculated by evaluating the inception integral eq. (2.5) with $\ln N_{\text{crit}} = 9.15$ [11]. The background field must first be calculated, thereafter eq. (2.5) is typically evaluated along electrical field lines. In addition to inception computations with VHVlab [104], a Python

script was implemented to calculate inception from FEM results. The script input is a background field line and the applied voltage and pressure (1 bar in this work). It evaluates the inception integral, by scaling up the field in small steps until the integral is $\geq \ln N_{\text{crit}}$. The final voltage is then the inception voltage.

4.1.2 Saturation charge and extensions

In addition to inception calculations, VHVlab includes the possibility to calculate saturation charge (eqs. (2.8) and (2.10)). Some saturation charge computations were also performed with commercial FEM software. A comparison of COMSOL Multiphysics (FEM) and VHVlab (BEM) inception and saturation charge resulted in equal solutions. An example of a saturation charge computation in VHVlab is illustrated in fig. 4.1.

An attempt was made to predict the influence of restrikes (also called back or reverse discharges [59], [105]) on the surface charge distributions. Restrikes can occur at the impulse tail, when the field between the charged surface and grounded rod can become high enough to support discharge activity (as illustrated in fig. 2.6d). To compute restrikes, charge was removed and the normal field equalized to a non-zero value. This removal of charge and subsequent equalizing continued until there was no longer inception at the rod tip. See fig. 4.2 for illustration of the procedure.

In the experiments, the surface potential distribution was measured on the barrier after it was moved away from the HV electrode (fig. 3.4a). To be able to compare the computations with the measured surface potentials, the potential distribution without the rod had to be computed, as the presence of the rod affects the potential distribution.

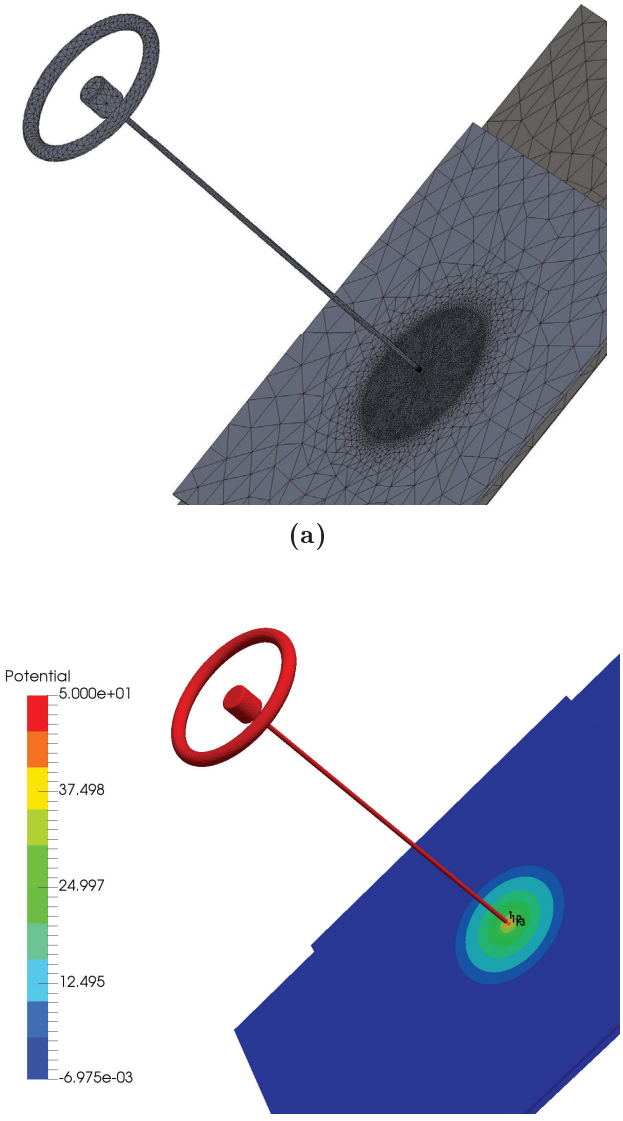

Figure 4.1: Example of VHVlab saturation charge computation. a) Surface mesh rod-barrier-plane gap, generated with CAD software. b) Surface potential, with saturation charge, calculated in VHVlab.

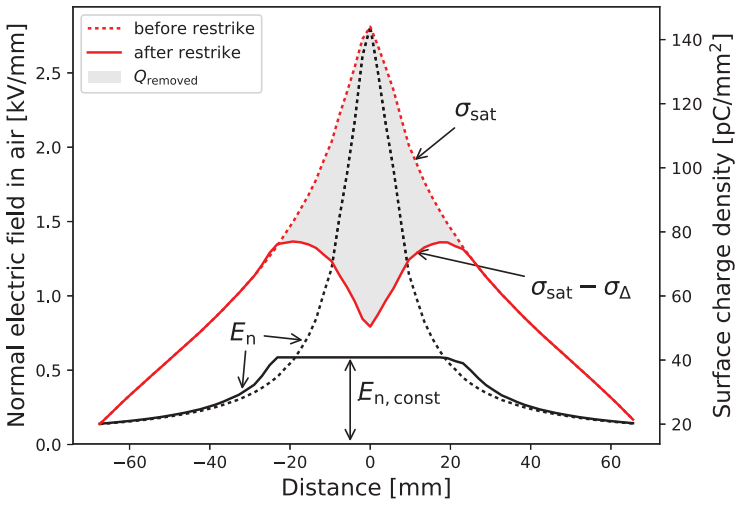

Figure 4.2: A restrike (back discharge) calculation example – removing charge and equalizing the normal electric field. Distributions of charge density and normal field strength before and after the restrike calculated with conditions: applied voltage 35 kV, rod radius 2 mm, gap 10 mm, 5 mm barrier resting on the ground plane. Black lines: normal electric field in air at the surface. Red lines: surface charge density. Solid/dotted lines: before/after restrike.

Computational procedure

The following computational procedure was followed (see also fig. 4.3):

1. Calculate background field with zero surface charge and applied voltage U.

2. Evaluate discharge propagation paths (as field lines) and the streamer inception voltage U_{i} .

3. If a streamer collides with a dielectric surface, assume on an area A_{σ} of this surface the saturation charge boundary condition and compute

the unknown saturation charge σ_{sat} according to eqs. (2.8) and (2.10). The outer border of A_σ is determined from the maximum streamer propagation range (eq. (2.11)) calculated as applied voltage U divided by the stability fields $E_{\mathrm{st,+}} = 0.5\,\mathrm{kV/mm}$ for positive and $E_{\mathrm{st,-}} = 1\,\mathrm{kV/mm}$ for negative polarities (see also fig. 2.6c).

4. Calculate saturation inception voltage $U_{\mathrm{i,sat.}}$. If $U_{\mathrm{i,sat.}} > U$, scale down U until $U_{\mathrm{i,sat.}} = U$. For the reduced voltage the discharge, and therefore also the surface charging, will be suppressed. This step is included, as it is assumed that the accumulated charge may decrease the field strength at the original inception points and extinguish the discharge before saturation is achieved.

5. Evaluate whether there are new critical field lines that will lead to inception and charging of other surfaces.

6. Ground the active electrode and calculate restrike inception voltage $U_{\mathrm{i,res}}$. For $U_{\mathrm{i,res}} \leq U$, the prediction is that there will be restrikes between the dielectric surface and the electrode when it is grounded.

7. If there is a restrike, remove a fraction of the surface charge and calculate the new shape assuming that the normal field is equalized in the region where charge is removed (see fig. 4.2). Change the fraction iteratively until the restrike is suppressed, i.e. $U \leq U_{\mathrm{i,res}}$.

8. Recalculate the field without the active electrode and extract the surface potential for comparisons with experiments.

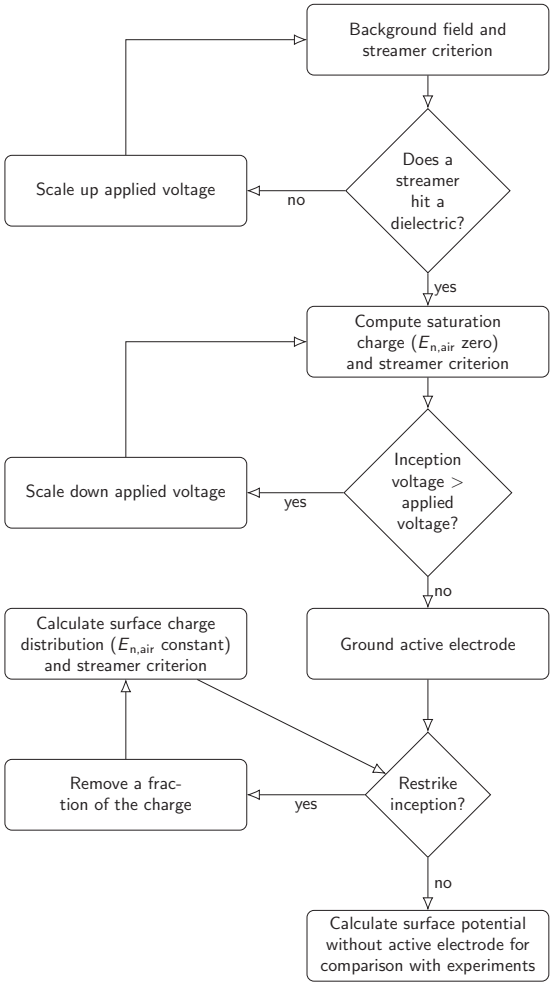

Figure 4.3: Computational procedure, saturation charging.

4.2 Drift diffusion simulations

The drift-diffusion simulations solve the drift-diffusion continuity equation (eq. (2.12)), Poisson's equation (eq. (2.13)) and approximate solutions to a set of radiative transfer equations (RTE) to model photo-ionization. A finite volume method with adaptive mesh refinement is used, see section 4.2.3 and [64] for further details on the implementation.

4.2.1 Equation coupling: streamer kinetics

Poisson's equation (eq. (2.13)), the drift-diffusion continuity equation (eq. (2.12)) and the RTEs (see section 4.2.2) are coupled through source terms S_i, diffusion coefficients D_i and velocities $\mathbf{v}_i$ with the streamer plasma kinetics model described in [67]. It includes three charged species i; electrons ($i = \mathrm{e}$), positive ($i = +$) and negative ions ($i = -$), and has been widely used [73], [75], [77]. The source terms are given by

$$S_\mathrm{e} = S_\mathrm{ph.} + n_\mathrm{e}\alpha|\mathbf{v}_\mathrm{e}| - n_\mathrm{e}\eta|\mathbf{v}_\mathrm{e}| - n_\mathrm{e}n_+\beta \tag{4.1}$$

$$S_+ = S_\mathrm{ph.} + n_\mathrm{e}\alpha|\mathbf{v}_\mathrm{e}| - n_\mathrm{e}n_+\beta - n_-n_+\beta \tag{4.2}$$

$$S_- = n_\mathrm{e}\eta|\mathbf{v}_\mathrm{e}| - n_-n_+\beta \tag{4.3}$$

where α, η and β are ionization, attachment and recombination coefficients respectively, for which calculated expressions are given in [67]. The calculated reaction rate coefficients can be found in [106]. These are obtained from calculated electron energy distributions as a function of the electric field, using the method described in [107]. Empirical expressions are also given for $\mathbf{v}_i$ and D_i (as functions of the electric field) in [67]. $S_\mathrm{ph.}$ is a photo-ionization source term, which will be shortly discussed in section 4.2.2.

A uniform density of positive ions and electrons, $10^{10}/\mathrm{m}^3$, which is a typical level inside buildings [108], is applied as an initial condition. At the electrodes, there is a free outflow of charged species. Surface charging of dielectrics is modeled by assuming that incident charge carriers onto the dielectric become surface charge (see eq. (2.14)), and that incident photons and positive ions may release electrons (details will be given below, see eqs. (4.6) to (4.10)).

4.2.2 Radiative transfer and photoionization

The radiative transfer equation (RTE) describes energy transfer in the form of absorption, emission and scattering of electromagnetic radiation. In streamer discharges, the photons can ionize air molecules or cause emission of electrons from solid materials and therefore contribute to the discharge development. The model for radiative transfer and photoionization in the simulation work here (see [64]) relies on a number of simplifications that will only be briefly mentioned below. It is not in the scope of this thesis to discuss the simplifications and limitations of the radiative transfer and photoionization model. In the discussion of the results (chapter 5), the effect of streamer light emission is discussed in a mainly qualitative way, in the context of the influence of photoemission on surface charging dynamics (see section 5.3).

Computation of the radiative energy transfer in the entire frequency spectrum is computationally heavy. In the model used here, it is assumed that a single frequency band is relevant for photoionization in air. The photoionization source terms S_{ph} are estimated with a three-exponential fit (see details in [83]).

Direct numerical solution of a RTE is complicated, even when restricting the frequency bands. In the drift-diffusion simulation code here, an approximation to the RTE known as the Eddington approximation is used. See [83], [109] for details on this approach.

4.2.3 Implementation

A finite volume code implementation described in [64] was used. It uses cartesian grids with adaptive mesh refinement. The simulations were run in planar 2D domains, and used up to 512 cores on a super-computer (16 out of 1006 nodes, each with 2 Intel E5-2683v4 chips with 16 cores).

Adaptive meshing

Adaptive meshing can limit the amount of computational cells, and therefore reduce the computational burden significantly. The local mesh size is mainly

controlled by the relative electric field strength E_{rel} in this work

$$E_{\text{rel}} = |\mathbf{E}|/\max(|\mathbf{E}|) \tag{4.4}$$

The meshing strategy was based on the assumption that finer mesh is needed in areas with relatively large electric field strength or large electric field strength gradients (∇E_{rel}), which is typically near the streamer head in streamer simulations.

The simulations here were in 16 cm^2 2D (see section 4.2.4), with a base grid of 128×128 (for domain shown in fig. 4.5a) or 256×64 (for domain shown in fig. 4.5b) equal-sized quadratic cells. The coarsest grid cells were therefore $\Delta x_{\max} = 312.5\,\mu\text{m}$ wide. When refining the grid cells, they were split into smaller cells of size $\Delta x_{\max}/f$, where f is a refinement factor. In total, five refinement levels were used, with a mix of $f = 2$ and $f = 4$. The ratio between the coarsest and finest grid size was $\Delta x_{\max}/\Delta x_{\min} = 2 \times 4^4$. So $\Delta x_{\min} = 0.61\,\mu\text{m}$ was used at the finest level. This size was used, as the accuracy of the velocity computation for a streamer propagating along a dielectric surface is sensitive to mesh size. An acceptable accuracy level has been observed for mesh size in the range of 1 µm [71]. Reduction of the mesh size below 1 µm does not significantly improve accuracy. If $\Delta x_{\min} = 0.61\,\mu\text{m}$ would have been uniformly used here, it would correspond to effective domains of 65536×65536 or 131147×32787 (4 billion cells). As adaptive meshing was used, the resulting number of cells varied from a few million to 14 million. The domain was remeshed at every tenth time step.

Time stepping

The time steps Δt were around 0.3 ps to 0.6 ps, mainly limited by the Courant-Friedrichs-Lewy (CFL) condition. The CFL condition limits the time step Δt of the simulation as

$$\Delta t \leq k_{\text{CFL}} \Delta x_{\min}/|\mathbf{v}_i| \tag{4.5}$$

where $|\mathbf{v}_i|$ is the maximum species velocity in the computational cell and $k_{\text{CFL}} \leq 1$ is a constant. Through trial and error, k_{CFL} was set to 0.6 to

ensure numerically stable solutions. The CFL condition (eq. (4.5)) protects the numerical stability of the simulation by restricting the displacement of a charged particle to one grid cell during the time step Δt.

Material boundaries

Material boundaries within the simulation domain are described with level-set functions $s(x, y)$ where $s(x, y) = 0$ describes the boundary interface. The material boundaries are then approximated as straight lines cutting through the cell (cut-cells), see fig. 4.4. Since the partial differential equations are calculated in the cell centers (black dots in fig. 4.4), the fluxes (i.e. mass, electric and photon fluxes) at the material boundaries are estimated with extrapolation. For details on the extrapolation methods (and on the code in general), the reader is referred to [64].

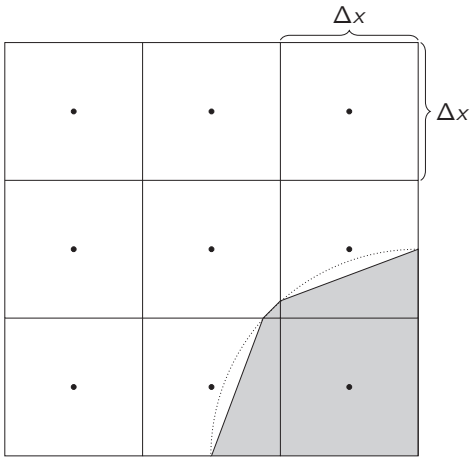

Figure 4.4: The domain is discretized with rectangular grids, with adapative mesh size Δx. Boundaries are described with level-set functions (here illustrated with a dotted line), and approximated as straight lines cutting through each cell. The white-colored area is the gas, grey-shaded area is a solid material (electrode or dielectric). Since the code solves for the cell centers (black dots), the fluxes (i.e. mass, electric and photon fluxes) at the material boundaries are found by extrapolation from the air.

Surface charging

As the streamer propagates near a dielectric surface, there is a net charge flux F_σ

$$F_\sigma = \frac{d\sigma}{dt} = q_\mathrm{e}(F_\mathrm{e} - F_+ + F_-) \tag{4.6}$$

into the surface. F_σ is integrated over time and becomes surface charge σ. The fluxes F_+, F_- and F_e are charged species fluxes onto the surface, q_e is the electron charge. As mentioned above, the fluxes at material boundaries are found by extrapolating from the air side. However, charged species should not be emitted from the surface if the extrapolated flux points out of the dielectric. A max() function is used here to prevent such emission:

$$F_+ = \max(0, \tilde{F_+}) \tag{4.7}$$

$$F_- = \max(0, \tilde{F_-}) \tag{4.8}$$

$$F_\mathrm{e} = \max(0, \tilde{F_\mathrm{e}}) - A(\gamma F_\mathrm{ph} + \kappa F_+) \tag{4.9}$$

$$A = \begin{cases} 1, \text{if } \mathbf{E}\cdot\mathbf{n} \leq 0 \\ 0, \text{otherwise} \end{cases} \tag{4.10}$$

Here $\tilde{F_+}$, $\tilde{F_-}$, $\tilde{F_e}$ are linearly extrapolated fluxes from the air to the surface and $\mathbf{n}$ surface normal pointing into the air. F_ph is the photon flux into the surface.

Two electron emission mechansims are implemented in the electron flux F_e: photoemission (γ electrons released per incident photon) and positive ion bombardment (κ electrons released per incident positive ion). These only contribute when the electric field points into the dielectric, hence the conditional A. Emission mechanisms contribute to surface charging, as every emitted electron leaves behind an electron hole.

For positive ion bombardment, $\kappa = 0.1$ is used here, which is a high estimate (at cathodes, the order of magnitude of κ is, for instance, 0.01 [19]). $\kappa = 0.1$ is sometimes used in streamer simulations to account for emission phenomena that are not included in the model [18], [76]. Ion

bombardment is contributing directly to surface charging, as every emitted electron leaves a positive charge behind. However, with $\kappa = 0.1$, the ion bombardment direct contribution to surface charge is an order of magnitude smaller than that of the ion drift, so it is not expected that the coefficient will affect the surface charging behaviour strongly.

γ (photoelectron emission yield/photoemission efficiency) depends on both the material and gas properties. Experimental data on photoemission from dielectrics is limited, especially in the presence of a discharge. Estimates for γ fall in the large range from 10^{-7} to 1 for polymers (references can be found in [54]). The photoionization model in this work only accounts for UV-photons, as those are considered responsible for photoionization in air [83]. Longer wavelength photons may contribute to photoemission from dielectric surfaces in air, but the effect is small as γ decreases with decreasing photon energy. In this study, γ was set to 10^{-6} and 10^{-1} to study its influence on the surface charge accumulation and positive streamer dynamics.

4.2.4 Computational domains

Blade-barrier-plane gaps were used instead of rod-barrier-plane gaps as the code implementation does not support cylindrical coordinates (only 2D planar or 3D). Two simulation geometries were used, see table 4.1 for parameters and fig. 4.5 for illustrations. Throughout, the dielectric was 5 mm thick with $\epsilon_r = 3$, resting on the ground plane and centered. The barrier edges were rounded with 0.2 mm radius. Geometry G1 was used to study the influence of photoemission. To test whether the streamer range concept (eq. (2.11)) would hold in the fluid simulations, geometry G2 was made. To enable streamer inception at lower voltages and longer streamer propagation distances, G2 has a sharper electrode tip and wider dielectric.

A constant potential U was applied in the simulations instead of a 1.2/50 µs LI pulse. The total duration of the simulations was between 15 and 115 ns. If it is assumed that the first electron avalanche will appear close to the LI peak, the voltage level variation during 115 ns is a few percent, so a constant potential is a reasonable approximation.

Table 4.1: Simulation parameters (see also fig. 4.5)

Parameter	Geometry	
	G1	G2
Domain[mm^2]	40x40	80x20
Blade tip radius [mm]	2	0.5
Dist. blade tip to ground [mm]	10	7
Blade potential U [kV]	35	35 or 14
Barrier width [mm]	22	72
Photoemission efficiency γ	10^{-6} or 10^{-1}	10^{-6}

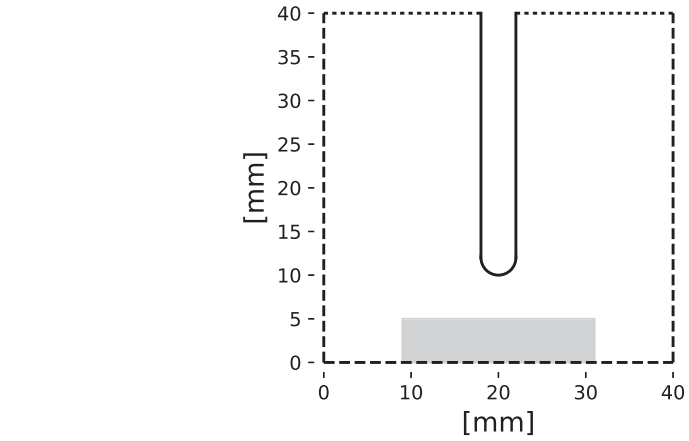

(a)

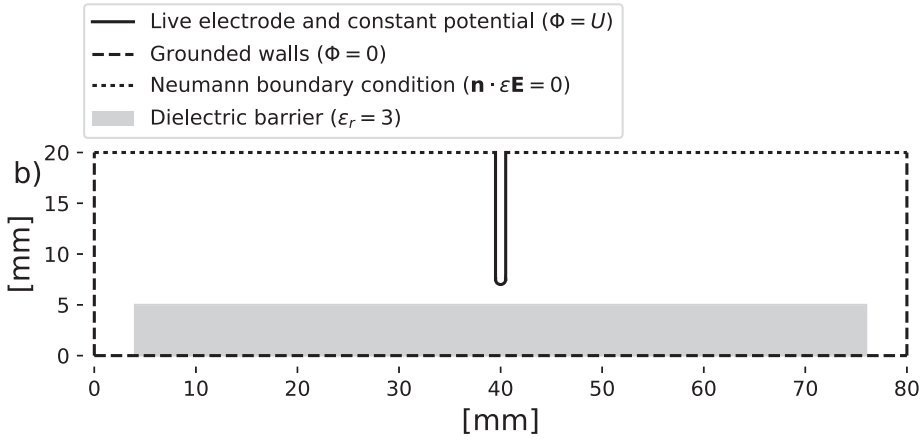

(b)

Figure 4.5: Simulation domains (16 cm^2) for drift-diffusion simulations. The simulations are 2D planar, meaning that the dimensions are infinite into and out of the paper. So the geometries are blade-barrier-plane gaps. In a) (Geometry G1, see table 4.1), the influence of photoemission was studied. In b) (Geometry G2, see table 4.1), the influence of applied voltage was studied.

Chapter 5

Results and Discussions

In this chapter, the research questions presented in the introduction will be discussed in light of the results. The results include pre-breakdown and breakdown diagnostics of LI-stressed rod-plane gaps and rod-barrier-plane gaps, surface charge measurements, and simulations of surface charging by streamers. The research questions are:

- What are the characteristics of breakdown in LI-stressed short rod-plane air gaps with and without dielectric barriers? (discussed in section 5.1).
- How can surface charge distributions on dielectrics after discharges in short LI-stressed rod-plane air gaps be predicted? (discussed in section 5.2).
- What are the dynamics of surface charging in short LI-stressed non-uniform air gaps? (discussed in section 5.3).

For more details on the results, the reader is referred to the papers.

5.1 Breakdown characteristics

What are the characteristics of breakdown in LI-stressed short non-uniform air gaps with and without dielectric barriers?

5.1.1 Primary streamers

The first discharge event captured on camera in the rod-plane gaps is always streamer inception from the rod and propagation towards ground. Streamers reaching ground do not, however, directly cause breakdown in non-uniform electric fields [28], [110].

Streamer discharges are challenging to capture on camera as they are faint and move fast (a few mm/ns) (fig. 5.2). In fig. 5.2, an image series of streamer propagation in a rod-barrier-plane gap is shown. Streamers start from the rod in the first frame, and propagate towards ground (reaching ground in frame 5 with a speed of around 2 mm/ns). The positioning of the frames relative to the applied lightning impulse is also shown (fig. 5.2b).

In fig. 5.1, the 50 % streamer inception voltage is reasonably estimated with the inception integral eq. (2.5). Note: A higher field inhomogeneity (smaller rod radius) leads to lower inception voltages.

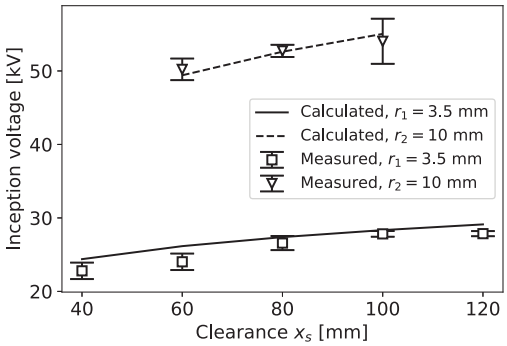

Figure 5.1: 50 % inception voltages (and standard deviations) with calculations (eq. (2.5)) for short rod-plane air gaps subject to positive LI stress. Data from paper II. Rod-plane gaps without barriers.

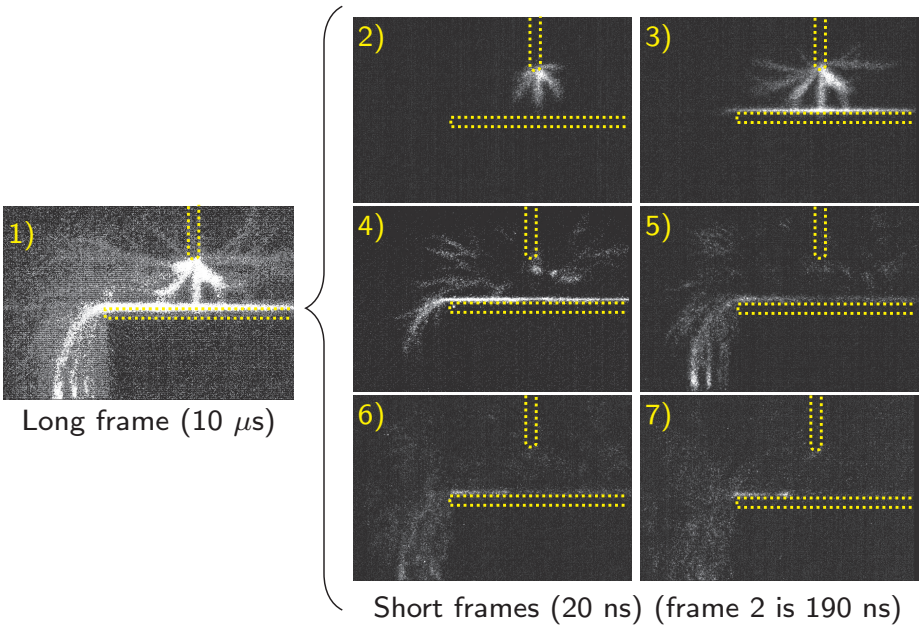

(a)

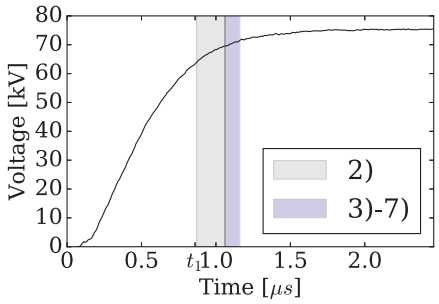

(b)

Figure 5.2: Streamer propagation in a rod-plane air gap with a dielectric barrier, from paper I. 75.36 kV applied, no BD. 60 mm gap, barrier surface at 40 mm, 40 mm overhang. a) Image frames b) applied voltage shape, with shaded columns indicating positioning of the short camera frames 2-7 relative to impulse voltage shape. t_1 indicates start of frames.

5.1.2 Leader-type discharges

In most high-voltage literature, it is stated that short (ca. $< 1\,\mathrm{m}$) atmospheric air gaps under $1.2/50\,\mu\mathrm{s}$ LI do not normally support leader discharges [7], [35], [111]. However, in the recent work by Kojima et al [31], so-called leader-type breakdowns in short rod-plane air gaps are reported. Even more recently, Seeger et al. demonstrated that breakdown data for short, non-uniform gaps can be reasonably estimated with a one-dimensional leader model [28] (see also section 2.6.3).

It was shown in paper II and IV that leader-like discharges can cause BD in short rod-plane air gaps (see e.g. fig. 5.3). At the 50 % BD voltage level, leader-type channels are the dominating mode of breakdown for gaps larger than ca. 40 mm. In images, the leader (or leader-like) signature is a luminous channel, with a cloud of streamers emanating from the front of the channel [16]. Leader-like discharges are also recognizable through characteristics such as propagation speed, induced current, luminosity and spectra. In paper IV, it was shown that the current and velocity relationship was leader-like (see fig. 5.4, where it is shown that the measured current and velocities are within the empirical leader velocity and current relation eq. (2.4)).

In paper II, different light filters were used on the PMT to characterize the discharges (see fig. 5.3). Although the leader-type channels were more luminous, both streamers and leader-type channels emitted light from ultra-violet to infra-red. It was therefore not possible to distinguish these based on the emitted light ranges only. In fig. 5.3, an image series of the development from streamer inception to leader-type channel breakdown with the corresponding voltage, current and PMT measurements is shown.

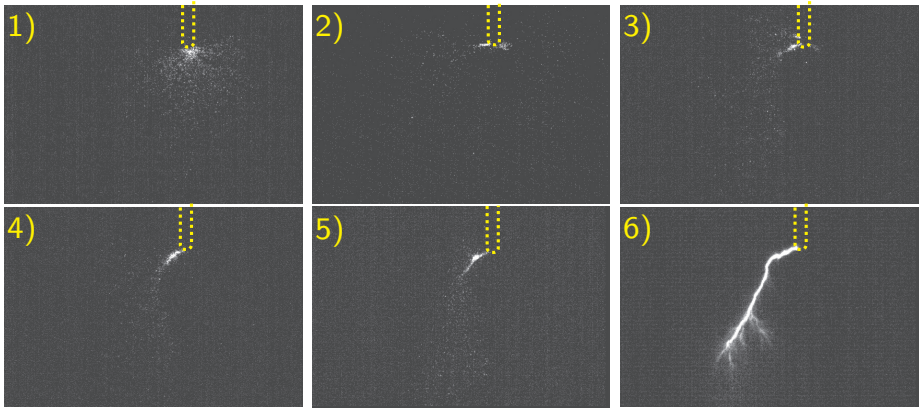

(a)

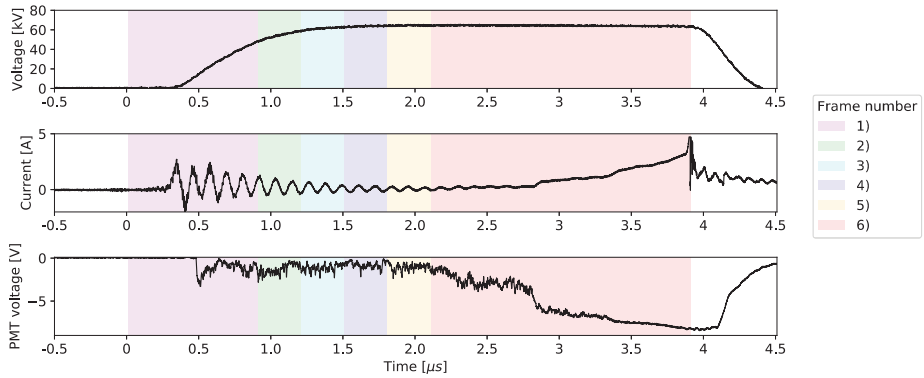

(b)

Figure 5.3: Breakdown in a 80 mm rod-plane gap (rod radius 3.5 mm) by a leader-type channel, 65.71 kV applied, from paper II. a) Frames b) Voltage (top) Current (middle) and PMT (bottom) oscilloscope traces. The PMT senses light with wavelength 495-650 nm. Shaded columns indicate positioning of the image frames relative to the electrical signals. In frame 1, streamers can be observed spreading from the rod tip. The streamers are observable in the PMT trace too. In frames 2-5, a streamer channel is heated. The resulting leader-type channel is observed in frame 6. Breakdown (voltage collapse) follows directly after frame 6.

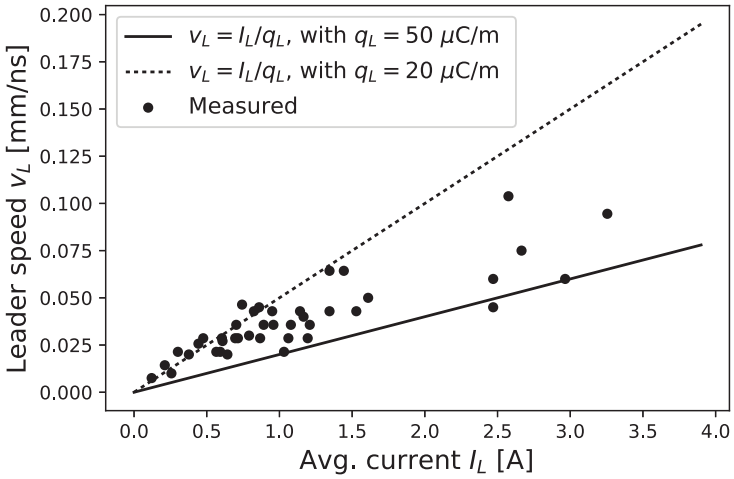

Figure 5.4: Leader-type channel speed as a function of measured current, from paper IV. The current-velocity relationship in short rod-plane air gaps is leader-like (predictions with eq. (2.4) shown). 41 data points plotted, from different 60 mm rod-plane gaps with and without a dielectric barrier. The barrier surface was 40 mm above ground, and the overhang was varied (see paper IV for details).

5.1.3 Sparks (secondary streamer breakdown)

If the distances are short enough, breakdown by streamers directly (secondary streamer BD) can occur (see fig. 2.5). This was also shown in [31]. With a larger rod radius, or a shorter gap distance (or both), the spark mechanism was observed in this work as well (fig. 5.5). In fig. 5.5, such a breakdown series is shown for a 20 mm gap with 10 mm rod radius. Directly after the primary streamer inception (frame 1), secondary streamer and channel heating activity (frames 2-4) lead to breakdown (frames 5 and 6).

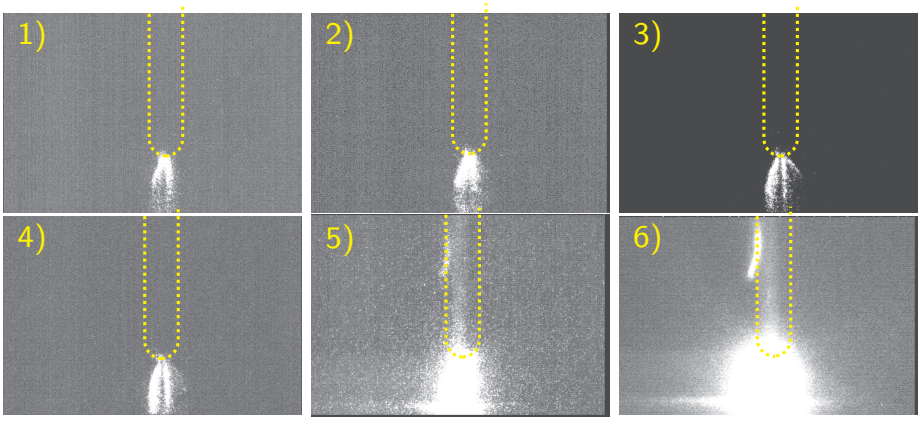

(a)

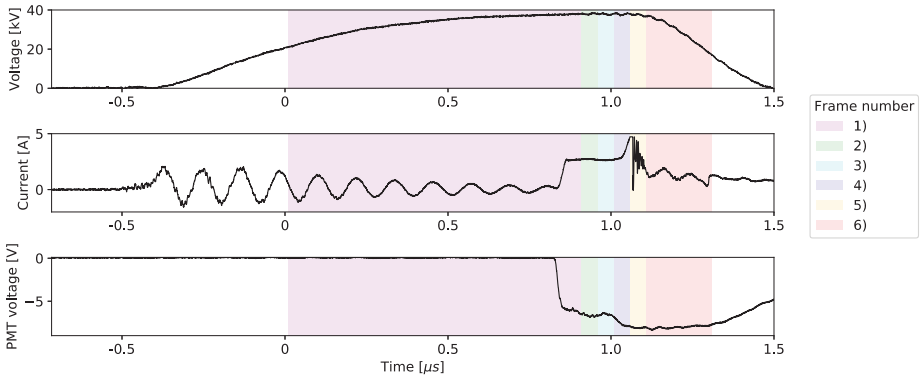

(b)

Figure 5.5: Breakdown in a 20 mm rod-plane gap (rod radius 10 mm) by the spark mechanism, 39 kV applied, from paper II. a) Frames b) Voltage (top) Current (middle) and PMT (bottom) oscilloscope traces. The PMT senses light with wavelength 610-850 nm. Shaded columns indicate positioning of the image frames. In frame 1, streamers can be observed spreading from the rod tip. The streamers are observable in the PMT trace too. In frames 2-4, the streamer channels are heated. Breakdown occurs in frame 5, as the spark gap is triggered in this frame in the current trace. No leader-type channel initiation is observed.

5.1.4 Negative breakdown

Negative BD is known to typically involve a system of streamers and leaders of both polarities [34]. Such phenomena were observed during the course of this work as well. In the negatively stressed rod-plane gaps, the breakdown channel starts from the ground plane, and not the rod, see fig. 5.6. As it starts from the ground, it is cathode-directed, i.e. a positive leader-type channel.

In frame 1 in fig. 5.6, streamers can be observed spreading from the rod tip. Nothing happens in frame 2, but in frame 3 and 4 there is again discharge activity, before a leader-type channel starts from the ground plane in frame 5. Breakdown (voltage collapse) then follows a few hundred ns after frame 5.

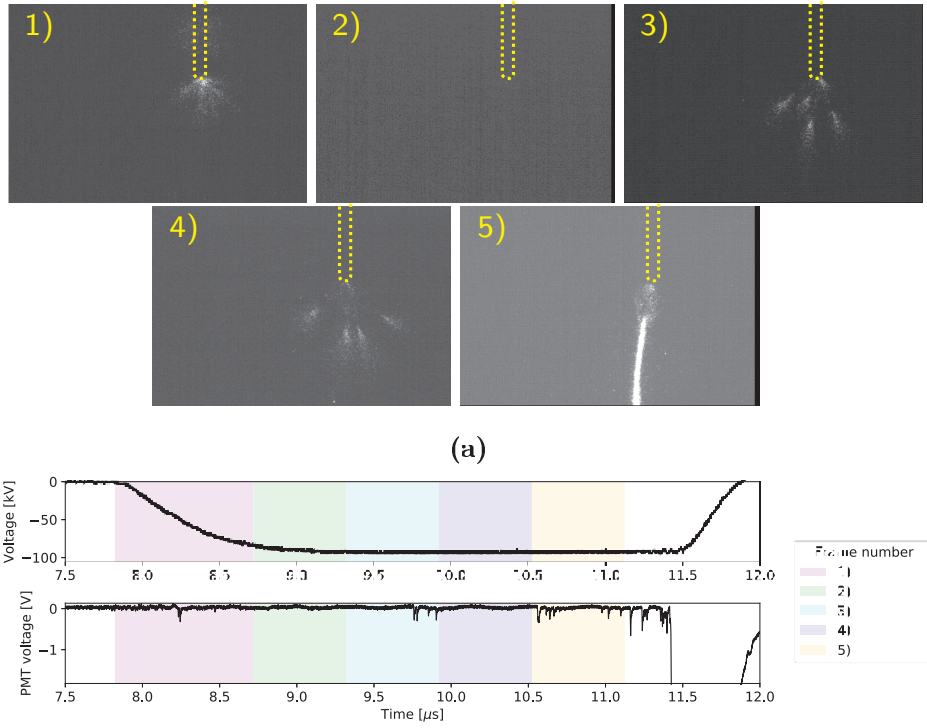

Figure 5.6: Breakdown in a 60 mm rod-plane gap (rod radius 3.5 mm), −96 kV applied (not included in papers). a) Frames b) Voltage (top) and PMT (bottom) oscilloscope traces. The PMT senses light with wavelength 380-680 nm, but the light into the PMT is strongly attentuated with a paper filter. Shaded columns indicate positioning of the image frames. In frame 1, negative streamers can be observed spreading from the rod tip. Nothing happens in frame 2, but in frame 3 and 4 there is again discharge activity, before a leader-type channel starts from the ground plane in frame 5.

5.1.5 Breakdown voltage measurements in rod-plane gaps

The 50 % BD voltages for the tested rod-plane gaps are shown in fig. 5.7. They increase linearly, and the corresponding linear regressions are within the wide predictions of the streamer stability criterion eq. (2.7). The dependency on rod geometry is only significant at low clearances (fig. 5.7a), where streamer BD (secondary streamer crossing and heating) comes into play for the weakly uniform fields (gap < 40 mm).

While the slope of positive BD is the typical 0.4-0.6 kV/mm, the slope of negative BD is steeper, around 1.2 kV/mm. This is within expectations, as a higher background field is needed for negative streamer propagation (see section 2.3.3).

Equation (2.7) should be interpreted in terms of leader properties when the breakdown mechanism is leader-like. In [28], a leader propagation model is used to interpret breakdown data of short (< 1 m) non-uniform atmospheric air gaps under positive LI. It is concluded in [28] that the slope of ca. 0.5 kV/mm is likely explained by the complex heating mechanisms during leader propagation, rather than the streamer stability field.

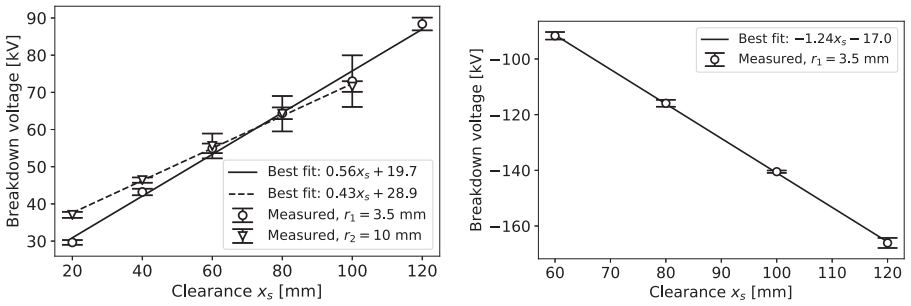

Figure 5.7: Breakdown statistics (50 % values with standard deviations) of rod-plane gaps, subject to positive and negative LI stress (paper II). Breakdown voltage increases linearly with slopes between ca. 0.4 to 0.6 kV/mm for positive (a) and between 1 to 1.5 kV/mm for negative(b) 1.2/50 µs LI, as expected [7], [19]. Linear regressions to the data sets also shown in the figure.

5.1.6 Dielectric barriers and positive breakdown

In fig. 5.8, an image series of breakdown by leader-type channel propagation around a dielectric barrier is shown with corresponding voltage, current and PMT curves. In frame 1, streamers propagate around the dielectric barrier, as in fig. 5.2. In frames 2 and 3, a channel further up on the rod is gradually heated, and the propagation of the resulting leader-type channel can be seen in frames 4 to 6.

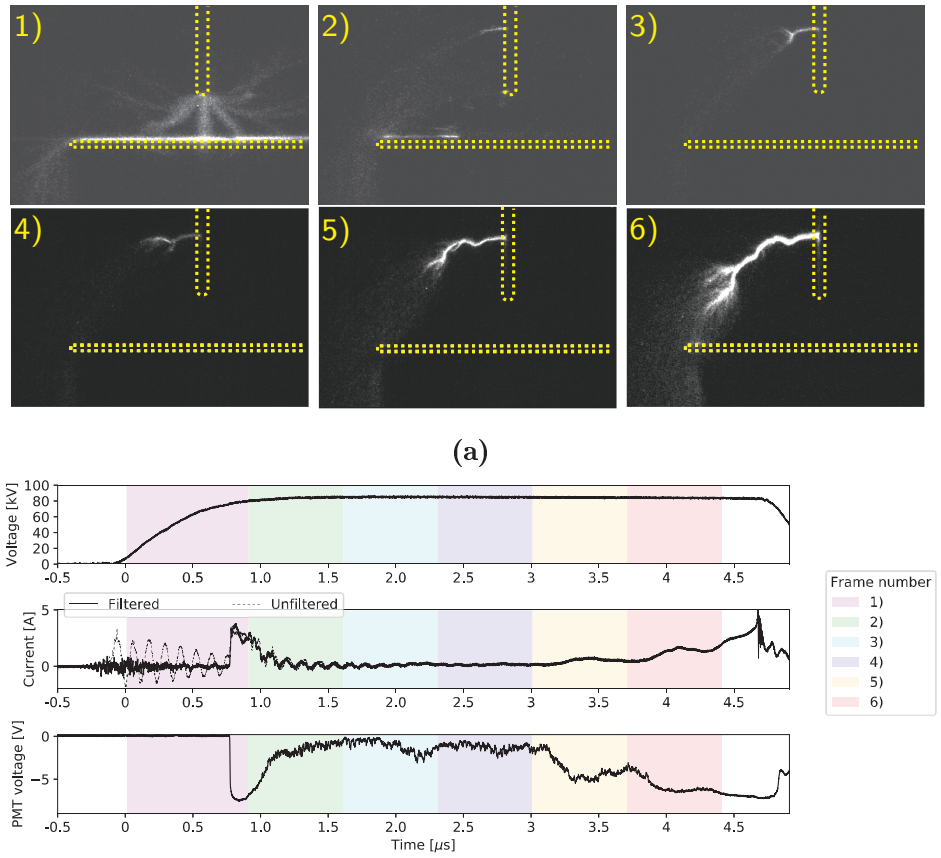

Figure 5.8: Breakdown in a 60 mm rod-plane gap (rod radius 3.5 mm) by a leader-type channel, 86 kV applied, from paper IV. Barrier surface at 40 mm, 60 mm overhang. a) Frames b) Voltage (top) Current (middle) and PMT (bottom) oscilloscope traces. The PMT senses light with wavelength 495-850 nm. Shaded columns indicate positioning of the image frames. In frame 1, streamers can be observed spreading from the rod tip. The streamers are observable in the PMT trace too. In frames 2-3, a streamer channel or stem is heated. The resulting leader-type channel is observed propagating in frames 4 to 6. Breakdown (voltage collapse) follows right after frame 6.

Arrested leader-type channel

In [112] it was shown that a dielectric barrier can impede secondary streamer BD and promote leader-type BD in a 30 mm rod-plane gap. The leader-type channel would then cause BD. In paper III, it was shown that a dielectric barrier may also impede and arrest a leader-type channel in a 60 mm rod-plane gap (fig. 5.9).

In fig. 5.9, no BD occurred, even though the leader-type channel bridged ca. 75 % of the gap distance. Probably, the intense surface charging by the streamer corona at the leader-type channel tip caused a field reduction that arrested the channel development. Accurate prediction models of the surface charging effects are needed to understand and predict such discharge suppression effects. One such prediction model for surface charge is discussed in section 5.2 (and papers V and VI), where measurements of the residual surface charge on a dielectric barrier after a LI are used to validate the model. The residual surface charge after the discharges in fig. 5.9 is also presented in section 5.2 (see fig. 5.14).

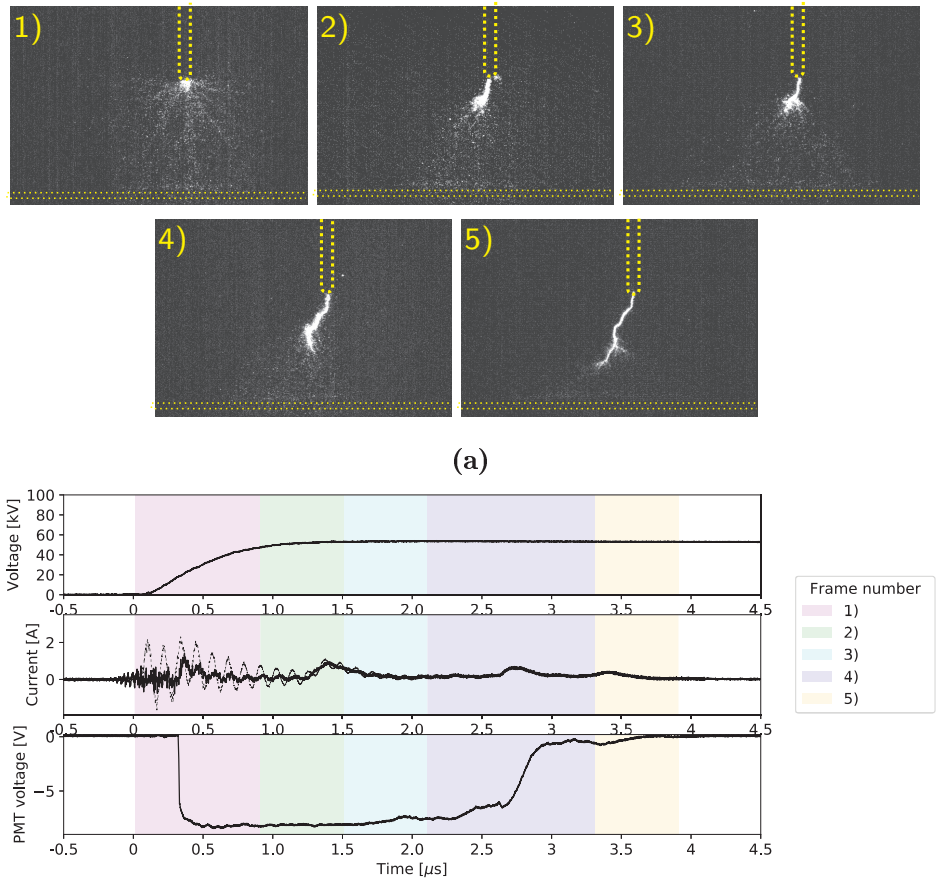

Figure 5.9: Streamers and arrested leader-type channel 60 mm rod-plane gap (rod radius 3.5 mm), no BD, 54.3 kV applied, from paper III. Barrier resting on the ground plane, centered (300 mm overhang). a) Frames b) Voltage (top) Current (middle) and PMT (bottom) oscilloscope traces. The PMT senses light with wavelength 180-610 nm. Shaded columns indicate positioning of the image frames. In frame 1, streamers can be observed spreading from the rod tip. The streamers are observable in the current and PMT trace too. In frames 2-5, a streamer channel is heated to a leader-type channel, which is arrested above the dielectric barrier in frame 5. No further discharge activity was observed.

5.1.7 Dielectric barriers and negative breakdown

Negative BD is known to typically involve a system of streamers and leaders of both polarities [34]. It was shown in paper IV that this is the case for rod-plane gaps with dielectric barriers as well.

In paper IV, it was shown that positive streamers (frames 2 and 4 in fig. 5.10a) may initiate from the ground plane after the negative streamers have charged the barrier (frame 1 in fig. 5.10a). The positive streamer channels may then become breakdown channels (frame 5 in fig. 5.10a).

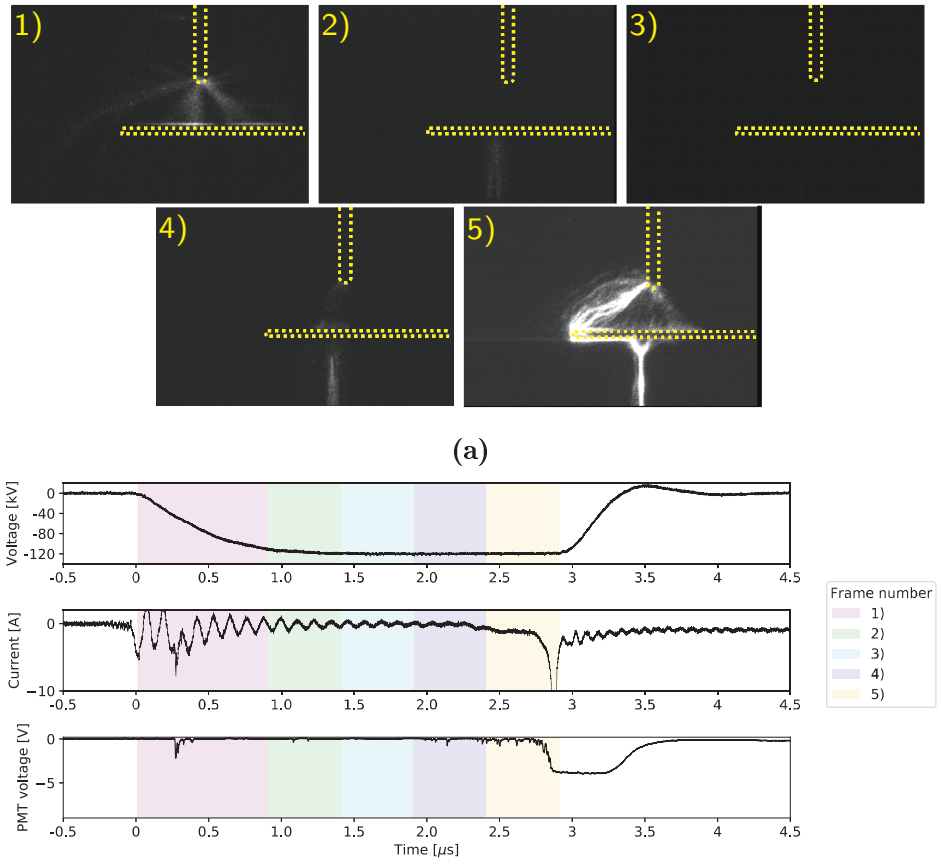

Figure 5.10: Breakdown in a 60 mm rod-plane gap (rod radius 3.5 mm) by a leader-type channel, −124 kV applied, from paper IV. Barrier surface at 40 mm, 40 mm overhang. a) Frames b) Voltage (top) Current (middle) and PMT (bottom) oscilloscope traces. The PMT senses light with wavelength 360-650 nm. Shaded columns indicate positioning of the image frames. In frame 1, streamers can be observed spreading from the rod tip. In frames 2-4, a positive streamer channel beneath the barrier is heated. The resulting leader-type channel is observed in frame 5. The frame ends right before the voltage collapse.

5.1.8 Breakdown voltage measurements in rod-plane gaps with a dielectric barrier

Breakdown voltages in rod-plane gaps with a dielectric barrier are presented in paper IV and fig. 5.11. The voltage values are largely aligned with eq. (2.7), when the minimum discharge path x_s (see fig. 2.6b) is used. This has also been shown in previous investigations, e.g. [51]. In addition to the mechanical obstruction, the dielectric barrier acquires surface charge, which screens the rod tip. This surface charge causes the leader-type channels to initiate higher up on the rod, see fig. 5.8.

For negative breakdown in rod-barrier-plane gaps, a linear increase of ca. 0.9 kV/mm is observed, which is close to the range of typical negative streamer stability fields $E_{\mathrm{st}-}$ [7].

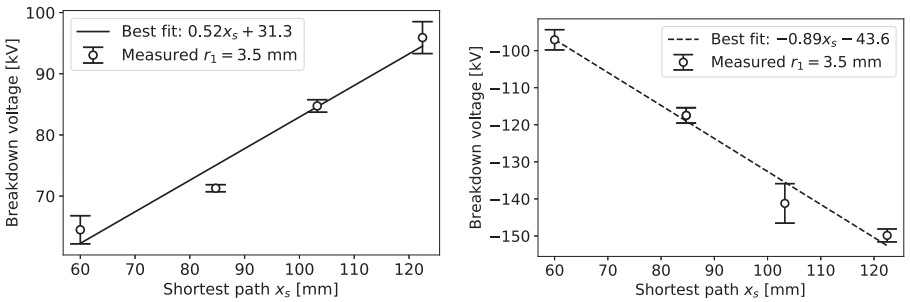

Figure 5.11: Breakdown voltages (50 % values with standard deviations) of rod-plane gaps with a dielectric barrier, subject to positive and negative LI stress (paper IV). The horizontal axis represents the shortest inter-electrode path. Linear regressions to the data sets also shown in the figure.

5.1.9 Summary

Pre-breakdown and breakdown phenomena in short LI-stressed non-uniform air gaps with and without dielectric barriers have been characterized with high-speed imaging, PMTs and fast current measurement.

High-speed images have shown that streamers propagate from the rod to the ground plane without causing breakdown. The leader-type channel is the governing breakdown mechanism at the 50 % level of the short LI-stressed non-uniform air gaps tested in this thesis. In weakly uniform or uniform fields, the spark (streamer breakdown) mechanism dominates. The breakdown voltages can be roughly estimated with the empirical stability field criterion (eq. (2.7)).

At negative lightning impulse polarity, the breakdown is characterized by a system of streamers and leader-type channels of both polarities. After the initial negative streamers from the rod, positive streamers initiate from the ground plane. The breakdown channel then starts from the ground plane.

A simulation model of leader breakdown (as in [28]) would aid the interpretation of the experimental results. The roughness of the electrodes was not controlled or monitored. More selective PMT light filters may reveal relevant details of the discharges. Moreover, the experiments were performed with a single dielectric barrier size and material. Varying barrier parameters such as thickness, permittivity and surface conductivity (see e.g. [113]) may reveal important aspects of the dielectric barrier influence on breakdown voltage.

5.2 Surface charge prediction

How can surface charge distributions on dielectrics after discharges in short LI-stressed rod-plane air gaps be predicted?

It was demonstrated in paper V and VI that surface charge predictions using saturation charge conditions (eqs. (2.8) and (2.10)) with the extensions described in section 4.1.2 fit reasonably well with the experimental results (figs. 5.12a and 5.12b below and fig. A.1 in appendix A). 9 rod-barrier-plane configurations were tested, and produced similar conclusions (see table A.1 in appendix A for details on these configurations). The model can be used to estimate charging from positive and negative streamers and back discharges. Back discharges are reverse discharges occurring at the LI tail. It was shown in paper III that they occur as pulses of some 100 kHz, and are observable as a faint glow on the rod. They influence the surface charge distribution, as shown in paper III, V, VI and VII.

Moreover, provoking discharges on the ground plane side leads to surface charge behaviour that is also, to some extent, predictable with the model (fig. 5.13).

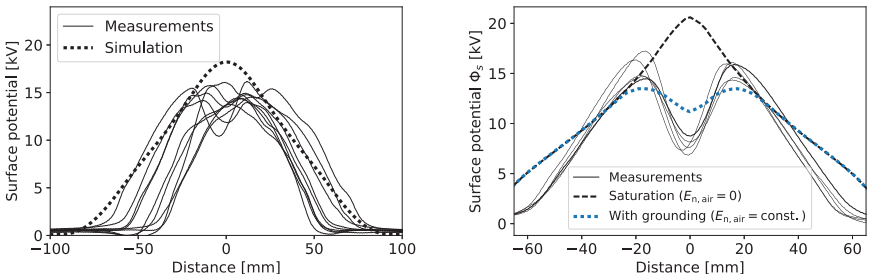

Figure 5.12: Surface potential close to saturation levels after a positive 35 kV LI (from papers V and VI) a) 15 mm gap, barrier on the ground plane, 3.5 mm rod radius. b) 10 mm gap, barrier on the ground plane, 2 mm rod radius. Back discharge signature ("volcano"-shape) and back discharge calculation (see section 4.1.2).

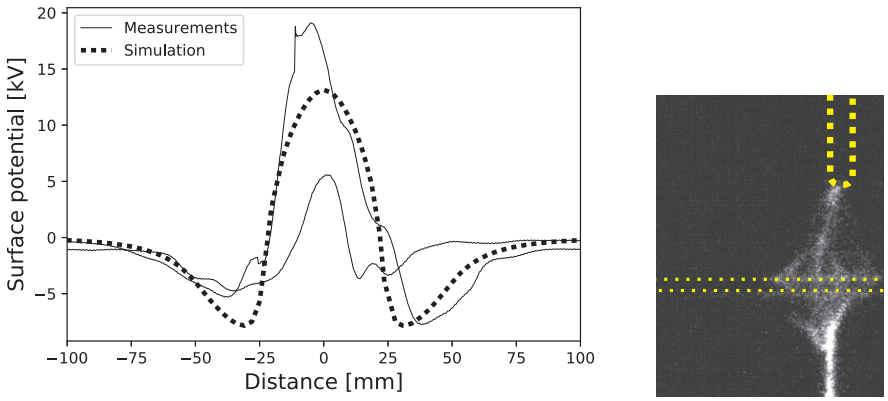

Figure 5.13: Saturation, −50 kV LI with measurement on the side of the barrier facing ground (from paper V and VI). 20 mm gap with 3.5 mm rod radius. Barrier surface at 15 mm. A small copper wire (radius ca. 1 mm, protruding ca. 2 mm) was placed on the ground plane to initate discharges on both sides of the dielectric barrier. a) The results agree qualitatively with the prediction (negative potential on the sides but positive in the middle), but the predictions are inaccurate. b) image of streamers on both sides of a dielectric barrier in a 60 mm gap, previously published in [89] (−100 kV impulse).

5.2.1 Charging by leader-type channels

Leaders or leader-type channels are highly conductive channels that can be more or less approximated as an extension of the high voltage electrode. As a a result, saturation charge evaluations based on the background field are inaccurate when leaders are present. Experimental results confirm this – see fig. 5.14 and paper V. Modeling the leader as an electrode may produce correct results, but this was not tested here.

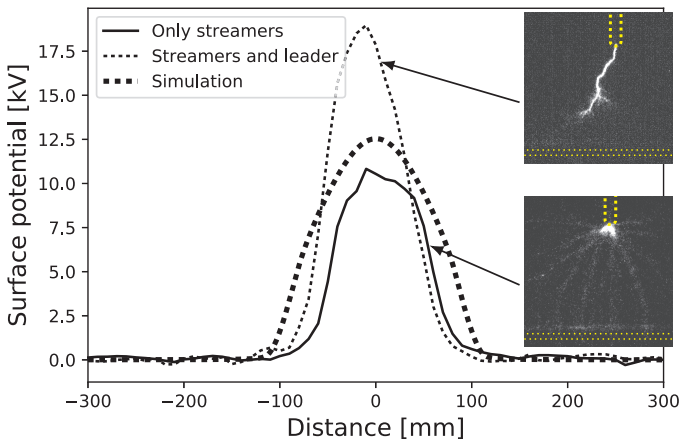

Figure 5.14: Leader-type channels lead to surface charge above saturation levels. Measured after a 54.3 kV impulse (see fig. 5.9). 60 mm gap, 3.5 mm rod radius, barrier resting on the ground plane. Leaders should be modeled as conductors, as discussed in paper V. Insets: accumulated discharge activity before measurement.

5.2.2 Charge decay

An important factor that influences these measurements is the surface charge decay. In paper V, it was shown that most charge disappears within a few hours, see fig. 5.15. Moving the barrier from the lightning impulse dock to the scanning dock (see fig. 3.4a) took around 2-3 minutes, in which time the charge decay could affect the measurement. One should therefore expect that the actual charge distributions during the LI are higher than the results indicate.

Influence of probe on charge decay

Initial decay measurements (paper III) suggested that the decay was negligible after 1000 min. These results were, however, misleading as it was discovered during the measurements in paper V that leaving the probe near

the barrier slows the charge decay significantly. The probe housing adjusts to the surface by zero-ing the electric field between the surface and the probe. Neutralization by gas ions is therefore stopped when the probe is close to the surface.

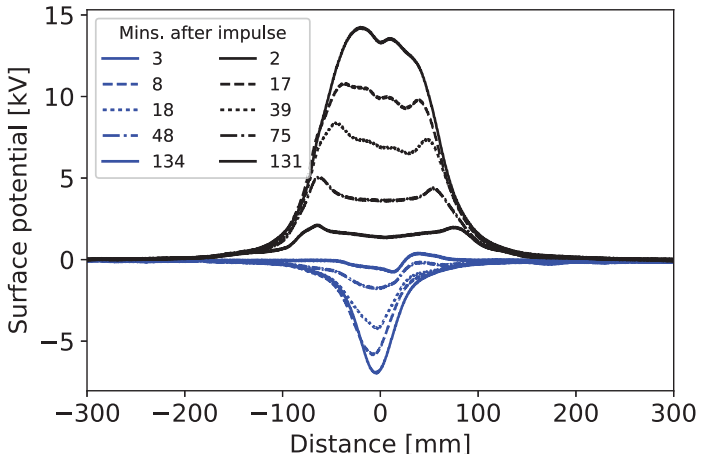

Figure 5.15: Charge decay measurements after a $\pm 50\,\mathrm{kV}$ lightning impulse. 35 mm rod-plane gap with a dielectric barrier, the surface of which was 15 mm above ground. Most of the surface charge disappears within a couple of hours.

5.2.3 Summary

The residual surface potential on a dielectric barrier after a 1.2/50 µs LI was measured. The results were analyzed with a simulation procedure based on saturation charge conditions (zero or constant normal electric field in air at the surface).

It was found that the measured distributions after primary streamers are well estimated with saturation charge conditions and streamer range estimates (see sections 2.7.2 and 4.1.2 for descriptions of the simulation procedure). Secondary phenomena such as inception suppression, back discharges and leader discharge may result in deviations from saturation charge. The residual potential distribution after a back discharge can be estimated by iteratively removing charge and equalizing the normal electric field.

Highly localized charge densities may exceed saturation, as the resolution of the scan was low, up to 2 cm. Furthermore, the influence of the probe on the measured surface potential was neglected, which may lead to measurement errors of a few % [99], [101]. Moreover, the surface charge distribution may have decayed from the initial state during the time delay (2-3 minutes) between LI application and the surface potential scan. A study of the influence of dielectric barrier properties (e.g. surface conductivity) on surface charging would also be beneficial.

5.3 Surface charge dynamics

What are the dynamics of surface charging by streamers in short LI-stressed non-uniform air gaps?

In paper VII, it was shown that drift-diffusion simulations of 2D planar blade-barrier-plane gaps (fig. 5.17) produce similar charging behavior as the experiments in paper V and VI. Moreover, the dynamics of the surface charging mechanisms during the simulated positive surface streamer propagation was clarified. It was shown that the simulated streamers produce enough charge carriers to charge the surface to saturation (zero normal electric field in air at the air-dielectric interface), and that the recombination rate of these charge carriers is not fast enough to prevent saturation. Development towards saturation charge was observed during tens of ns as the streamer propagates along the barrier (fig. 5.16). Furthermore, the streamer range and velocity were consistent with the stability field estimate (eq. (2.11)) and experiments.

Although ion drift is the dominating surface charging mechanism in the model, photoemission near the streamer head also contributes, as every emitted electron leaves behind an electron hole. As discussed in section 4.2.3, the value of the photoemission yield γ is not well documented, with estimates ranging from 10^{-7} to 1 for polymers. $\gamma = 0.1$ and $\gamma = 10^{-6}$ were used in the simulations here to study the general influence of photoemission on streamer and surface charge dynamics. It was shown in the simulations in paper VII that photoemission increases the charging rate, see fig. 5.16a. In the figure, surface charge density snapshots during simulations with high ($\gamma = 0.1$) and low ($\gamma = 10^{-6}$) photoemission yields are shown. It was also demonstrated in the simulations in paper VII that a higher photoemission yield γ causes the streamer to propagate closer to the dielectric barrier surface.

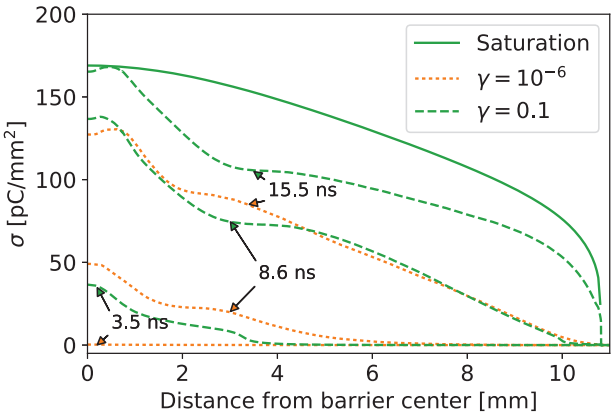

(a)

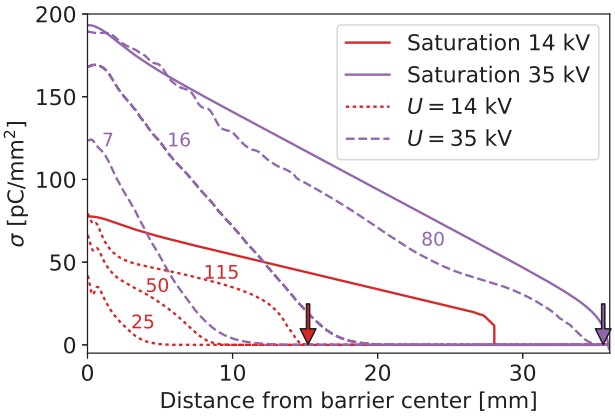

(b)

Figure 5.16: Surface charge densities (dotted and broken lines) evolve toward saturation (solid lines) in tens of nanoseconds in drift-diffusion simulations. See section 4.2.4 for details on simulation domains. a) Geometry G1 (fig. 4.5a), high photoemission yield γ (see eq. (4.9)) increases surface charging rate. b) Geometry G2 (fig. 4.5a): Two voltage levels, 14 kV and 35 kV applied. At 14 kV, the streamer stability range (eq. (2.11)) is shorter than the barrier width, so the saturation condition (red solid line) is only applied to a part of the barrier. The simulations were stopped before the streamer reached ground. Vertical arrows mark the position of the streamer head at the simulation end. Numerals indicate elapsed simulation time in ns.

5.3.1 Streamer propagation along a dielectric surface

As the streamer charges the surface, it reduces the electric field strength in air below the ionization threshhold ($E_{\mathrm{cr}} = 2.6\,\mathrm{kV/mm}$ [16]), see fig. 5.17. In the figure, snapshots of the electric field strengths in regions with $|\mathbf{E}| \geq 2.6$ kV/mm during streamer propagation are shown. The streamer initates from the rod, hits the dielectric surface and propagates along the surface towards ground. Ionization activity is sustained near the streamer head, but the field strength in air behind the streamer head is reduced below the ionization threshold (and consequently increased inside the solid dielectric).

Figure 5.17: Simulation: electric field strength, applied 35 kV. The field is only plotted in regions where $|\mathbf{E}| \geq 2.6$ kV/mm, to visualize the position of the streamer head. The maximum field strength in air is located at the streamer head (value of maximum field strength indicated in each plot). The streamer slows down as it propagates into low background field regions. a) $t = 0$ ns (background field), b) $t = 0.3$ ns (streamer initiated from the blade tip, propagating towards the barrier), c) $t = 7$ ns (streamer propagation along barrier) d) $t = 16$ ns, e) $t = 59$ ns, f) $t = 80$ ns (streamer at the barrier edge). Entire simulation domain shown in fig. 4.5b.

Streamer velocity

Streamer velocities from 0.1 up to a few mm/ns are typical experimental values in high voltage literature [7], [21] and similar velocities are seen here in figs. 5.17 and 5.18. The velocity of the streamer depends on the applied voltage, see fig. 5.18. According to the streamer range hypothesis (eq. (2.11)), the 14 kV simulation in fig. 5.18 should not propagate further than 28 mm. The simulation was, however, stopped due to excessive computation time before the streamer reached the stability limit. It did, however, appear to slow down to a halt, in support of the streamer range concept of eq. (2.11). As the streamer moves into lower-field regions, it slows down (this can also be seen in fig. 5.17).

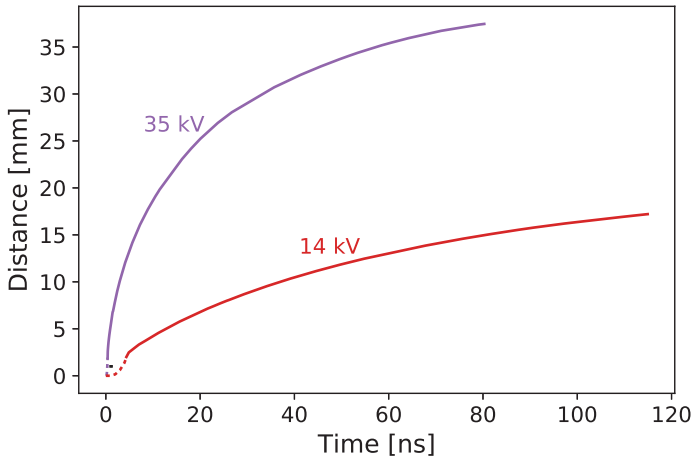

Figure 5.18: Streamer distance vs time, geometry G2 (see fig. 4.5b). The 35 kV streamer reaches the barrier edge, but the 14 kV simulation was not run for long enough, and slows down significantly, in support of the stability field concept (eq. (2.11)). Dotted lines indicate propagation in the air gap, solid lines along the barrier.

5.3.2 Back discharges

Finally, the influence of back discharges on the surface charge distribution was reproduced qualitatively (fig. 5.19). When grounding the HV electrode, the surface charge field distortion may lead to the inception of a new discharge from the electrode tip. When the back discharge hits the surface, it affects the surface charge distribution. The result is a characteristic "volcano"-shaped surface potential (as measured in fig. 5.12b and [59]) and negative surface charging directly beneath the electrode, as observed in [59]. This influence of back discharges was demonstrated in paper VII with the drift-diffusion simulation model as well, see fig. 5.19.

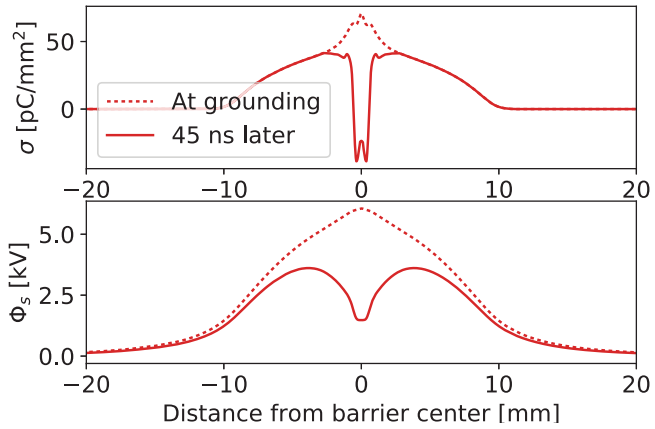

Figure 5.19: Drift-diffusion simulations reproduce the influence of back discharges – volcano-shaped surface potential. 14 kV applied. The simulation is restarted after 61.2 ns, with the obtained surface charge distribution, initial conditions for space charge ($10^{10}/\mathrm{m}^3$ electrons and positive ions) and a grounded HV rod. This results in a back discharge, which affects the surface charge distribution. Domain (G2) shown in fig. 4.5b. Upper plot: surface charge density σ. Lower plot: Surface potential Φ_s.

5.3.3 Summary

The dynamics of positive streamer propagation in 2D planar non-uniform electric fields near dielectric barriers was analyzed with drift-diffusion simulations.

Positive streamers charge dielectrics in cm-scale domains to saturation within tens of ns in the simulations. The surface charging during positive streamers is dominated by ion drift, although photo-emission near the streamer head also plays an important role. A high photoemissive yield causes the streamer to propagate closer to the surface.

It can be concluded that drift-diffusion simulation models reproduce experimentally observed characteristics (saturation charging, streamer velocity and range, back discharges) of streamer-dielectric interaction in atmospheric air.

The 2D planar simulation domain is an important limitation of this work. 2D cylindrical simulations would be closer to the experiments. Recent publications [74], [78], [114] have demonstrated that 2D cylindrical drift-diffusion simulations of streamers in hybrid air-solid insulation systems are well aligned with the experimentally observed streamer characteristics shown in paper I (e.g. the image series shown in fig. 5.2a). A comprehensive streamer modelling approach requires 3D, however, to include streamer branching effects (as in fig. 2.3 and [23], [115]). The 2D domain used in this thesis was also small (16 cm^2) compared with the experiments (high voltage lab, with grounded walls far from the set-up).

Chapter 6

Conclusions

The aim of this thesis has been to improve the understanding of hybrid-solid air insulation techniques. The results are valuable for the development of next generation medium voltage metal-enclosed SF_6-free switchgear insulation systems.

The work presented in this thesis contributes to a better understanding on LI breakdown mechanisms in short ($\leq$ 120 mm) non-uniform gaps in atmospheric air, and how these are affected by a polycarbonate dielectric barrier. Three research questions are discussed: (i) *What are the characteristics of breakdown in LI-stressed short non-uniform air gaps with and without dielectric barriers?* (ii) *How can surface charge distributions on dielectrics after discharges in short LI-stressed rod-plane air gaps be predicted?* and (iii) *What are the dynamics of surface charging by streamers in short LI-stressed non-uniform air gaps?* A summary of the main contributions is given below:

(i) **Breakdown characteristics:** The pre-breakdown and breakdown development in short LI-stressed rod-plane air gaps with and without a dielectric barrier has been clarified with high-speed images, photomultipliers and fast current measurements. It has been demonstrated that leader-type discharges dominate breakdown around the 50 % level in short rod-plane gaps. It has also been shown that dielectric barri-

ers may arrest leader-type channels in short rod-plane gaps, and that negative LI breakdown involves streamers and leader-type channels of both polarities.

(ii) **Surface charge prediction:** Surface charging of a dielectric barrier by streamers in rod-plane gaps has been investigated with surface potential measurements. It has been shown that the surface charge levels after a LI can be reasonably predicted with the saturation charge condition (zero normal electric field at the air side of the air-dielectric interface). The range of the streamer charging can be estimated with the streamer stability field. A procedure has also been proposed to estimate the surface charging effect of back discharges (restoring discharges occuring at the LI tail). It has, however, been shown that the model under-predicts surface charging by leader-like discharges, as leaders should be modeled as an extension of the live electrode.

(iii) **Surface charge dynamics:** A drift-diffusion streamer simulation model has been used to clarify the dynamics of surface charging by positive streamers in $16\,\mathrm{cm}^2$ 2D planar domains. Experimentally observed characteristics of streamer-dielectric interaction are reproduced with the model. The characteristics include positive streamer velocity, range and surface charge magnitudes. The simulated positive streamers charge dielectric surfaces to saturation within tens of ns. The streamer-exposed surface is charged mainly by drifting ions from the streamer channel, but also by electron emission processes from the dielectric surface.

Chapter 7

Further work

It is hoped that the work presented here could be used as a basis for further investigations into the science and engineering applications of dielectric barriers. Possible topics for future research include:

- Dielectric barriers in other atmospheric conditions or other gases
- Determination of transition regions in rod-plane gaps from leader-type breakdown mechanism to spark mechanism as functions of rod geometry, gap clearance and applied voltage
- Optimal design of dielectric barrier-insulated system (material shapes/position, material properties, multiple barriers)
- 3D drift-diffusion simulations of branching streamers propagating over dielectric surfaces
- Drift diffusion simulations and experiments with streamers propagating near surfaces with different material shapes and properties (e.g. different conductivity, permittivity or surface roughness)
- Improvement and validation of drift-diffusion plasma kinetics models
- Extension of the drift-diffusion model to account for secondary discharge phenomena (leaders and secondary streamers)

Bibliography

[1] *Regulation (EU) no 517/2014 of the european parliament and of the council of 16 april 2014 on fluorinated greenhouse gases and repealing regulation (EC) no 842/2006 text with EEA relevance*, May 20, 2014.

[2] E. Lakervi and E. J. Holmes, *Electricity distribution network design*, 21. IET, 1995.

[3] (). MV GIS ring main units and compact switchgear SafeRing air / SafePlus air - gas insulated switchgear (switchgear) | ABB, [Online]. Available: https://new.abb.com/medium-voltage/switchgear/gas-insulated-switchgear/iec-gis-rmu-for-secondary-distribution/iec-gas-insulated-ring-main-unit-safering-air (visited on 09/26/2018).

[4] M. Rabie and C. M. Franck, "Assessment of eco-friendly gases for electrical insulation to replace the most potent industrial greenhouse gas SF6," *Environmental Science & Technology*, vol. 52, no. 2, pp. 369–380, Jan. 16, 2018, ISSN: 0013-936X.

[5] X. Li, H. Zhao, and A. B. Murphy, "SF 6 -alternative gases for application in gas-insulated switchgear," *Journal of Physics D: Applied Physics*, vol. 51, no. 15, p. 153 001, 2018, ISSN: 0022-3727.

[6] A. Beroual and A. M. Haddad, "Recent advances in the quest for a new insulation gas with a low impact on the environment to replace sulfur hexafluoride (SF6) gas in high-voltage power network applications," *Energies*, vol. 10, no. 8, p. 1216, Aug. 16, 2017.

[7] A. Küchler, *High Voltage Engineering: Fundamentals-Technology-Applications*. Springer, 2017.

[8] W. J. Dixon and A. M. Mood, "A method for obtaining and analyzing sensitivity data," *Journal of the American Statistical Association*, vol. 43, no. 241, pp. 109–126, 1948, ISSN: 0162-1459.

[9] International Electrotechnical Commission, "IEC 62271-1 high voltage switchgear and controlgear part 1: Common specifications," 2008.

[10] J. S. Townsend, "The conductivity produced in gases by the motion of negatively-charged ions," *Nature*, vol. 62, no. 1606, p. 340, 1900.

[11] Petcharaks, Komson, "Applicability of the streamer breakdown criterion to inhomogenous gas gaps," PhD thesis, 1995.

[12] H. Raether, "Die Entwicklung der Elektronenlawine in den Funkenkanal," *Zeitschrift für Physik*, vol. 112, no. 7, pp. 464–489, Jul. 1939, ISSN: 0044-3328.

[13] L. B. Loeb and J. M. Meek, *The mechanism of the electric spark*. Stanford University Press, 1941.

[14] J. M. Meek, "A theory of spark discharge," *Physical Review*, vol. 57, no. 8, pp. 722–728, Apr. 15, 1940, ISSN: 0031-899X.

[15] G. A. Dawson and W. P. Winn, "A model for streamer propagation," *Zeitschrift für Physik*, vol. 183, no. 2, pp. 159–171, Apr. 1, 1965, ISSN: 0044-3328.

[16] I. Gallimberti, "The mechanism of the long spark formation," in *Journal De Physique, Colloquium C*, vol. 7, 1979, pp. 193–250.

[17] U. Ebert, W. v. Saarloos, and C. Caroli, "Propagation and structure of planar streamer fronts," *Physical Review E*, vol. 55, no. 2, pp. 1530–1549, Feb. 1, 1997, ISSN: 1063-651X, 1095-3787.

[18] N. Y. Babaeva, A. N. Bhoj, and M. J. Kushner, "Streamer dynamics in gases containing dust particles," *Plasma Sources Science and Technology*, vol. 15, no. 4, p. 591, 2006, ISSN: 0963-0252.

[19] F. H. Kreuger, *Industrial high voltage: electric fields, dielectrics, constructions*. Delft University Press, 1991.

[20] N. L. Allen and P. N. Mikropoulos, "Dynamics of streamer propagation in air," *Journal of Physics D: Applied Physics*, vol. 32, no. 8, p. 913, 1999, ISSN: 0022-3727.

[21] ——, "Streamer propagation along insulating surfaces," *IEEE Transactions on Dielectrics and Electrical Insulation*, vol. 6, no. 3, pp. 357–362, Jun. 1999, ISSN: 1070-9878.

[22] U. Ebert, S. Nijdam, C. Li, A. Luque, T. Briels, and E. v. Veldhuizen, "Review of recent results on streamer discharges and discussion of their relevance for sprites and lightning," *Journal of Geophysical Research: Space Physics*, vol. 115, A7 2010, ISSN: 2156-2202.

[23] R. Marskar, "Adaptive multiscale methods for streamer discharges in 3d," *arXiv:1809.08857 [physics]*, Sep. 24, 2018. arXiv: 1809.08857.

[24] R. Morrow, "The theory of positive glow corona," *Journal of Physics D: Applied Physics*, vol. 30, no. 22, p. 3099, 1997, ISSN: 0022-3727.

[25] R. Morrow and T. R. Blackburn, "Burst pulses and secondary streamers from positive points," *Journal of Physics D: Applied Physics*, vol. 35, no. 24, p. 3199, 2002, ISSN: 0022-3727.

[26] S. Kumara, Y. Serdyuk, and S. Gubanski, "Charging of polymeric surfaces by positive impulse corona," *IEEE Transactions on Dielectrics and Electrical Insulation*, vol. 16, no. 3, pp. 726–733, Jun. 2009, ISSN: 1070-9878.

[27] M. Seeger, L. Niemeyer, and M. Bujotzek, "Leader propagation in uniform background fields in SF 6," *Journal of Physics D: Applied Physics*, vol. 42, no. 18, p. 185 205, 2009, ISSN: 0022-3727.

[28] M. Seeger, T. Votteler, J. Ekeberg, S. Pancheshnyi, and L. Sánchez, "Streamer and leader breakdown in air at atmospheric pressure in strongly non-uniform fields in gaps less than one metre," *IEEE Transactions on Dielectrics and Electrical Insulation*, vol. 25, no. 6, pp. 2147–2156, Dec. 2018, ISSN: 1070-9878.

[29] T. Suzuki, "Transition from the primary streamer to the arc in positive point-to-plane corona," *Journal of Applied Physics*, vol. 42, no. 10, pp. 3766–3777, Sep. 1, 1971, ISSN: 0021-8979.

[30] R. S. Sigmond, "The residual streamer channel: Return strokes and secondary streamers," *Journal of Applied Physics*, vol. 56, no. 5, pp. 1355–1370, Sep. 1, 1984, ISSN: 0021-8979.

[31] H. Kojima, K. Hotta, T. Kitamura, N. Hayakawa, A. Otake, K. Kobayashi, T. Kato, T. Rokunohe, and H. Okubo, "Classification of impulse breakdown mechanisms under non-uniform electric field in air," *IEEE Transactions on Dielectrics and Electrical Insulation*, vol. 23, no. 1, pp. 194–201, Feb. 2016, ISSN: 1070-9878.

[32] A. Agnihotri, W. Hundsdorfer, and U. Ebert, "Modeling heat dominated electric breakdown in air, with adaptivity to electron or ion time scales," *Plasma Sources Science and Technology*, vol. 26, no. 9, p. 095 003, 2017, ISSN: 0963-0252.

[33] A. Bondiou and I. Gallimberti, "Theoretical modelling of the development of the positive spark in long gaps," *Journal of Physics D: Applied Physics*, vol. 27, no. 6, p. 1252, 1994, ISSN: 0022-3727.

[34] V. Cooray, *The Lightning Flash*. IET, 2003, 600 pp., ISBN: 978-0-85296-780-5.

[35] I. Gallimberti, G. Bacchiega, A. Bondiou-Clergerie, and P. Lalande, "Fundamental processes in long air gap discharges," *Comptes Rendus Physique*, vol. 3, no. 10, pp. 1335–1359, Dec. 1, 2002, ISSN: 1631-0705.

[36] A. Pedersen, "On the electrical breakdown of gaseous dielectrics-an engineering approach," *IEEE Transactions on Electrical Insulation*, vol. 24, no. 5, pp. 721–739, Oct. 1989, ISSN: 0018-9367.

[37] G. V. Naidis, "Conditions for inception of positive corona discharges in air," *Journal of Physics D: Applied Physics*, vol. 38, pp. 2211–2214, 2005.

[38] P. Simka, E. Borrelli, and A. Blaszczyk, "Air breakdown at sharp edges," in *2018 IEEE 2nd International Conference on Dielectrics (ICD)*, Jul. 2018, pp. 1–4.

[39] A. Chvyreva, S. Pancheshnyi, T. Christen, and A. J. M. Pemen, "The raether-meek criterion for prediction of electrodeless discharge inception on a dielectric surface in different gases," *Journal of Physics D: Applied Physics*, 2018, ISSN: 1361-6463.

[40] T. Christen, "Streamer inception and propagation from electric field simulations," in *Conference on Scientific Computing in Electrical Engineering, SCEE*, 2012, pp. 11–14.

[41] M. Akyuz, L. Gao, V. Cooray, T. Gustavsson, S. Gubanski, and A. Larsson, "Positive streamer discharges along insulating surfaces," *IEEE Transactions on Dielectrics and Electrical Insulation*, vol. 8, no. 6, pp. 902–910, Dec. 2001, ISSN: 1070-9878.

[42] Y. V. Serdyuk, A. Larsson, S. M. Gubanski, and M. Akyuz, "The propagation of positive streamers in a weak and uniform background electric field," *Journal of Physics D: Applied Physics*, vol. 34, no. 4, p. 614, 2001, ISSN: 0022-3727.

[43] A. Pedersen and A. Blaszczyk, "An engineering approach to computational prediction of breakdown in air with surface charging effects," *IEEE Transactions on Dielectrics and Electrical Insulation*, vol. 24, no. 5, pp. 2775–2783, Oct. 2017, ISSN: 1070-9878.

[44] T. Christen, H. Böhme, A. Pedersen, and A. Blaszczyk, "Streamer line modeling," in *Scientific Computing in Electrical Engineering SCEE 2010*, Springer, 2012, pp. 173–181.

[45] F. A. M. Rizk, "A model for switching impulse leader inception and breakdown of long air-gaps," *IEEE Transactions on Power Delivery*, vol. 4, no. 1, pp. 596–606, Jan. 1989, ISSN: 0885-8977.

[46] M. Becerra and V. Cooray, "A simplified physical model to determine the lightning upward connecting leader inception," *IEEE Transactions on Power Delivery*, vol. 21, no. 2, pp. 897–908, Apr. 2006, ISSN: 0885-8977.

[47] S. M. Lebedev, O. S. Gefle, and Y. P. Pokholkov, "The barrier effect in dielectrics: The role of interfaces in the breakdown of inhomogeneous dielectrics," *IEEE Transactions on Dielectrics and Electrical Insulation*, vol. 12, no. 3, pp. 537–555, Jun. 2005, ISSN: 1070-9878.

[48] H. Roser, "Schirme zur erhöhung der durchschlagspannung in luft," *Elektrotech. Z.*, vol. H17, no. 411, 1932.

[49] E. Marx, "Der durchschlag der luft im unhomogenen elektrischen felde bei verschiedenen spannungsarten," *Elektrotech. Z.*, vol. H33, pp. 1161–1165, 1930.

[50] F. Mauseth, J. S. Jørstad, and A. Pedersen, "Streamer inception and propagation for air insulated rod-plane gaps with barriers," in *2012 Annual Report Conference on Electrical Insulation and Dielectric Phenomena (CEIDP)*, Oct. 2012, pp. 739–732.

[51] J. S. Jørstad, "Effect of barriers in air insulated rod-plane gaps," *61*, 2012.

[52] I. Gallimberti, G. Marchesi, and L. Niemeyer, "Streamer corona at an insulator surface," in *7th international symposium on High voltage engineering*, 1991, pp. 26–30.

[53] M. Ramesh, R. Summer, S. Singh, Y. Serdyuk, S. Gubanski, and S. Kumara, "Application of streamer criteria for calculations of flashover voltages of gaseous insulation with solid dielectric barrier," in *Chalmers Publication Library (CPL)*, 2013, pp. 1258–1263.

[54] A. A. Dubinova, "Modeling of streamer discharges near dielectrics," PhD thesis, TU Eindhoven, 2016.

[55] A. Kumada, S. Okabe, and K. Hidaka, "Residual charge distribution of positive surface streamer," *Journal of Physics D: Applied Physics*, vol. 42, no. 9, p. 095 209, 2009, ISSN: 0022-3727.

[56] N. L. Allen and D. C. Faircloth, "Corona propagation and charge deposition on a PTFE surface," *IEEE Transactions on Dielectrics and Electrical Insulation*, vol. 10, no. 2, pp. 295–304, Apr. 2003, ISSN: 1070-9878.

[57] S. Kumara, "Electrical charges on polymeric insulator surfaces and their impact on flashover performance," Doctoral thesis, Chalmers University of Technology, 2012.

[58] M. Sjöberg, "Charge accumulation in hybrid high voltage insulation," Doctoral thesis, Chalmers University of Technology, 2003.

[59] M. A. Abdul-Hussain and K. J. Cornick, "Charge storage on insulation surfaces in air under unidirectional impulse conditions," *IEE Proceedings A - Physical Science, Measurement and Instrumentation, Management and Education - Reviews*, vol. 134, no. 9, pp. 731–740, Nov. 1987, ISSN: 0143-702X.

[60] S. E. Cherukupalli, K. Tsuruta, and K. D. Srivastava, "Mechanism of prebreakdown spacer charging in non-uniform fields under unidirectional voltages," *IEEE Transactions on Electrical Insulation*, vol. 25, no. 4, pp. 642–654, Aug. 1990, ISSN: 0018-9367.

[61] V. I. Gibalov and G. J. Pietsch, "The development of dielectric barrier discharges in gas gaps and on surfaces," *Journal of Physics D: Applied Physics*, vol. 33, no. 20, p. 2618, 2000, ISSN: 0022-3727.

[62] H. Fujinami, T. Takuma, M. Yashima, and T. Kawamoto, "Mechanism and effect of DC charge accumulation on SF/sub 6/ gas insulated spacers," *IEEE Transactions on Power Delivery*, vol. 4, no. 3, pp. 1765–1772, Jul. 1989, ISSN: 0885-8977.

[63] F. H. Kreuger, *Industrial high DC voltage: 1. fields, 2. breakdowns, 3. tests*. Delft University Press, 1995, ISBN: 90-407-1110-0.

[64] R. Marskar, "An adaptive cartesian embedded boundary approach for fluid simulations of two- and three-dimensional low temperature plasma filaments in complex geometries," *arXiv:1809.03745 [physics]*, Sep. 11, 2018. arXiv: 1809.03745.

[65] M. M. Turner, "Computer simulation in low-temperature plasma physics: Future challenges," *Plasma Processes and Polymers*, vol. 14, no. 1, p. 1 600 121, 2017, ISSN: 1612-8869.

[66] Y. V. Serdyuk, S. M. Gubanski, J. Beattie, S. Schmidt, and K. Kreway, "Computational analysis of the electrostatic environment and flashover performance of a suspension link-stick for live-line work on high voltage power lines," *IEEE Electrical Insulation Magazine*, vol. 35, no. 1, pp. 7–22, Jan. 2019, ISSN: 0883-7554.

[67] R. Morrow and J. J. Lowke, "Streamer propagation in air," *Journal of Physics D: Applied Physics*, vol. 30, no. 4, p. 614, 1997, ISSN: 0022-3727.

[68] B. Bagheri, J. Teunissen, U. Ebert, M. M. Becker, S. Chen, O. Ducasse, O. Eichwald, D. Loffhagen, A. Luque, D. Mihailova, J.-M. Plewa, J. v. Dijk, and M. Yousfi, "Comparison of six simulation codes for positive streamers in air," *Plasma Sources Science and Technology*, 2018, ISSN: 1361-6595.

[69] J. Teunissen and U. Ebert, "Simulating streamer discharges in 3d with the parallel adaptive afivo framework," *Journal of Physics D: Applied Physics*, 2017, ISSN: 1361-6463.

[70] V. R. Soloviev and V. M. Krivtsov, "Mechanism of streamer stopping in a surface dielectric barrier discharge," *Plasma Physics Reports*, vol. 40, no. 1, pp. 65–77, Jan. 29, 2014, ISSN: 1063-780X, 1562-6938.

[71] W. Hua and K. Fukagata, "Influence of grid resolution in fluid-model simulation of nanosecond dielectric barrier discharge plasma actuator," *AIP Advances*, vol. 8, no. 4, p. 045 209, Apr. 1, 2018.

[72] Y. V. Serdyuk and S. M. Gubanski, "Computer modeling of interaction of gas discharge plasma with solid dielectric barriers," *IEEE Transactions on Dielectrics and Electrical Insulation*, vol. 12, no. 4, pp. 725–735, Aug. 2005, ISSN: 1070-9878.

[73] S. Singh, Y. V. Serdyuk, and S. M. Gubanski, "Simulations of electrical discharges in air using stabilized drift-diffusion model," *IEEE Transactions on Plasma Science*, vol. 46, no. 8, pp. 3031–3039, Aug. 2018, ISSN: 0093-3813.

[74] S. Singh and Y. V. Serdyuk, "Simulations of nonthermal electrical discharges in air over solid insulating barrier," *IEEE Transactions on Plasma Science*, pp. 1–7, 2018, ISSN: 0093-3813.

[75] J.-M. Plewa, O. Eichwald, O. Ducasse, P. Dessante, C. Jacob, N. Renon, and M. Yousfi, "3d streamers simulation in a pin to plane configuration using massively parallel computing," *Journal of Physics D: Applied Physics*, 2018, ISSN: 1361-6463.

[76] F. Pechereau, J. Jánský, and A. Bourdon, "Simulation of the reignition of a discharge behind a dielectric layer in air at atmospheric pressure," *Plasma Sources Science and Technology*, vol. 21, no. 5, p. 055 011, 2012, ISSN: 0963-0252.

[77] G. E. Georghiou, A. P. Papadakis, R. Morrow, and A. C. Metaxas, "Numerical modelling of atmospheric pressure gas discharges leading to plasma production," *Journal of Physics D: Applied Physics*, vol. 38, no. 20, R303, 2005, ISSN: 0022-3727.

[78] Y. V. Serdyuk and S. M. Gubanski, "Computer simulations of discharges along insulator surfaces," in *2017 IEEE Conference on Electrical Insulation and Dielectric Phenomenon (CEIDP)*, Oct. 2017, pp. 26–29.

[79] Y. Serdyuk, "Numerical simulations of non-thermal electrical discharges in air," *Lightning electromagnetics*, pp. 87–138, 2012.

[80] M. Sjöberg, Y. V. Serdyuk, S. M. Gubanski, and M. Å. S. Leijon, "Experimental study and numerical modelling of a dielectric barrier discharge in hybrid air–dielectric insulation," *Journal of Electrostatics*, vol. 59, no. 2, pp. 87–113, Sep. 2003, ISSN: 0304-3886.

[81] S. Pancheshnyi, M. Nudnova, and A. Starikovskii, "Development of a cathode-directed streamer discharge in air at different pressures: Experiment and comparison with direct numerical simulation," *Physical Review E*, vol. 71, no. 1, p. 016 407, Jan. 14, 2005.

[82] U. Ebert, C. Montijn, T. M. P. Briels, W. Hundsdorfer, B. Meulenbroek, A. Rocco, and E. M. v. Veldhuizen, "The multiscale nature of streamers," *Plasma Sources Science and Technology*, vol. 15, no. 2, S118, 2006, ISSN: 0963-0252.

[83] A. Bourdon, V. P. Pasko, N. Y. Liu, S. Célestin, P. Ségur, and E. Marode, "Efficient models for photoionization produced by non-thermal gas discharges in air based on radiative transfer and the helmholtz equations," *Plasma Sources Science and Technology*, vol. 16, no. 3, p. 656, 2007, ISSN: 0963-0252.

[84] S. Singh, "Computational framework for studying charge transport in high-voltage gas-insulated systems," Doctoral thesis, Chalmers University of Technology, 2017.

[85] D. Linhjell, L. E. Lundgaard, and M. Unge, "Positive third mode streamers in insulating oil," in *2017 IEEE 19th International Conference on Dielectric Liquids (ICDL)*, Jun. 2017, pp. 1–4.

[86] F. X. Hassion and R. H. Cole, "Dielectric properties of liquid ethanol and 2-propanol," *The Journal of Chemical Physics*, vol. 23, no. 10, pp. 1756–1761, Oct. 1, 1955, ISSN: 0021-9606.

[87] M. Prego, E. Rilo, E. Carballo, C. Franjo, E. Jiménez, and O. Cabeza, "Electrical conductivity data of alkanols from 273 to 333 k," *Journal of Molecular Liquids*, vol. 102, no. 1, pp. 83–91, Jan. 1, 2003, ISSN: 0167-7322.

[88] P. Rain and O. Lesaint, "Prebreakdown phenomena in mineral oil under step and ac voltage in large-gap divergent fields," *IEEE Transactions on Dielectrics and Electrical Insulation*, vol. 1, no. 4, pp. 692–701, Aug. 1994, ISSN: 1070-9878.

[89] M. Husøy, "Streamer charging of dielectric barriers in inhomogeneous air gaps," MSc, NTNU, Jun. 2017.

[90] S. Okabe and A. Kumada, "Measurement methods of accumulated electric charges on spacer in gas insulated switchgear," *IEEE Transactions on Power Delivery*, vol. 22, no. 3, pp. 1547–1556, Jul. 2007, ISSN: 0885-8977.

[91] A. Kumada, S. Okabe, and K. Hidaka, "Resolution and signal processing technique of surface charge density measurement with electrostatic probe," *IEEE Transactions on Dielectrics and Electrical Insulation*, vol. 11, no. 1, pp. 122–129, Feb. 2004, ISSN: 1070-9878.

[92] D. C. Faircloth, "Surface charge density and its influence on insulator flashover," PhD thesis, 2000.

[93] D. Faircloth and N. Allen, "High resolution measurements of surface charge densities on insulator surfaces," *IEEE Transactions on Dielectrics and Electrical Insulation*, vol. 10, no. 2, pp. 285–290, Apr. 2003, ISSN: 1070-9878.

[94] T. Rerup, G. Crichton, and I. McAllister, "Using the lambda; function to evaluate probe measurements of charged dielectric surfaces," *IEEE Transactions on Dielectrics and Electrical Insulation*, vol. 3, no. 6, pp. 770–777, Dec. 1996, ISSN: 1070-9878.

[95] A. Pedersen, G. Crichton, and I. McAllister, "The functional relation between partial discharges and induced charge," *IEEE Transactions on Dielectrics and Electrical Insulation*, vol. 2, no. 4, pp. 535–543, Aug. 1995, ISSN: 1070-9878.

[96] H. Ootera and K. Nakanishi, "Analytical method for evaluating surface charge distribution on a dielectric from capacitive probe measurement-application to a cone-type spacer in plusmn;500 kV DC-GIS," *IEEE Transactions on Power Delivery*, vol. 3, no. 1, pp. 165–172, Jan. 1988, ISSN: 0885-8977.

[97] Mauseth, Frank, "Charge accumulation in rod-plane air gap with covered rod," PhD thesis, Norwegian University of Science and Technology, 2006.

[98] J. Kindersberger and C. Lederle, "Surface charge decay on insulators in air and sulfurhexafluorid - part II: Measurements," *IEEE Transactions on Dielectrics and Electrical Insulation*, vol. 15, no. 4, pp. 949–957, Aug. 2008, ISSN: 1070-9878.

[99] A. Winter and J. Kindersberger, "Stationary resistive field distribution along epoxy resin insulators in air under DC voltage," *IEEE Transactions on Dielectrics and Electrical Insulation*, vol. 19, no. 5, pp. 1732–1739, Oct. 2012, ISSN: 1070-9878.

[100] S. Kumara, Y. V. Serdyuk, and S. M. Gubanski, "Surface charge decay on polymeric materials under different neutralization modes in air," *IEEE Transactions on Dielectrics and Electrical Insulation*, vol. 18, no. 5, pp. 1779–1788, Oct. 2011, ISSN: 1070-9878.

[101] M. Schueller, R. Gremaud, and C. Franck, "Accuracy of surface potential measurements of HVDC spacers," in *2014 International Conference on High Voltage Engineering and Application (ICHVE)*, Sep. 2014, pp. 1–4.

[102] J. Deng, H. Mu, G. Zhang, S. Matsuoka, A. Kumada, and K. Hidaka, "Residual charge distribution of surface leader discharge under positive impulse voltage," *IEEE Transactions on Plasma Science*, vol. 41, no. 4, pp. 999–1004, Apr. 2013, ISSN: 0093-3813.

[103] M. A. Noras, "Non-contact surface charge/voltage measurements: Capacitive probe—principle of operation," *Trek Application Note*, no. 3001, pp. 1–8, 2002.

[104] A. Blaszczyk, J. Ekeberg, S. Pancheshnyi, and M. Saxegaard, "Virtual high voltage lab," in *Scientific Computing in Electrical Engineering - SCEE 2016*, ser. Mathematics in Industry, U. Langer, W. Amrhein, and W. Zulehner, Eds., Heidelberg: Springer, 2018.

[105] H. J. M. Blennow, M. Å. S. Leijon, and S. M. Gubanski, "Active high voltage insulation," *Journal of Electrostatics*, vol. 55, no. 2, pp. 159–172, Jun. 2002, ISSN: 0304-3886.

[106] J. J. Lowke and R. Morrow, "Theoretical analysis of removal of oxides of sulphur and nitrogen in pulsed operation of electrostatic precipitators," *IEEE Transactions on Plasma Science*, vol. 23, no. 4, pp. 661–671, Aug. 1995, ISSN: 0093-3813.

[107] J. J. Lowke, A. V. Phelps, and B. W. Irwin, "Predicted electron transport coefficients and operating characteristics of CO2–n2–he laser mixtures," *Journal of Applied Physics*, vol. 44, no. 10, pp. 4664–4671, Oct. 1, 1973, ISSN: 0021-8979.

[108] S. Pancheshnyi, "Role of electronegative gas admixtures in streamer start, propagation and branching phenomena," *Plasma Sources Science and Technology*, vol. 14, no. 4, p. 645, 2005, ISSN: 0963-0252.

[109] P. Ségur, A. Bourdon, E. Marode, D. Bessieres, and J. H. Paillol, "The use of an improved eddington approximation to facilitate the calculation of photoionization in streamer discharges," *Plasma Sources Science and Technology*, vol. 15, no. 4, p. 648, 2006, ISSN: 0963-0252.

[110] G. V. Naidis, "Dynamics of streamer breakdown of short non-uniform air gaps," *Journal of Physics D: Applied Physics*, vol. 38, no. 21, p. 3889, 2005, ISSN: 0022-3727.

[111] A. Haddad and D. F. Warne, *Advances in High Voltage Engineering*. IET, 2004, 669 pp., ISBN: 978-0-85296-158-2.

[112] T. Kitamura, H. Kojima, N. Hayakawa, K. Kobayashi, T. Kato, and T. Rokunohe, "Influence of space charge by primary and secondary streamers on breakdown mechanism under non-uniform electric field in air," in *2014 IEEE Conference on Electrical Insulation and Dielectric Phenomena (CEIDP)*, Oct. 2014, pp. 122–125.

[113] M. Schueller, A. Blaszczyk, A. Krivda, and J. Smajic, "Influence of the surface conductivity of a single glass barrier on the breakdown voltage in an air insulated rod plane arrangement," in *2016 IEEE Conference on Electrical Insulation and Dielectric Phenomena (CEIDP)*, Oct. 2016, pp. 428–431.

[114] S. Singh, Y. V. Serdyuk, and R. Summer, "Streamer propagation in hybrid gas-solid insulation," in *2015 IEEE Conference on Electrical Insulation and Dielectric Phenomena (CEIDP)*, Oct. 2015, pp. 387–390.

[115] ——, "Streamer branching in air: Physical model and simulations in fully 3d spatial domain," in *Properties and Applications of Dielectric Materials (ICPADM), 2015 IEEE 11th International Conference on the*, Jul. 2015, pp. 220–223.

Chapter 8

Publications

Here follows a short description of the papers that are a part of this thesis. Paper I–IV mainly report experimental results on pre-breakdown and breakdown processes in rod-plane air gaps with (I, III, IV), and without (II) a dielectric barrier. Paper III also includes surface charge measurements, but the majority of these are presented in Paper V. In Paper V and VI, simulation models are used to interpret surface charge measurements. In paper VII, a drift-diffusion model is used to study the dynamics of surface charging by streamers in non-uniform fields.

Paper I: Streamer propagation in rod-plane air gaps with a dielectric barrier

Presented at the IEEE Conference on Electrical Insulation and Dielectric Phenomena (CEIDP), October 2016 in Toronto, Canada

DOI 10.1109/CEIDP.2016.7785515.

Short summary

The first pre-breakdown diagnostics results are presented in this paper. The paper focuses on streamer propagation in a 60 mm positive LI-stressed rod-plane air gap with a dielectric barrier in two different positions. The streamer spatio-temporal development is captured in detail using camera frames of 20 ns exposure time. The streamers propagate around the barrier to ground without causing breakdown.

As the surface is charged in the process, an analysis of the effect of surface charge on streamer inception voltage is included. This analysis demonstrates how the charge distribution on the surface can mitigate inception as it screens the rod. The surface potential of the barrier was set to 86 % of the applied voltage. This was based on the assumption that the surface is charged to the potential of the streamer head, with an assumption of 0.54 kV/mm voltage drop along the streamer. This was, as later experiments have shown (paper V), not realistic surface charging behaviour. It did, however, illustrate the influence of surface charge on streamer inception.

Paper II: Breakdown in short rod-plane air gaps under positive lightning impulse stress

Presented at the Nordic Insulation Symposium (Nord-IS), June 2017, Västerås, Sweden

DOI 10.5324/nordis.v0i25.2377.

Short summary

The discharge diagnostics setup in paper I is extended with a fast current measurement system and PMTs in this paper. Pre-breakdown and breakdown mechanisms of short rod-plane gaps ($\leq 100\,\mathrm{mm}$) without barriers was investigated. The effect of homogeneity and clearance on breakdown mechanisms was studied using two different rod radii (3.5 and 10 mm). The breakdown mechanism was mainly a leader-type discharge.

The breakdown mechanism of shorter gaps (20 mm) was dominated by the heating of primary streamer channels. Only here, a dependency on the rod radius was observed. As the rod with greater radius (10 mm) has a higher streamer inception voltage, the breakdown voltage was also higher. The stability field estimates from eq. (2.7) fit well with the 50 % breakdown voltages. It was argued that eq. (2.7) should be interpreted in light of the leader-type breakdown mechanism.

Different light filters were used on the PMT to characterize the discharges. Although the leader-type channels were more luminous, both streamers and leader-type channels emitted light from the ultra-violet to the infra-red range. It was therefore not possible to distinguish these based on the emitted light ranges only.

Paper III: Surface charging of dielectric barriers under positive lightning impulse stress

Presented at the IEEE Conference on Electrical Insulation and Dielectric Phenomena (CEIDP), October 2017, Fort Worth, USA

DOI 10.1109/CEIDP.2017.8257620.

Short summary

This work contains the initial surface potential measurements at the NTNU HV lab. In addition to the surface potential measurement, the discharge diagnostics setup from paper II was used.

An arrested leader-type channel was observed. The accumulated surface charge on the dielectric barrier was likely responsible for arresting the leader-type channel. Later analysis with VHVlab suggested that the arrested leader-type channel led to charging above saturation charge (see paper V).

Moreover, back discharges were observed with the PMT, camera and current measurement. These were pulses of some 100 kHz on the LI tail. A faint glow on the rod was observed with the camera, and current pulses of ca. 1 mA were observed. The back discharges led to a saddle-shaped rather than a bell-shaped surface potential. It was argued that these discharges continue until the potential between the barrier and rod is smaller than the rod inception voltage. For a more thorough analysis of the effect of these discharges on the surface potential, see paper V.

Paper IV: Breakdown mechanisms of rod-plane air gaps with a dielectric barrier subject to lightning impulse stress

Published in IEEE Transactions on Dielectrics and Electrical Insulation, June 2018, Vol. 25, Issue 3
DOI 10.1109/TDEI.2018.007023

Short summary

In this paper, the discharge diagnostics setup from paper II is used to study both positive and negative breakdown in short rod-plane gaps with a dielectric barrier.

Positive breakdown is characterized by the development of leader-type channel from the rod, which propagates around the barrier toward ground. It was also shown that the current-velocity relationship is leader-like. The negative breakdown involves a system of discharge mechanisms of both polarities. At negative impulse, positive streamers and leaders typically start from the ground plane and propagate around the barrier to the rod.

The barrier increases the 50 % breakdown voltage by increasing the shortest leader path. The increase is around 0.5 kV/mm, coincidentally the same as the streamer stability field E_{st}. At negative impulse, the increase is 0.9 kV/mm, which is in the range of negative streamer stability field strength.

Paper V: Surface charging of dielectric barriers in short rod-plane air gaps – experiments and simulations

Presented at the IEEE International Conference on High Voltage Engineering and Application (ICHVE), September 2018, Athens, Greece
DOI 10.1109/ICHVE.2018.8642108

Short summary

This paper contains the majority of surface charge measurements taken at HSR Rapperswil. The measurements are compared with the saturation charge model in VHVlab. It is concluded that the model predictions fit well for the simple rod-barrier-plane geometry. The model is able to predict secondary phenomena like back discharges and discharges on the ground plane side of the barrier. These were provoked using a small protrusion on the ground plane. Analysing the surface potential measurements with the simulation tool requires an intricate procedure which is described in detail.

It is found that the model under-predicts the surface charge if there is a leader-type discharge. The reason is that the leader can be considered as an extension of the electrode, and should be modeled as such. Moreover, it is found that the surface potential decays and disappears within a few hours.

The results are encouraging for dielectric design applications, as the saturation charge simulations are not computationally heavy.

Paper VI: Surface Charging Formulations for Engineering Applications. Validation by Experiments and Transient Models

Presented as an extended abstract to the 12th International Conference on Scientific Computing in Electrical Engineering, October 2018, Taormina, Sicily, Italy

Short summary

This paper discusses the simulation model in paper V in greater detail. It also includes simulation results from a transient (drift-diffusion) model in COMSOL Multiphysics by Thomas Christen. The simulation models are discussed in light of the experimental results of paper V.

In the transient model, saturation charge (normal electric field at the surface) is observed, when space charge is neglected in Poisson's equation. With space charge, the normal electric field points out of the surface.

Paper VII: Streamer and surface charge dynamics in non-uniform air gaps with a dielectric barrier

To appear in IEEE Transactions on Dielectrics and Electrical Insulation, August 2019, Vol. 26, Issue 4.

Short summary

This paper analyzes the surface charging dynamics in rod-barrier-plane gaps with a drift-diffusion model for computer clusters (PlasmaC). One aim is to understand how the saturation charge simulations fit the experiments in paper V.

2D planar simulations of non-uniform air gaps with a dielectric barrier are presented. The simulated streamer channel produces more than enough charge to charge the surface to saturation during the LI, and saturation is achieved within tens of ns. Similar streamer propagation speeds and ranges as experimental values are also observed. Moreover, the possible effect of photoemission on surface charge accumulation is clarified. Discharge suppression by streamer-deposited surface charge is also demonstrated. Finally, the effect of back discharges on the surface potential distribution is demonstrated qualitatively.

Paper I

presented at the IEEE Conference on Electrical Insulation and Dielectric Phenomena (CEIDP) 2016, Toronto

Streamer Propagation in Rod-Plane Air Gaps with a Dielectric Barrier

Hans Kristian Meyer, Frank Mauseth
Norwegian University of Science and Technology
Dept. of Electric Power Engineering
Trondheim, Norway

Atle Pedersen
SINTEF Energy Research
Trondheim, Norway

Jonas Ekeberg
ABB Ltd.
Baden-Dättwil, Switzerland

***Abstract*—High-voltage design optimization requires a fundamental understanding of electrical breakdown mechanisms under different stress situations. The impulse withstand voltage is normally used as dimensioning criterion for medium voltage air-insulated systems as flashover mechanisms in air are rapid. Prediction of withstand voltage relies on streamer inception and propagation models that are not always sufficiently accurate. Positive impulse voltage experiments were performed on a rod-plane gap with a dielectric barrier at different positions parallel to the ground plane. Streamers initiate from the rod tip and propagate in the field direction. Charge deposited on the dielectric surface changes the field situation and can result in a higher inception voltage. The streamer propagation was recorded with a fast ICCD camera. Finite element method field simulations of the background field were used to evaluate the effect of a barrier surface potential on the streamer inception voltage. Streamers reach the ground electrode without initiating electrical breakdown. The discharge activity from the rod was reduced by deposited charge on the barrier.**

I. Introduction

Space is a limiting factor in high voltage engineering, resulting in an incentive to minimize equipment size. The breakdown strength of the insulating medium restricts designers of gas insulated systems. Sulphur hexafluoride gas (SF_6) is often used as insulating medium because of its good dielectric properties, but alternatives are sought since SF_6 is a very potent greenhouse gas. The withstand voltage of air is roughly a third of the corresponding value for SF_6 and is therefore normally not used when space is limited. Dielectric barriers can, however, significantly improve the breakdown strength of air [1]. The size and position of such barriers must be chosen carefully. For instance, it has been observed that small barriers close to the live electrode can reduce the withstand voltage relative to that of the corresponding barrierless gap [2]. Estimation of the withstand strength of such hybrid gas-solid insulation systems require better knowledge of the interaction between gas discharges and dielectrics. An important aspect is the field distortion that can arise when charge is deposited on dielectric surfaces. This work aims to further explore the characteristics of electrical discharges in an inhomogeneous air gap with a dielectric barrier. Standard positive lightning impulse voltages ($1.2/50\,\mu s$) are used since they are usually dimensioning for gas insulation systems in the medium voltage (MV) range.

II. Breakdown in air

A. Streamer inception

In atmospheric air with gap distances larger than a few mm, the prediction of breakdown is based on the streamer inception criterion

$$\int_\Gamma \alpha_{\text{eff}} dx = \ln(N_c) \tag{1}$$

where $\alpha_{\text{eff}}(E)$ is the field-dependent effective ionization coefficient, and N_c is the critical number of electrons in the electron avalanche needed to create a self-propagating streamer head. For atmospheric air MV applications in strongly inhomogeneous fields, $\ln(N_c) \approx 18.4$ should be used [3]. Finding the correct streamer path Γ is not straightforward in complex geometries. A common approximation is to assume that it starts in the high field region and follows a field line along which $\alpha_{\text{eff}} > 0$. The integration path is typically a few mm and ends when the background field reaches a critical value E_c such that $\alpha_{\text{eff}}(E_c) = 0$. $\alpha_{\text{eff}}(E_c)$ can be estimated with empirically determined fit functions [4]. E_c is the field strength at which the probability of ionization is equal to that of recombination, typically around $2.5\,\mathrm{kV/mm}$ for atmospheric air [3], [5].

B. Streamer propagation

A sufficiently high voltage must be applied if streamers are to reach the ground electrode d mm away. For a strongly inhomogeneous field distribution E in a gap where $5\,\mathrm{cm} < d < 2\,\mathrm{m}$, the prediction of streamer propagation distance is based on the assumption of a constant field strength E_{st} in the streamer channel. The propagation distance d_S is estimated with the equal area rule $E_{st} \cdot d_S \approx \int_0^{d_S} E(x)dx$ along a field line. The impulse voltage level leading to breakdown in air is approximately [3]

$$U_W = U_0 + d \cdot E_{st} \tag{2}$$

where $E_{st} \approx 0.54\,\mathrm{kV/mm}$ is the internal field strength along the positive streamer behind its front. $U_0 \approx 20 - 30$ kV is equivalent to the streamer head potential needed to generate a breakdown [6].

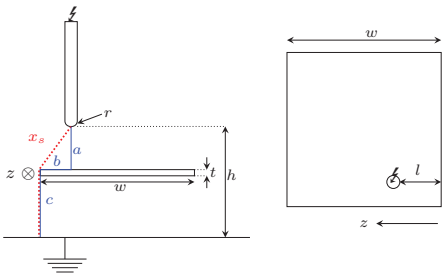

Fig. 1. Rod-plane gap with insulating barrier.

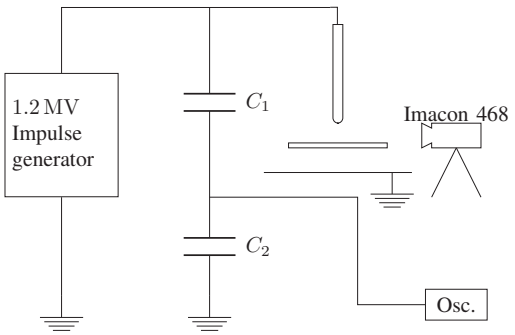

Fig. 2. Experimental set-up.

C. Barrier effect

The withstand voltage of an air gap can be increased by introducing an insulating barrier between the electrodes. This can be understood in terms of an elongated path for air discharges, as a longer distance d in (2) results in a higher withstand voltage U_W. The shortest path to the ground electrode in Fig. 1 is $x_s = \sqrt{a^2 + b^2} + c$, whereas in a barrierless gap the distance would only be $a + c$.

Furthermore, streamers deposit charge on the dielectric surface, reducing the field between the rod and barrier while increasing it between the barrier and ground. With a large and sufficiently charged barrier, the field between its surface and ground will be weakly inhomogeneous. The withstand voltage $U_W(c)$ of the gap between barrier and ground is then governed by streamer inception, not propagation. Assuming that the barrier is charged to a potential equal to that of the streamers reaching the barrier, the impulse level necessary for breakdown becomes [2]

$$U_W = U_W(c) + a \cdot E_{st}. \tag{3}$$

Small barriers close to the electrode can result in poor withstand voltages [2]. This could be caused by high tangential background field strengths that can support streamer propagation along the entire surface or edge effects [2], [7].

III. Experimental

A. Experimental set-up

A $1.2\,\mathrm{MV}$ Marx impulse generator was used to generate lightning voltages over a rod-plane gap with a dielectric barrier, see Fig. 2. An Imacon 468 camera with an 85 mm f/1.8 Nikkor lens in a Faraday cage at a distance of $\sim 1\,\mathrm{m}$ from the live electrode was used to capture the discharge activity. An optical beam splitter in the camera divided incoming light into 8 paths, each with an intensified charge-coupling device (ICCD). The exposure time of each frame is controlled by a digital circuit, giving a minimum possible time resolution of $10\,\mathrm{ns}$. The images were timed to the impulse voltage using a digital delay generator. The applied voltage and camera trigger monitor pulse were measured with an oscilloscope.

B. Experimental procedures

Positive lightning impulses were applied to a rod-plane gap with a $600\,\mathrm{mm} \times 600\,\mathrm{mm} \times 5\,\mathrm{mm}$ polycarbonate barrier over a $1\,\mathrm{m} \times 1\,\mathrm{m}$ ground plane. An electrode with a hemisphere rod-tip radius r = $3.5\,\mathrm{mm}$ was placed centrally above to the ground plane at a height h = $60\,\mathrm{mm}$. To achieve better imaging conditions, the electrode was shifted towards the camera so that l in Fig. 1 was $\sim 170\,\mathrm{mm}$. The overhang b was varied between $40\,\mathrm{mm}$ and $0\,\mathrm{mm}$ by moving the barrier transverse to the camera axis z. The distance a from the barrier surface to the rod tip was kept constant at $20\,\mathrm{mm}$. The ratios w/b and l/b were chosen relatively large to ensure that streamer propagation would occur inside the frame and transverse to the camera axis z.

All sides of the barrier were cleaned with isopropanol between each impulse to remove deposited charge. A handheld electrostatic voltmeter was used to verify that the surface potential was less than $500\,\mathrm{V}$. The temperature, pressure and relative air humidity were logged.

C. Image processing

Calibration pictures with no voltage stress on the gap were taken after each successful streamer image sequence to adjust for differences in the ICCD light sensitivity. This calibration picture sequence was later subtracted from the streamer image sequence, resulting in more uniform background light. As the discharges were very faint, it was also necessary to enhance the image brightness and contrast. These parameters were adjusted to the same values for all images in order to normalise the evaluation of discharge intensity.

D. Simulations

3D electrostatic simulations of the background field were made using COMSOL Multiphysics. Charge deposited was simulated with an electric potential on the barrier surface and side. This potential was approximated using (3) to the potential of streamers that have reached the barrier $U_W - a \cdot E_{st}$. The streamer inception criterion (1) was computed along field lines from the rod tip to ground.

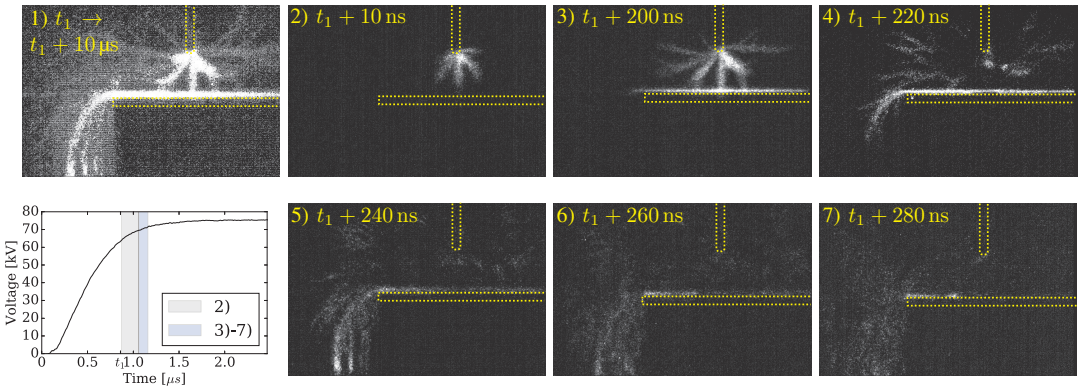

(a) Barrier overhang b = 40 mm with applied lightning impulse voltage U = 75.37 kV. Rel. air humidity 35 %, temp. 22 °C, air pressure 100.8 kPa.

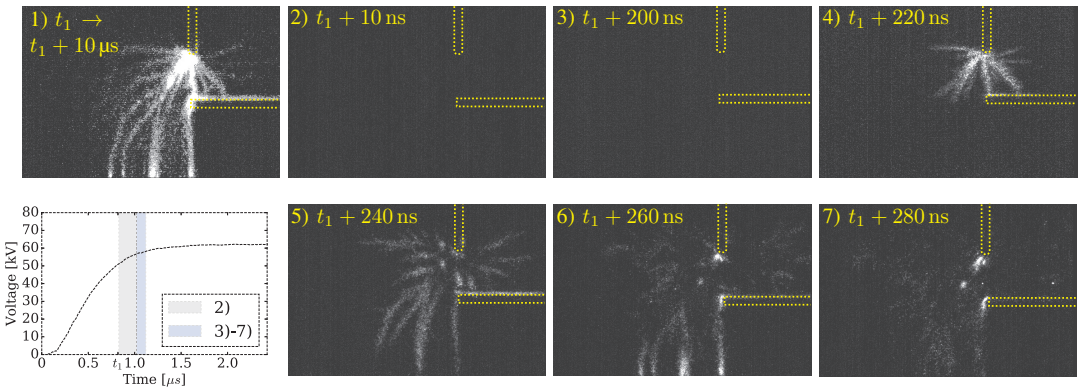

(b) Barrier overhang b = 0 mm with applied lightning impulse voltage U = 62.18 kV. Rel. air humidity 40 %, temp. 21 °C, air pressure 100.2 kPa.

Fig. 3. Streamers in a rod-plane gap with a dielectric barrier. Electrode-to-ground distance h = 60 mm, barrier surface height c = 40 mm and barrier thickness t = 5 mm. Frame 1) with exposure time 10 µs shows the accumulated discharge activity. Frame 2) is 190 ns long while frames 3)-7) are all 20 ns. The frame sequence start time t_1 is indicated in the voltage front plot in the bottom left corner of each figure. No breakdown occurred.

IV. Results and Discussion

A. Images of streamer development

Fig. 3 shows streamer development in a rod plane-gap with two different barrier placements. The geometry is equal in Figs. 3a and 3b except for the overhang b, which is 40 mm in the former and 0 mm in the latter. In Fig. 3a, streamers are incepted at the rod during frame 2). They then propagate along the barrier surface in frame 3) before propagating toward the ground plane in frames 4) and 5). The discharge activity is reduced between the barrier surface and rod in frame 4) and remains sparse in the subsequent frames. This quenching of the discharge activity indicates a counter-field set up by deposited charge on the barrier. Although some streamers reach the ground plane, all the necessary conditions for electrical breakdown are not met.

Similarly, in Fig. 3b, a cloud of streamers touches the barrier in frame 4), before propagating toward ground in frame 5) and 6). Bridging of the gap seems to be faster in Fig. 3b than in Fig. 3a, which is within expectations as the shortest path x_s is 60 mm in the former and ∼85 mm in the latter. Streamer propagation velocity is, based on the development from frame 4) to frame 5) in Fig. 3b, estimated to ∼2 mm/ns.

Edge effects are observed in frames 6) and 7) in Fig. 3b where the discharge activity near the barrier edge is relatively high. Furthermore, discharge activity near the rod is not fully quenched as in Fig. 3a. Frames 1), 6) and 7) in Fig. 3b indicate that the discharge intensity is greater on the barrier-less side.

B. Simulations

The inception voltages in Table I are calculated as described in Sect. III-D. The inception strength is increased by a factor 5 and 2.5 for 40 mm and 0 mm respectively when the barrier is charged. The field lines from the rod tip to ground with and without a barrier potential are shown alongside equipotential

lines in Figs. 4a and 4b respectively. The surface potential is, based on (3), ca. $86\,\%$ of the impulse peak. In reality the potential distribution will be non-uniform and mostly lower than the value used here. The real distribution will reflect the streamer propagation paths in the air and along the surface. Charge density will likely be high directly beneath the electrode and lower further out as the streamer potential decreases with distance from the rod. A better evaluation of the barrier potential influence requires surface charge measurements or simulation models of discharge dynamics. Nevertheless, it is reasonable to expect that charge on the dielectric surface will in these cases alter the field significantly and reduce discharge activity near the rod.

Simulation results by Singh, Serdyuk and Summer [8] of the discharge dynamics for a similar configuration show qualitative similarities to the frames 2)-5) in Fig. 3a and an average streamer propagation velocity of $2\,\mathrm{mm/ns}$.

TABLE I
CALCULATED MINIMUM STREAMER INCEPTION VOLTAGE [kV]

Overhang [mm]	**Uncharged barrier**	**Charged barrier**
40	27.51	139.81
0	28.49	69.19

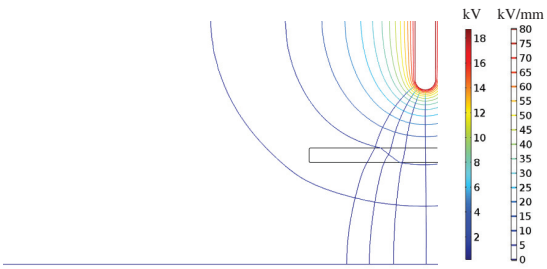

(a)

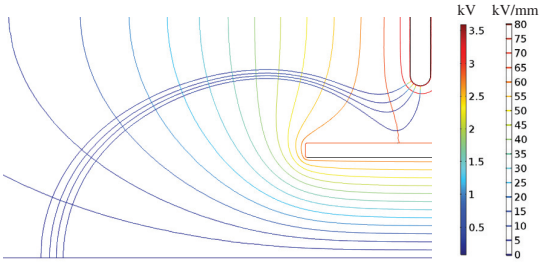

(b)

Fig. 4. Comparison of electrical field and equipotential lines without (a) and with (b) voltage on the barrier surface and edge. Overhang $40\,\mathrm{mm}$.

V. CONCLUSIONS

Streamer propagation in a rod-plane gap with a dielectric barrier under positive lightning impulse stress has been examined with a high-speed camera. Two barrier placements with different overhangs ($40\,\mathrm{mm}$ and $0\,\mathrm{mm}$) were used. In both cases, streamers propagate from the rod to ground without causing electrical breakdown. A reduction in discharge activity near the rod after streamers reach the barrier was observed. Background field calculations demonstrate that the deposited charge on the barrier increases inception strength from the rod, in line with observations.

ACKNOWLEDGMENT

This work is part of the project "Electrical insulation with low-GWP gases" (project number: 245422) funded by the Research Council of Norway and the industrial partners ABB AS, Norway and ABB Ltd., Switzerland.

The authors would also like to thank Dag Linhjell at SINTEF Energy Research, Norway, for all his help with the Imacon camera.

REFERENCES

[1] S. Lebedev, O. Gefle, and Y. Pokholkov, "The barrier effect in dielectrics: the role of interfaces in the breakdown of inhomogeneous dielectrics," *Dielectrics and Electrical Insulation, IEEE Transactions on*, vol. 12, no. 3, pp. 537–555, 2005.

[2] F. Mauseth, J. Jørstad, and A. Pedersen, "Streamer inception and propagation for air insulated rod-plane gaps with barriers," in *Electrical Insulation and Dielectric Phenomena (CEIDP), 2012 Annual Report Conference on*. IEEE, 2012, pp. 739–732.

[3] T. Christen, H. Böhme, A. Pedersen, and A. Blaszczyk, "Streamer line modeling," in *Scientific Computing in Electrical Engineering SCEE 2010*. Springer, 2012, pp. 173–181.

[4] Petcharaks, Komson, "Applicability of the streamer breakdown criterion to inhomogenous gas gaps," Ph.D. dissertation, 1995.

[5] I. Gallimberti, "The mechanism of the long spark formation," in *Journal De Physique, Colloquium C*, vol. 7, 1979, pp. 193–250.

[6] A. Pedersen, T. Christen, A. Blaszczyk, and H. Böhme, "Streamer inception and propagation models for designing air insulated power devices," in *Electrical Insulation and Dielectric Phenomena, 2009. CEIDP'09. IEEE Conference on*. IEEE, 2009, pp. 604–607.

[7] I. Gallimberti, G. Marchesi, and L. Niemeyer, "Streamer corona at an insulator surface," in *7th international symposium on High voltage engineering*, 1991, pp. 26–30.

[8] S. Singh, Y. V. Serdyuk, and R. Summer, "Streamer propagation in hybrid gas-solid insulation," in *2015 IEEE Conference on Electrical Insulation and Dielectric Phenomena (CEIDP)*, Oct. 2015, pp. 387–390.

Paper II

presented at the Nordic Insulation Symposium (Nord-IS)
2017, Västerås

Breakdown in short rod-plane air gaps under positive lightning impulse stress

Hans Kristian Hygen Meyer, Frank Mauseth, Martine Husøy
Norwegian University of Science and Technology

Atle Pedersen
SINTEF Energy Research

Jonas Ekeberg
ABB Switzerland Ltd.

Abstract

Prediction of withstand voltages in air-insulated systems are made on the basis of empirical models that are not sufficiently accurate for complex geometries. Better understanding of the spatiotemporal development of electrical discharges is necessary to improve the present models. Discharges in lightning impulse stressed 20–100 mm rod-plane gaps are examined using a high-speed camera, photo-multiplier tubes (PMTs) and a high-bandwidth current measurement system. The images and measurements of gaps larger than 20 mm show a fast initial streamer discharge with a current rise time of some tens of ns, followed by a dark period of a few µs and a propagation of a slower leader-type channel leading to breakdown. The breakdown mechanisms in the shortest gaps are faster and geometry dependent, probably occuring by heating of initial streamer channels. Different light filters used with the PMTs indicate that all parts of the leader-type discharge development emit light over a spectrum from UV to IR. The initial discharges emit low amounts of warm light and IR compared to the leader-type channel. Finally, it is suggested that empirical breakdown voltage prediction models should be interpreted in light of the leader-type breakdown mechanism.

1. Introduction

SF_6, a very strong greenhouse gas, is often used as insulation in medium voltage (MV) equipment, although insulating gases with lower global warming potential have recently been proposed [1], [2]. Air in combination with dielectrics is a feasible alternative to SF_6 as insulation in MV switchgear [3], [4]. Meeting clearance requirements in air-insulated medium voltage (MV) substations requires accurate withstand voltage prediction models of the dielectric design. Current models often fail to correctly predict the withstand voltage of such hybrid insulation systems. To understand how dielectric surfaces influence the breakdown voltage of an air-insulated gap, the breakdown mechanisms of the gap must be understood. The focus in this work is on positive lightning impulse (LI) stressed short (20–100 mm) inhomogeneous air gaps, applicable to MV switchgear insulation designs. Breakdown in these gaps can happen via a leader-type channel propagating around the space charge left by the initial streamer discharges [5]. The aim of this work is to investigate how this breakdown mechanism fits with standard breakdown voltage prediction models.

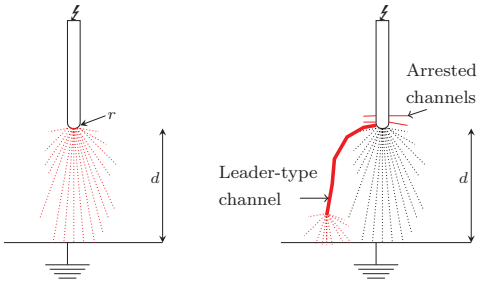

(a) Initial streamers crossing the gap

(b) Leader-type channel development around initial streamers

Fig. 1 – Illustration of discharge development by the leader-type breakdown mechanism in a rod-plane gap with clearance d and a hemispheric rod of radius r.

2. Breakdown in air

2.1. Empirical breakdown models

Although primary streamers crossing the gap is sufficient to induce breakdown in weakly inhomogeneous fields, it is not a sufficient condition for breakdown in strongly inhomogeneous fields. An empirical model of streamer crossing is, however, traditionally used to predict the withstand voltage of strongly inhomogeneous gaps shorter than 1–2 m:

$$U_{\mathrm{W}} = E_{\mathrm{st}} \cdot d + U_0 \tag{1}$$

where the statistical withstand voltage U_{W} is estimated based on an assumption of constant streamer channel field $E_{\mathrm{st}} \approx 0.54\,\mathrm{kV/mm}$ and a streamer head potential $U_0 = 20\text{–}30\,\mathrm{kV}$ needed to cause breakdown [6]. The statistical withstand voltage U_{W} is defined from the 50 % breakdown voltage as $U_{\mathrm{W}} = U_{50\,\%} - 3\sigma$ [7].

Kojima et al. [5] classified positive LI breakdown mechanisms in rod-plane gaps. In their work, two main classes of positive breakdowns are described: channel-heating breakdown and leader-type breakdown. Channel-heating breakdown requires crossing and sufficient heating of a

secondary streamer channel. These conditions can be met in gaps of a few cm if the voltage is high enough. Without a secondary streamer bridging the inter-electrode gap and heating the channel, breakdown will either not occur or it may be induced after the inception and propagation of a leader-type channel. If a leader-type channel develops, it typically starts at a different part of the rod than the primary streamer (Fig. 1) since there will be residual positive space charge from the streamer corona shielding the rod [8], [9].

3. Method

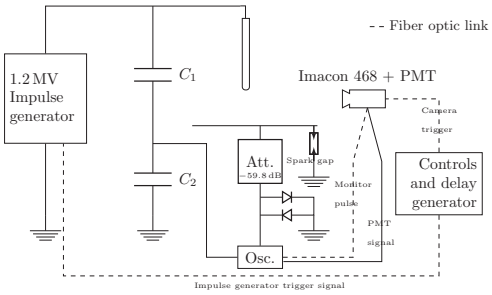

Fig. 2 – Experimental set-up for studying discharge behaviour in 20–100 mm rod-plane gaps. Impulse generator, camera, PMT, current measurement using attenuators (Att.) and current measurement protection (spark gaps and diodes) are shown.

3.1. Camera and PMT

A rod with a hemispheric tip of radius $r = 3.5\,\mathrm{mm}$ or $10\,\mathrm{mm}$ was placed 20–100 mm over a $1 \times 1\,\mathrm{m}$ ground plane and stressed with 1.2/50 µs positive lightning impulses using a 1.2 MV impulse generator. The experiments were performed in ambient air with the temperature, pressure and relative humidity being logged. An Imacon 468 ICCD camera with 7 frames of minimum exposure time 10 ns each was triggered with a delay generator to capture the spatiotemporal discharge development. An 85 mm f/1.4 Nikkor lens was used with the camera which was placed inside a Faraday cage about 1 m away from the rod. A continuous signal of the light intensity was obtained using a PMT 2 m away. Two different PMTs, Philips 56UVP (160–650 nm) and Philips 56TVP (360–850 nm), were used with 2.5 kV supply voltage and different light filters to study the emitted light of the discharges.

3.2. Current measurement system

The current was measured through a 23 m 50 Ω signal cable (RG-214) with approximately 400 MHz bandwidth connected to the ground plane. The signal cable was matched at the oscilloscope end after passing through a series of 13 GHz T-type attenuators with a damping of up to 59.8 dB. To protect the oscilloscope from breakdown currents, a 430 V spark gap was placed close to the ground plane, see Fig. 2. Two diodes were placed in anti-parallel close to the oscilloscope to arrest the fastest voltage transients. The spark gap voltage or attenuation can be modified to measure different current ranges, but a practical upper limit is given by the thermal rating of the first attenuator, 5000 V for 400 ns.

The capacitance between the rod and plane, and between the plane and the supporting structure is in the pF range. With a 50 kV 1.2/50 µs lightning impulse the peak of the capacitive charging current in a 10 pF capacitor is around $I_C = 0.5\,\mathrm{A}$. In addition to high frequency (GHz) noise, a large damped oscillation with frequency 7.5–10 MHz is induced in the current measurement system by the impulse generator as the setup is not placed in a Faraday cage.

3.3. Digital post-processing

The propagation times in the PMT, current and voltage measurement cables were found using a pulse generator. These cable delays and the internal PMT delay were compensated in the digital post-processing of the $5\,\mathrm{GS/s}$ oscilloscope recordings. The correct timing of the camera monitor pulse was found using a PMT and a fast light-emitting diode. A Python script that filters out parts of the current measurement noise was made. The script cuts the 7.5–10 MHz frequencies in the frequency domain to remove noise and subtracts a similarly filtered current measurement without discharge activity in the time domain to remove capacitive current. The original current measurement is also plotted in the results.

As the discharges are faint, the image brightness and contrast were enhanced with photo-editing software. These parameters were adjusted to the same levels in all image series to normalise the evaluation of discharge intensity. Images of background light were subtracted to normalise intensities of the ICCDs.

3.4. Breakdown voltages

The 50 % breakdown and inception voltages of the different rod-plane configurations were estimated using the up and down method with $n = 20$ shots [10].

4. Results

4.1. Breakdown voltage levels

50 % breakdown ($U_{50\,\%}$) and inception ($U_{i,50\,\%}$) voltages for the tested geometries are shown in Fig. 8. 50 % breakdown voltages fit well with the empirical streamer propagation criterion in (1) using $U_0 = 20\,\mathrm{kV}$. The 50 % BD voltages for the strongly inhomogeneous fields seem to be independent of rod geometry, but a discrepancy is

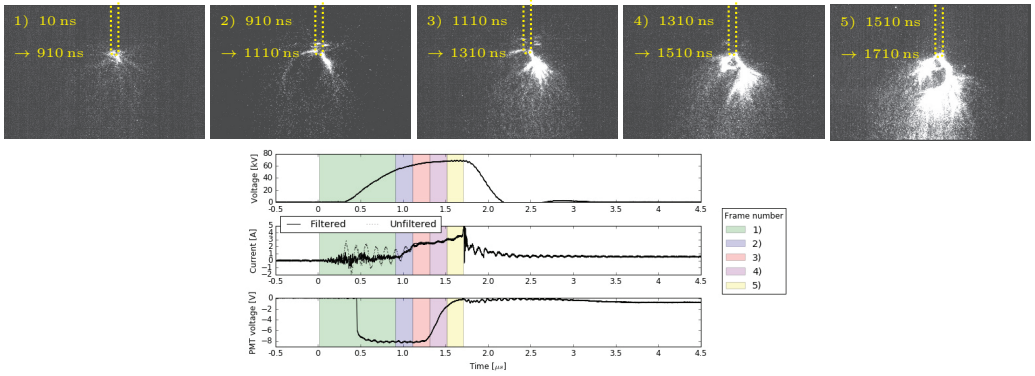

Fig. 3 – Breakdown development images and oscilloscope recordings, $d = 60\,\mathrm{mm}$, $r = 3.5\,\mathrm{mm}$, $U = 69.66\,\mathrm{kV}$. PMT wavelength detection range 160–650 nm. Atmospheric pressure $1.009\,\mathrm{bar}$, $22\,^{\circ}\mathrm{C}$, relative humidity $36\,\%$. Leader-type breakdown channel mechanims.

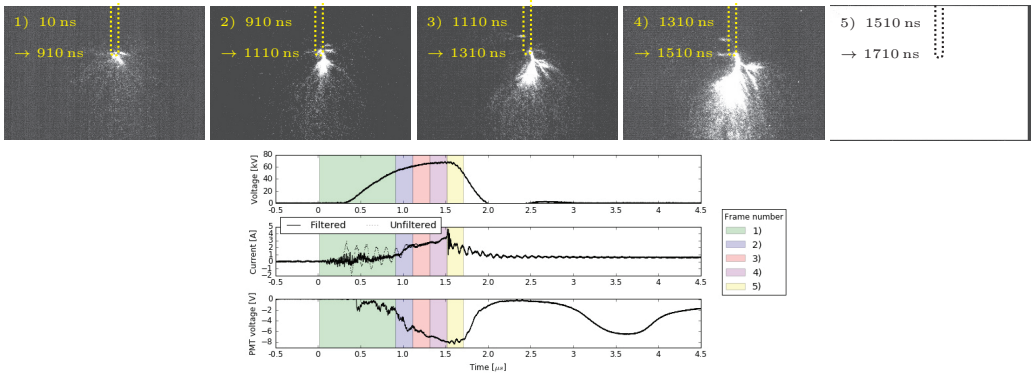

Fig. 4 – Breakdown development images and oscilloscope recordings, $d = 60\,\mathrm{mm}$, $r = 3.5\,\mathrm{mm}$, $U = 68.75\,\mathrm{kV}$. PMT wavelength detection range 610–850 nm. Atmospheric pressure $1.009\,\mathrm{bar}$, $22\,^{\circ}\mathrm{C}$, relative humidity $36\,\%$. Leader-type channel breakdown mechanism.

seen in the shorter gaps (20–40 mm).

4.2. Discharge development

High-speed images of leader-type breakdowns (Fig. 3 to 6) or channel-heating breakdown (Fig. 7) with corresponding voltage, current and PMT signal are shown. All image series have five or six frames of different timing and exposure time showing the discharge development. The positioning of the frames relative to oscilloscope recordings of voltage, current and light are indicated using color-shaded areas in the oscilloscope plots.

Breakdown occurs in all presented image series. Image series without breakdown usually showed the initial streamer activity only (frame 1 in Fig. 3 to 5) or the initial streamers and a leader-type channel stem that was stopped after propagating a few mm in a lateral direction. These arrested channels were sometimes also seen when breakdown occurred as in Fig. 3 and 4 and as illustrated in Fig. 1b.

Two types of PMTs were combined with various filters so that different ranges of wavelengths were detected. Whereas Fig. 3 show the wavelength ranges 160–650 nm and Fig. 4 and 7 shows 610–850 nm, Fig. 5 and 6 show the wavelengths 495–650 nm.

In all image series, the discharge starts with a cloud of streamers crossing the gap as illustrated in Fig. 1a. This discharge activity was captured in a single long frame of 900 ns in all image series, so it is not possible to determine the propagation speed from the images. Previous work by the authors on similar gaps with dielectric barriers showed that these streamers move with roughly $2\,\mathrm{mm/ns}$, crossing the gap in some tens of ns [4].

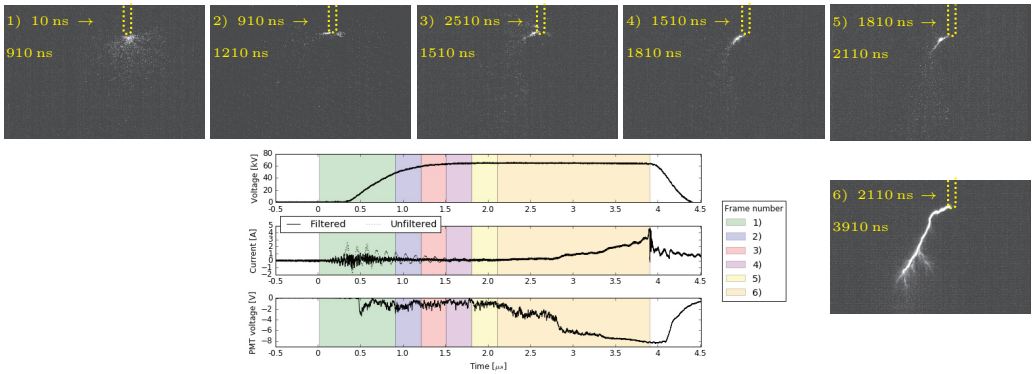

Fig. 5 – Breakdown development images and oscilloscope recordings, $d = 80\,\mathrm{mm}$, $r = 3.5\,\mathrm{mm}$, $U = 65.71\,\mathrm{kV}$. PMT wavelength detection range 495–650 nm. 1.020 bar, 22 °C, relative humidity 37 %. Leader-type channel breakdown mechanism.

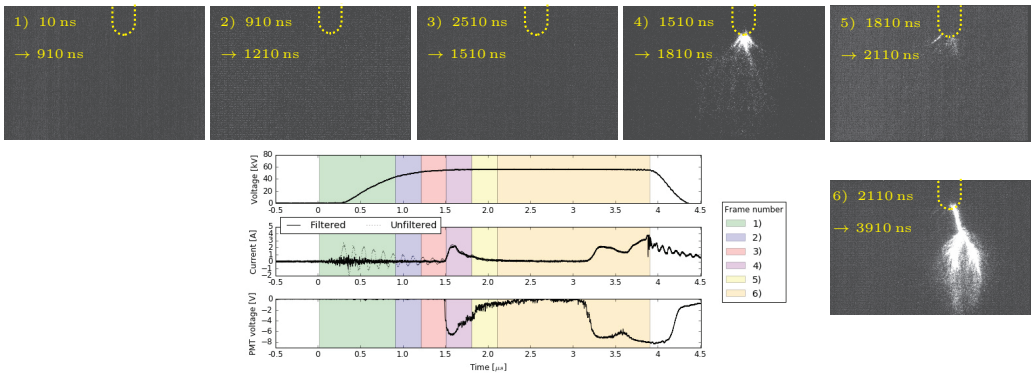

Fig. 6 – Breakdown development images and oscilloscope recordings, $d = 60\,\mathrm{mm}$, $r = 10\,\mathrm{mm}$, $U = 56.58\,\mathrm{kV}$. PMT wavelength detection range 495–650 nm. Atmospheric pressure 1.005 bar, 22 °C, relative humidity 36 %. Leader-type channel breakdown mechanism.

In the configurations where $d = 20\,\mathrm{mm}$, leader-type channels were not observed. Instead, breakdown quickly developed after the initial streamer activity as can be seen in Fig. 7. The light in frames 1–4 is probably from the secondary streamer activity and channel heating, while frame 5 and 6 show the breakdown channel.

For the $10\,\mathrm{mm}$ rod, the streamer current is typically around 2 A, see purple shaded current area in Fig. 6. The rise and fall times of the initial current are estimated from Fig. 6 to $50\,\mathrm{ns}$ and $500\,\mathrm{ns}$ respectively. The integrated charge is around $550\,\mathrm{nC}$. Due to the initial oscillations, the initial streamer current is not visible in the originial current plots in Fig. 3 and 4. From the filtered current measurement it can be seen that the current is typically below $0.5\,\mathrm{A}$. The time from primary streamer inception to breakdown is variable and characterized by a dark period with lower light emission and current before the initiation of the leader-like channel.

After the primary streamer activity, the remaining frames in all figures show an illumination of a single leader-like channel propagating from the rod. The channel starts from different parts of the rod and seems to have a more or less pronounced lateral component in directly after initiation. The lateral propagation is easiest to see when the channel is propagating transverse to the camera axis as in Fig. 5. Several streamers connect the leader-type channel front to the ground plane as illustrated in Fig. 1b. Sometimes multiple or branched channels are observed as seen in Fig. 3 and 4. From frame 3–4 in Fig. 4 it is estimated that the luminous channel moves with a speed of $0.1\,\mathrm{mm/ns}$.

Whereas the initial streamer current seems to be relatively similar for the different geometries, the current induced in the plane during the leader-type channel propagation is varying.

Fig. 3 and 4 indicate that all parts of the discharge emit

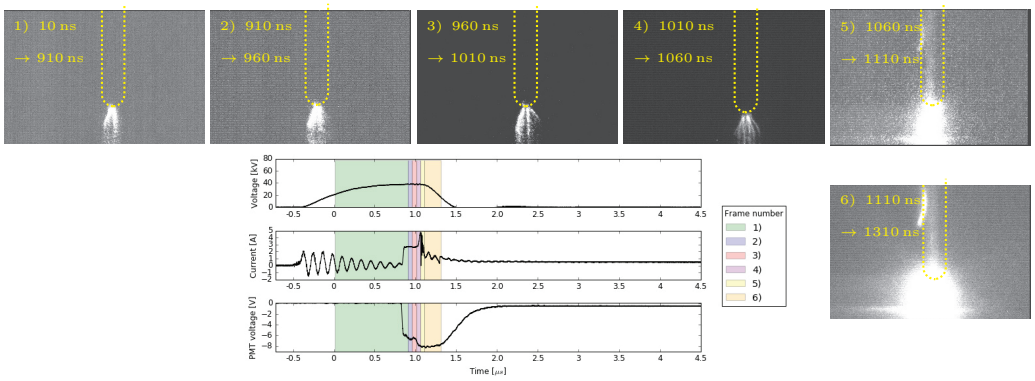

Fig. 7 – Breakdown development images and oscilloscope recordings, $d = 20\,\mathrm{mm}$, $r = 10\,\mathrm{mm}$, $U = 38.76\,\mathrm{kV}$. PMT wavelength detection range 610–850 nm. Atmospheric pressure $0.999\,\mathrm{bar}$, $22\,^{\circ}\mathrm{C}$, relative humidity $35\,\%$. Secondary streamer/channel-heating breakdown mechanism.

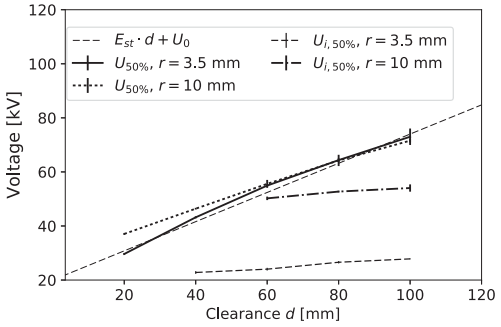

Fig. 8 – $50\,\%$ breakdown $U_{50\,\%}$ voltages with 95% confidence intervals as a function of rod-plane separation d, compared with (1) using $U_0 = 20\,\mathrm{kV}$

light in the wavelength range UV to IR. It was therefore not possible to clearly distinguish different discharge processes based on emitted light ranges only. However, the PMT in Fig. 3 goes directly into saturation with the initial streamers, which is not the case for Fig. 4 and 5. This indicates that the initial streamers emit light mostly in the part of the spectrum below $495\,\mathrm{nm}$, possibly down to UV.

5. Discussion

5.1. Discharge development

The period between primary streamers crossing and leader-type channel inception is sometimes characterized by propagation and crossing of secondary streamers [5], [11]. As the leader-type breakdown mechanism was the only breakdown mechanism seen when $d > 20\,\mathrm{mm}$, it is assumed that a voltage higher than the $50\,\%$ BD voltage is needed in these geometries for secondary streamers to cause breakdown [5].

The initial lateral propagation of the leader-type channel is likely a result of the field distortion from the primary streamer discharges. The variability of the current induced by the leader-type channel could be a result of the stochastic nature of the channel propagation and branching.

The primary streamer current and charge depends on the inception level. The current will therefore be larger in geometries with greater homogeneity as inception levels are higher. As primary streamer discharges seem to emit light mostly at wavelengths below $495\,\mathrm{nm}$, it is assumed that the PMT signal in Fig. 4 during the leader-type channel propagation mainly comes from heating of the channel by the current supplying streamers in front of the channel.

5.2. Breakdown voltage prediction models

As breakdown is not induced by the initial streamers directly, it is possible that (1) should be interpreted as a leader-type channel propagation criterion instead of a streamer propagation criterion. Then the equation would represent the potential needed to launch a leader-type channel across the gap. Once the channel has propagated a few cm into the gap, it is likely to bridge the gap as streamers propagating from its head to ground increase the conductivity of the channel.

The breakdown voltage dependency on the size of the rod for gaps smaller than $40\,\mathrm{mm}$ (see Fig. 8) could be explained by the fact that the channel-heating breakdown mechanism evolves directly from the primary streamer discharges. As the inception voltage for primary streamer discharges increases with homogeneity, so does the breakdown voltage. The leader-type channel mechanism seen in gaps from 40–$100\,\mathrm{mm}$ is on the other hand less dependent on rod geometry. A possible

explanation is that this breakdown mechanism is less related to the initial discharges. This view is supported by the fact that it does not seem to evolve directly from the initial discharges, but rather propagates around them.

6. Conclusions

Breakdown mechanisms in inhomogeneous rod-plane gaps have been studied with a high-speed camera, PMTs and a current measurement system. The breakdown condition for larger gaps (40–$100\,\mathrm{mm}$) is inception of a leader-like channel after the crossing of a cloud of primary streamers. The channel is preceded by primary streamers incepting from the rod tip and propagating to ground. The leader-like channel does not follow the shortest path to ground as it is affected by the electric field distortion due to the space charges created by initial streamers. Similarly to leaders in long ($>1\,\mathrm{m}$) gaps, streamers are propagating from the leader-type channel head to ground.

The breakdown mechanism of the shortest gaps ($20\,\mathrm{mm}$) is governed by heating of initial streamer channels. This breakdown mechanism is dependent on the rod geometry as it evolves directly from the streamer channels. The empirical streamer propagation criterion (1) generally fits well with the $50\,\%$ breakdown voltages for strongly inhomogeneous fields, and the predicted voltage of (1) could represent the potential needed for a leader-type channel to be initiated and propagate across the gap.

Acknowledgement

This work is part of the project ”Electrical insulation with low-GWP gases” (project number: 245422) funded by the Research Council of Norway and the industrial partners ABB AS, Norway and ABB Switzerland Ltd.. The authors would also like to thank Dag Linhjell at SINTEF Energy Research, Norway, for all his help with the experimental set-up.

References

[1] J. Mantilla, N. Gariboldi, S. Grob, and M. Claessens, “Investigation of the insulation performance of a new gas mixture with extremely low GWP,” in *Electrical Insulation Conference (EIC), 2014*, Jun. 2014, pp. 469–473.

[2] Y. Kieffel and F. Biquez, “SF6 alternative development for high voltage switchgears,” in *2015 IEEE Electrical Insulation Conference (EIC)*, Jun. 2015, pp. 379–383.

[3] F. Mauseth, J. S. Jørstad, and A. Pedersen, “Streamer inception and propagation for air insulated rod-plane gaps with barriers,” in *2012 Annual Report Conference on Electrical Insulation and Dielectric Phenomena (CEIDP)*, Oct. 2012, pp. 739–732.

[4] H. K. Meyer, F. Mauseth, A. Pedersen, and J. Ekeberg, “Streamer propagation in rod-plane air gaps with a dielectric barrier,” in *2016 IEEE Conference on Electrical Insulation and Dielectric Phenomena (CEIDP)*, Oct. 2016, pp. 1037–1040.

[5] H. Kojima, K. Hotta, T. Kitamura, N. Hayakawa, A. Otake, K. Kobayashi, T. Kato, T. Rokunohe, and H. Okubo, “Classification of impulse breakdown mechanisms under non-uniform electric field in air,” *IEEE Transactions on Dielectrics and Electrical Insulation*, vol. 23, no. 1, pp. 194–201, Feb. 2016.

[6] A. Pedersen, T. Christen, A. Blaszczyk, and H. Böhme, “Streamer inception and propagation models for designing air insulated power devices,” in *IEEE Conference on Electrical Insulation and Dielectric Phenomena, 2009. CEIDP ’09*, Oct. 2009, pp. 604–607.

[7] J. Kuffel and P. Kuffel, *High Voltage Engineering Fundamentals*. Newnes, Jul. 17, 2000, 556 pp.

[8] T. Kitamura, H. Kojima, N. Hayakawa, K. Kobayashi, T. Kato, and T. Rokunohe, “Influence of space charge by primary and secondary streamers on breakdown mechanism under non-uniform electric field in air,” in *2014 IEEE Conference on Electrical Insulation and Dielectric Phenomena (CEIDP)*, Oct. 2014, pp. 122–125.

[9] I. Gallimberti, “The mechanism of the long spark formation,” in *Journal De Physique, Colloquium C*, vol. 7, 1979, pp. 193–250.

[10] W. J. Dixon and A. M. Mood, “A method for obtaining and analyzing sensitivity data,” *Journal of the American Statistical Association*, vol. 43, no. 241, pp. 109–126, 1948.

[11] R. S. Sigmond, “The residual streamer channel: Return strokes and secondary streamers,” *Journal of Applied Physics*, vol. 56, no. 5, pp. 1355–1370, Sep. 1, 1984.

Paper III

presented at the IEEE Conference on Electrical Insulation and Dielectric Phenomena (CEIDP) 2017, Fort Worth

Surface charging of dielectric barriers under positive lightning impulse stress

Hans Kristian Meyer, Frank Mauseth, Martine Husøy
Norwegian University of Science and Technology
Department of Electric Power Engineering
Trondheim, Norway

Atle Pedersen
SINTEF Energy Research
Trondheim, Norway

***Abstract*—The complex geometry of gas-insulated substations makes it difficult to predict withstand voltages. A key challenge is the characterization of the interaction between electrical discharges and dielectric surfaces. A 60 mm rod-plane air gap with a dielectric barrier is stressed with positive lightning impulse, initiating discharges that are characterized with a PMT, a current measurement system and a high-speed camera. The discharges do not lead to breakdown at the tested voltages. The residual potential on the barrier is measured with a potential probe. Depending on the gap distance, the potential distribution is either bell-shaped or saddle-shaped. The saddle-shape appears when back discharges are seen from the electrode to the barrier. Back discharges reduce the surface charge until the voltage between barrier and rod is lower than the rod inception voltage. Charge density distributions are estimated from the measurements using FEM simulations. In addition to streamer discharges, leader-type channels are sometimes observed. They are arrested close to the dielectric surface. Streamers from these channels charge the dielectric barrier additionally.**

I. Introduction

Dielectric surfaces are common in medium voltage (MV) switchgear insulation systems, as e.g. spacers or shafts or as dielectric barriers. Proper use of gas-solid hybrid insulation techniques could offer the possibility to eliminate the need for the strong greenhouse gas SF_6 as insulating medium in MV switchgear. The increase in withstand strength can be realized by either covering parts of the electrodes [1]–[6] or with inter-electrode barriers [7]–[10]. Such methods require simulation models that model the relevant effects with high accuracy. The dielectric barrier influences the withstand strength by both increasing the shortest discharge path through the gas phase and by altering the field distribution due to surface charge.

The charging of dielectrics during positive lightning impulse (LI) has been studied by several researchers [1], [2], [6], [11]–[14]. Non-contacting field-nullifying probes offer the possibility to measure surface potential without influencing the measurement significantly [15], [16].

Previous work by the authors [9] documented the spatiotemporal propagation of positive streamers in a rod-plane gap with a dielectric barrier. The aim of this work is to further explore the characteristics of electrical discharges in an inhomogeneous air gap with a dielectric barrier. The focus is on the charge accumulation on the barrier surface during positive LI.

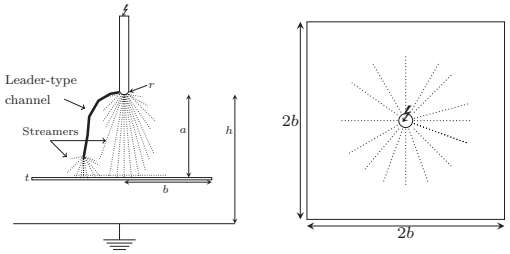

(a) (b)

Fig. 1. Streamers and a leader-type channel in a h mm rod-plane gap reaching a dielectric barrier of thickness t, overhang b, at a distance a mm from the rod, seen from a) the side and b) above

II. Breakdown of air gaps with dielectric barriers

A. Breakdown mechanisms of inhomogeneous air gaps

Strongly inhomogeneous air gaps have inception levels below breakdown levels. Typically, the discharge starts with streamers that can easily cross the gap, leaving behind positive charges that influence the subsequent discharge development [17], [18].

Breakdown can occur after the primary streamer discharges by either channel-heating breakdown or leader-type channel breakdown [18], [19]. Channel-heating breakdown requires crossing and sufficient heating of a secondary streamer channel. These conditions can be met in gaps of a few cm if the voltage is high enough.

B. Streamer-dielectric interaction under impulse voltages

Streamers can propagate from the rod around the barrier to ground without causing breakdown. They propagate along the barrier and charge it (fig. 1), changing the field distribution and the following discharge development [9].

The field from these charges can cause discharges from the rod to the barrier or from the barrier to the rod at the impulse tail. These back discharges will alter the charge distribution on the surface, typically resulting in a saddle-shaped surface potential [20].

The residual charge will also influence the discharge development under following impulses. Charge of the same polarity

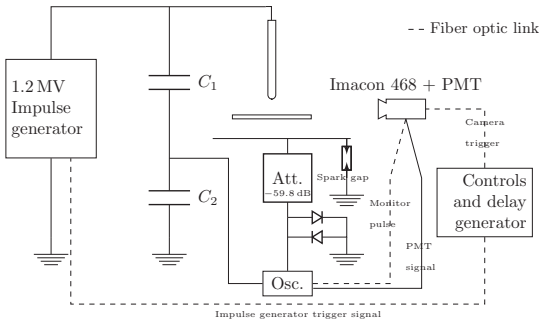

Fig. 2. Experimental set-up for studying discharge behaviour in a $h = 60\,\mathrm{mm}$ rod-plane gap with a dielectric barrier. Impulse generator, camera, PMT, current measurement using attenuators (Att.) and current measurement protection (spark gaps and diodes) are shown.

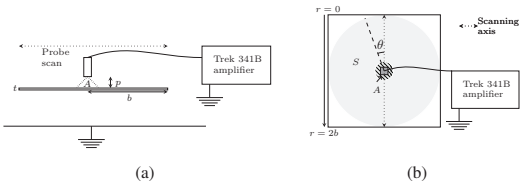

Fig. 3. Charge measurement setup seen from a) the side and b) above. Area A seen by the probe depends on the fixed probe-to-surface distance p. The probe is supplied by a $20\,\mathrm{kV}$ amplifier and is scanned along the $2b = 600\,\mathrm{mm}$ long surface $S = \pi b^2$. The surface charge density distribution is estimated from the measured potential distribution with a FEM 2D axisymmetric model.

as the applied voltage will typically increase inception levels and reduce them for opposite polarity.

III. Method

A. Camera and PMT

A rod-plane gap with a hemispheric aluminium rod tip of radius $r_\mathrm{r} = 3.5\,\mathrm{mm}$ placed $h = 60\,\mathrm{mm}$ over a $1 \times 1\,\mathrm{m}$ ground plane and $a = 0$–$55\,\mathrm{mm}$ over a $600 \times 600 \times 5\,\mathrm{mm}$ polycarbonate barrier was stressed with $1.2/50\,\mu\mathrm{s}$ positive lightning impulses using an $1.2\,\mathrm{MV}$ impulse generator (see fig. 1 and fig. 2). The applied impulse levels $U = 50$–$70\,\mathrm{kV}$ were above streamer inception levels, but below breakdown levels. The experiments were performed in ambient air with the temperature, pressure and relative humidity being logged. An Imacon 468 ICCD camera with 7 frames of minimum exposure time $10\,\mathrm{ns}$ each was triggered with a delay generator to capture the spatiotemporal discharge development. An 85 mm f/1.8 Nikkor lens was used with the camera which was placed inside a Faraday cage about $1\,\mathrm{m}$ away from the rod. A continuous signal of the light intensity was obtained using a PMT about $2\,\mathrm{m}$ away. A Philips 56UVP/TVP PMT with different light filters was used with $2.5\,\mathrm{kV}$ supply voltage.

B. Current measurement system

The current was measured through a $23\,\mathrm{m}$ $50\,\Omega$ signal cable (RG-214) with bandwidth of about $400\,\mathrm{MHz}$ connected to the ground plane. The signal cable was matched at the oscilloscope end after passing through a series of $13\,\mathrm{GHz}$ T-type attenuators with a damping of up to $59.8\,\mathrm{dB}$. To protect the oscilloscope from breakdown currents, a $430\,\mathrm{V}$ spark gap was placed close to the ground plane, see fig. 2. Two diodes were placed in anti-parallel close to the oscilloscope to arrest the fastest voltage transients. The spark gap voltage or attenuation can be modified to measure different current ranges, but a practical upper limit is given by the thermal rating of the first attenuator, $5000\,\mathrm{V}$ for $400\,\mathrm{ns}$.

C. Digital post-processing

The propagation times in the PMT, current and voltage measurement cables were found using a pulse generator. These cable delays and the internal PMT delay were compensated in the digital post-processing of the $5\,\mathrm{GS\,s^{-1}}$ oscilloscope recordings. The correct timing of the camera monitor pulse was found using a PMT and a fast light-emitting diode. A Python script that filters out the current measurement noise and capacitive current was made. The script subtracts a scaled measurement where no discharge activity was seen in the gap by the camera and PMT. The original current measurement is also plotted in the results.

As the discharges are faint, the image brightness and contrast were enhanced with photo-editing software. These parameters were adjusted to the same levels in all image series to normalise the evaluation of discharge intensity. However, the different ICCDs have somewhat different gain. Images of background light were subtracted to normalise intensities of the ICCDs.

D. Charge measurement

A Trek 3455ET probe was used with a $20\,\mathrm{kV}$ Trek 341B high voltage amplifier to measure surface potential $U_\mathrm{S}(r)$, see fig. 3. The probe zeroes the electric field between itself and the surface by adjusting its potential. After the impulse, the rod was removed and the probe was positioned $p = 10\,\mathrm{mm}$ above the barrier surface and scanned along a single axis intersecting the rod position with steps of $\Delta r = 10\,\mathrm{mm}$. The probe was calibrated by placing it over the grounded plane and zeroing it. The barrier was then cleaned with isopropyl alcohol, resulting in a surface potential magnitude below $300\,\mathrm{V}$.

Local potential differences smaller than the surface A seen by the probe are not resolved [21]. If it is assumed that A extends approximately $45°$ from the circular probe aperture with radius $r_\mathrm{p} = 0.76\,\mathrm{mm}$, A is a circle with radius $r_A = 10.76\,\mathrm{mm}$ when the probe spacing is $p = 10\,\mathrm{mm}$. Potential variations over distances smaller than $2r_A \approx 21.5\,\mathrm{mm}$ are therefore not resolved.

E. Estimation of surface charge

Determining the surface charge density distribution $\rho(r, \theta)$ on the surface S (see fig. 3b) from a series of potential

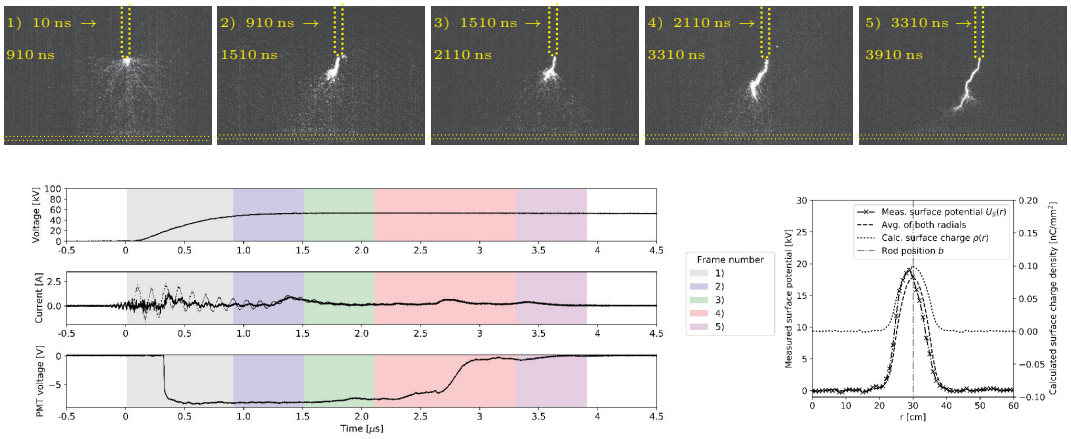

(a) Streamer discharges and leader-type channel development images, oscilloscope recordings and surface potential measurement, $h-a=5\,\mathrm{mm}$, $U=54.3\,\mathrm{kV}$. No breakdown occurred. PMT wavelength detection range 180–610 nm. Atmospheric pressure 1.014 bar, 21 °C, relative humidity 34 %.

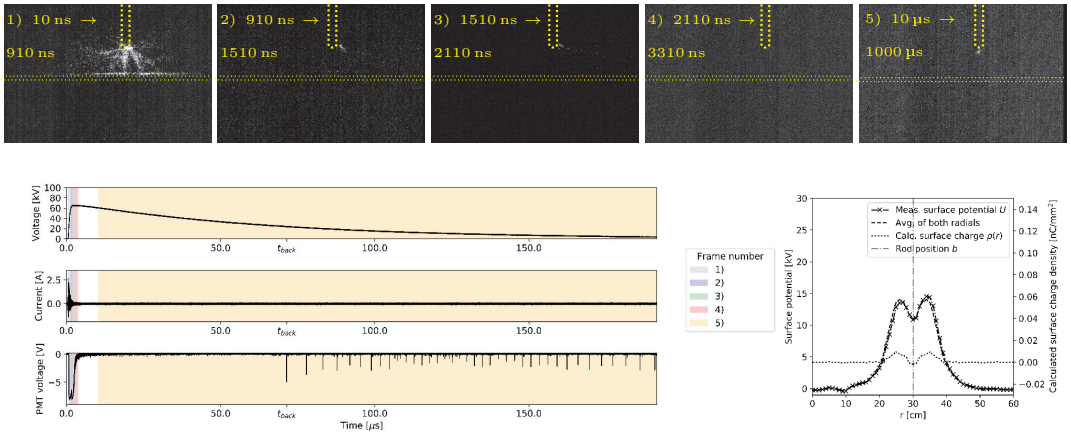

(b) Streamer discharge images, oscilloscope recordings and surface potential measurement, $h-a=40\,\mathrm{mm}$, $U=66.01\,\mathrm{kV}$. No breakdown occurred. PMT wavelength detection range 180–610 nm. Back discharges seen in last frame 5. Atmospheric pressure 1.005 bar, 22 °C, relative humidity 36 %.

Fig. 4. Discharge development and surface potential in $h=60\,\mathrm{mm}$ rod-plane gaps with a $600\times600\times5\,\mathrm{mm}$ dielectric barrier

measurements requires solving an inverse problem [22]. One way to solve it is to apply the measured potential distribution as a boundary condition on the dielectric surface in FEM software [23]. From Gauss' law, $\rho(r,\theta)$ is

$$\rho(r,\theta)=D_{\mathrm{n,gas}}(r,\theta)-D_{\mathrm{n,diel.}}(r,\theta) \tag{1}$$

If the surface charge distribution is assumed to be rotationally symmetric, 2D axisymmetric FEM calculations can be used. In the simulations, $\epsilon_r=3$ for the polycarbonate barrier was used [24]. The average measured potential of the two radials $r=b$ to $r=2b$ and $r=b$ to $r=0$ (fig. 3b) was applied to the barrier. In addition to the surface charge distribution $\rho(r)$, the total charge on the surface $Q_S=\int_S\rho(r)\mathrm{d}S$ was estimated.

Error sources with this method include

1) *Non-symmetrical surface potential distribution*
2) *Resolution/interpolation errors*
3) *Measurement errors* – inaccurate probe stepping and probe-to-surface distance, unparallel probe and surface, and inherent probe errors [15], [16], [25].
4) *Non-zero initial surface potential*

IV. Results

A. Discharge development

Fig. 4a and 4b show discharge development in rod-plane gaps with barriers. Images, oscilloscope plots of voltage, current and PMT, measured surface potential after the discharge and calculated surface charge densities are shown. Color-shaded areas indicate the timing of the camera frames.

1) Leader-type channel: In fig. 4a, a leader-type channel propagates about $75\,\%$ of the gap length after the initial streamers in frame 1. Streamers propagate from the channel head to the barrier as depicted in fig. 1. The leader-type channel is arrested right above the barrier during frame 5.

2) Back discharges: In fig. 4b, the barrier surface is at $h - a = 40\,\mathrm{mm}$. In addition to primary streamer activity (frame 1), back discharges are observed at the impulse tail (frame 6). In the PMT voltage plot, these back discharges can be seen as a series of about 35 pulses spaced 3–6 µs starting at a time t_{back} when the applied voltage is around $U(t_{\text{back}}) = 24\,\mathrm{kV}$, $37\,\%$ of peak voltage U. The interval shortens as the voltage decreases before increasing again from $150\,\mu\mathrm{s}$. The current amplitude is around 1–5 mA, with rise and fall times of some tens of ns. The corresponding image frame 5 shows a faint glow at the rod during this period. Back discharges were not seen for the tested voltages when $h - a < 30\,\mathrm{cm}$.

B. Surface charge

In fig. 4a, the barrier is on the ground plane and the resulting surface potential is bell-shaped with maximum potential $\hat{U}_{\mathrm{S}} = 19\,\mathrm{kV}$, although it is not symmetric around $r = b$. Total calculated charge on the surface is $Q_{\mathrm{S}} = 934\,\mathrm{nC}$. Another experiment at the same voltage level, without leader-type channel inception, resulted in a bell-shaped distribution with $\hat{U}_{\mathrm{S}} = 11\,\mathrm{kV}$ and total charge $Q_{\mathrm{S}} = 682\,\mathrm{nC}$.

In fig. 4b, the surface potential is saddle-shaped, with a larger spread than in fig. 4a and 4b. The calculated surface charge density is also saddle-shaped, and negative right below the rod.

Measurements showed that the surface potential for all geometries was negligibly altered after about $1000\,\mathrm{min}$.

V. Discussion

A. Discharge development

1) Arrested leader-type channel: Leader-type channels typically cause breakdown of rod-plane gaps without barriers when they have propagated a few cm into the gap [18]. The local charging of the dielectric by the streamers at the channel front is likely reducing the field between the channel head and dielectric sufficiently to arrest the channel.

2) Back discharges: The back discharges are similar in frequency to the relaxation pulses observed by Blennow et al. [6] in a plane-parallel dielectric-covered electrode system under positive LI stress. The occurence and frequency of these restoring discharges depend upon the magnitude of surface charge, the insulation system geometry, the time derivative of the applied voltage and the amount of charge neutralized by each back discharge.

B. Surface charge

1) Shape: The higher capacitance of the surface when the barrier is closer to the ground plane leads to a narrower surface potential for similar charge distributions. Charge distributions will likely also be narrower with the barrier on the ground plane due to lower tangential field strengths supporting streamer propagation.

Leader-type channel propagation as in fig. 4a will influence the charge distribution, as streamers propagating from the channel head also charge the dielectric surface. Leader-type channel development therefore results in potential distributions that are greater in magnitude and less symmetric around $r = b$.

2) Condition for back discharges: Back discharges start when the surface charge induced field is high enough [6]. A rod-plane gap with rod radius $3.5\,\mathrm{mm}$ has a streamer onset voltage at positive polarity of around $U_{\text{inc,pos}} = 20\,\mathrm{kV}$ [18]. Assuming a similar inception voltage magnitude for a streamer at negative impulse, the potential drop between the rod and barrier would be $U_{\text{inc,neg}} = -20\,\mathrm{kV}$ at t_{back} in fig. 4b. Since the voltage at the rod is $U(t_{\text{back}}) = 24\,\mathrm{kV}$, the maximum potential on the barrier at t_{back} should be around

$$U_{\mathrm{S},t_{\text{back}}}(b) = U(t_{\text{back}}) - U_{\text{inc,neg}} = 44\,\mathrm{kV} \tag{2}$$

As back discharges in fig. 4b are observed even when the rod potential is approximately 0, it is possible that the surface potential is depleted such that $U_{\mathrm{S}}(b) < 20\,\mathrm{kV}$, in line with measurements.

Back discharges will likely continue until the potential between the barrier and rod is smaller than inception voltage

$$U_{\mathrm{S,after}}(b) < |U_{\text{inc,neg}}| \tag{3}$$

Relation (3) can then be used as a rough estimate of the maximum residual potential below the rod after an impulse.

3) Surface charge density polarity: The surface charge density estimation method (1) results in negative surface charge density at the center when the barrier is closer to the rod, see fig. 4b. Although some charge on the barrier will be neutralized by the back discharges, the surface charge density should not change polarity locally. The local negative surface charge density could be a result of measurement errors.

VI. Conclusions

Surface charging of dielectrics depends upon the discharge mechanisms in play. In this work, a $60\,\mathrm{mm}$ positive LI stressed rod-plane gap with a dielectric barrier has been studied. The discharges were examined with high-speed images, PMTs and current and surface potential measurements. Three discharge phenomenons were observed: primary streamers, leader-type channels and back discharges. Whenever there is discharge activity, it always starts with primary streamers. These lead to a bell-shaped surface potential on the barrier. Leader-type channels develop at voltages closer to breakdown levels. Streamers from the front of these channels charge the surface additionally locally. It is suggested that the field from this charge is responsible for arresting the channel development.

Back discharges are observed at the impulse tail as regular pulses of 100–300 kHz. They are seen when the barrier is closer to the rod, as the reversed field becomes stronger. Back discharges will neutralize surface charge until the voltage drop between barrier and rod is lower than the rod inception voltage. As this voltage is approximately constant for a given rod radius, maximum surface potential after an impulse is restricted by the rod geometry.

ACKNOWLEDGMENT

This work is part of the project "Electrical insulation with low-GWP gases" (project number: 245422) funded by the Research Council of Norway and the industrial partners ABB AS, Norway and ABB Switzerland Ltd.. The authors would also like to thank Dag Linhjell at SINTEF Energy Research, Norway, for all his help with the experimental set-up.

REFERENCES

[1] F. Mauseth, A. Nysveen, and E. Ildstad, "Charging of dielectric barriers in rod-plane gaps," in *Proceedings of the 2004 IEEE International Conference on Solid Dielectrics, 2004. ICSD 2004*, vol. 1, Jul. 2004, pp. 447–451 Vol.1.

[2] S. Kumara, Y. Serdyuk, and S. Gubanski, "Charging of Polymeric Surfaces by Positive Impulse Corona," *IEEE Transactions on Dielectrics and Electrical Insulation*, vol. 16, no. 3, pp. 726–733, Jun. 2009.

[3] M. Sjöberg, Y. V. Serdyuk, S. M. Gubanski, and M. . S. Leijon, "Experimental study and numerical modelling of a dielectric barrier discharge in hybrid air–dielectric insulation," *Journal of Electrostatics*, vol. 59, no. 2, pp. 87–113, Sep. 2003.

[4] D. Durocher, M. Haim, L. Connor, and J. de Jong, "Safety by design: Solid insulated technologies challenge the use of SF6 in medium-voltage switchgear," in *Electrical Safety Workshop (ESW), 2015 IEEE IAS*, Jan. 2015, pp. 1–9.

[5] H. J. M. Blennow, M. L. A. Sjoberg, M. A. S. Leijon, and S. M. Gubanski, "Electric field reduction due to charge accumulation in a dielectric-covered electrode system," *IEEE Transactions on Dielectrics and Electrical Insulation*, vol. 7, no. 3, pp. 340–345, Jun. 2000.

[6] H. J. M. Blennow, M. . S. Leijon, and S. M. Gubanski, "Active high voltage insulation," *Journal of Electrostatics*, vol. 55, no. 2, pp. 159–172, Jun. 2002.

[7] S. M. Lebedev, O. S. Gefle, and Y. P. Pokholkov, "The barrier effect in dielectrics: the role of interfaces in the breakdown of inhomogeneous dielectrics," *IEEE Transactions on Dielectrics and Electrical Insulation*, vol. 12, no. 3, pp. 537–555, Jun. 2005.

[8] F. Mauseth, J. S. Jørstad, and A. Pedersen, "Streamer inception and propagation for air insulated rod-plane gaps with barriers," in *2012 Annual Report Conference on Electrical Insulation and Dielectric Phenomena (CEIDP)*, Oct. 2012, pp. 739–732.

[9] H. K. Meyer, F. Mauseth, A. Pedersen, and J. Ekeberg, "Streamer propagation in rod-plane air gaps with a dielectric barrier," Oct. 2016, pp. 1037–1040.

[10] Y. Chen, Y. Zheng, and X. Miao, "AC breakdown characteristics of air insulated point-plane gaps with polycarbonate barriers," in *2016 IEEE International Conference on High Voltage Engineering and Application (ICHVE)*, Sep. 2016, pp. 1–4.

[11] A. Kumada, S. Okabe, and K. Hidaka, "Residual charge distribution of positive surface streamer," *Journal of Physics D: Applied Physics*, vol. 42, no. 9, p. 095209, 2009.

[12] D. Faircloth and N. Allen, "High resolution measurements of surface charge densities on insulator surfaces," *IEEE Transactions on Dielectrics and Electrical Insulation*, vol. 10, no. 2, pp. 285–290, Apr. 2003.

[13] J. Deng, S. Matsuoka, A. Kumada, and K. Hidaka, "The influence of residual charge on surface discharge propagation," *Journal of Physics D: Applied Physics*, vol. 43, no. 49, p. 495203, 2010.

[14] I. Gallimberti, G. Marchesi, and L. Niemeyer, "Streamer corona at an insulator surface," in *7th international symposium on High voltage engineering*, 1991, pp. 26–30.

[15] M. Schueller, R. Gremaud, and C. Franck, "Accuracy of surface potential measurements of HVDC spacers," in *2014 International Conference on High Voltage Engineering and Application (ICHVE)*, Sep. 2014, pp. 1–4.

[16] A. Winter and J. Kindersberger, "Stationary resistive field distribution along epoxy resin insulators in air under DC voltage," *IEEE Transactions on Dielectrics and Electrical Insulation*, vol. 19, no. 5, pp. 1732–1739, Oct. 2012.

[17] T. Kitamura, H. Kojima, N. Hayakawa, K. Kobayashi, T. Kato, and T. Rokunohe, "Influence of space charge by primary and secondary streamers on breakdown mechanism under non-uniform electric field in air," in *2014 IEEE Conference on Electrical Insulation and Dielectric Phenomena (CEIDP)*, Oct. 2014, pp. 122–125.

[18] H. K. H. Meyer, F. Mauseth, A. Pedersen, M. Husøy, and J. Ekeberg, "Breakdown in short rod-plane air gaps under positive lightning impulse stress," in *Nordic Insulation Symposium (Nord-IS)*, 2017.

[19] H. Kojima, K. Hotta, T. Kitamura, N. Hayakawa, A. Otake, K. Kobayashi, T. Kato, T. Rokunohe, and H. Okubo, "Classification of impulse breakdown mechanisms under non-uniform electric field in air," *IEEE Transactions on Dielectrics and Electrical Insulation*, vol. 23, no. 1, pp. 194–201, Feb. 2016.

[20] S. Kumara, "Electrical Charges on Polymeric Insulator Surfaces and their Impact on Flashover Performance," Doctoral thesis, Chalmers University of Technology, 2012.

[21] M. A. Noras, "Non-contact surface charge/voltage measurements: capacitive probe—principle of operation," *Trek Application Note*, no. 3001, pp. 1–8, 2002.

[22] S. Okabe and A. Kumada, "Measurement Methods of Accumulated Electric Charges on Spacer in Gas Insulated Switchgear," *IEEE Transactions on Power Delivery*, vol. 22, no. 3, pp. 1547–1556, Jul. 2007.

[23] J. Kindersberger and C. Lederle, "Surface charge decay on insulators in air and sulfurhexafluorid - part I: simulation," *IEEE Transactions on Dielectrics and Electrical Insulation*, vol. 15, no. 4, pp. 941–948, Aug. 2008.

[24] J. E. Mark, *Polymer data handbook*. Oxford University Press, 2009.

[25] M. Noras and A. Pandey, "Evaluation of Surface Charge Density with Electrostatic Voltmeter - Measurement Geometry Considerations," in *IEEE Industry Applications Society Annual Meeting, 2008. IAS '08*, Oct. 2008, pp. 1–6.

Paper IV

published in IEEE Transactions on Dielectrics and Electrical Insulation, June 2018

Breakdown mechanisms of rod-plane air gaps with a dielectric barrier subject to lightning impulse stress

Hans Kristian Meyer, Frank Mauseth
Norwegian University of Science and Technology (NTNU)
Department of Electric Power Engineering
Trondheim, Norway

Atle Pedersen
SINTEF Energy Research
Trondheim, Norway

and **Jonas Ekeberg**
ABB Ltd.
Baden-Dättwil, Switzerland

ABSTRACT

The complexity of gas-insulated substations makes it difficult to predict withstand voltages. Modeling interaction between dielectric surfaces and electrical discharges is a key challenge. In this study, 60 mm rod-plane air gaps with a dielectric barrier 20 mm below the rod are stressed with lightning impulses of both polarities. The discharge mechanisms are investigated with a high-speed camera, a photomultiplier tube and a current measurement system. The discharge development and current-velocity relationship is leader-like. With positive polarity applied, a leader propagates from the upper parts of the rod to ground. Negative impulses are characterized by positive leader development from the ground plane to the rod. For both polarities, the discharge starts with streamers propagating from the rod to the barrier. Positive streamers typically reach the opposite electrode without causing breakdown directly. The findings imply that empirical breakdown prediction models for short air gaps should involve conditions for positive leader initiation and development. The results also show that dielectric barriers increase the breakdown voltage by impeding leader development. The barriers increase the shortest discharge path and shift the point of leader inception further up on the rod.

Index Terms — **dielectric barrier, streamers, leaders, propagation, lightning impulse, rod-plane gap, medium voltage, switchgear insulation**

1 INTRODUCTION

Expected restrictions on the use of sulphur hexafluoride (SF_6) gas in medium voltage (MV) switchgear has triggered research efforts to develop environmentally friendly insulation techniques. SF_6 has a 100-year global warming potential (GWP) of roughly 23900 [1]. Using air as insulation has obvious advantages, but it poses dielectric challenges as the equipment must be compact to meet standardized requirements. The field strengths required to initiate discharges are roughly three times lower in air than in SF_6 [2]. Up to three times greater electrode clearances are therefore needed in air than in SF_6 for similar geometries. Accurate withstand voltage prediction models are therefore needed to optimize the dielectric design. This requires a solid understanding of the physical processes leading to breakdown. These processes are complex and difficult to model accurately, so empirical models are typically used [3], [4]. The models can, however, lead to inaccurate results when the insulation system includes dielectric surfaces. Such surfaces are common in switchgear insulation in the form of shafts, spacers or dielectric barriers. Dielectric barriers can significantly improve the withstand voltage of an air gap [5]–[7], and could therefore be used to design space efficient insulation systems with low environmental impact. The aim of this work is to investigate the influence of dielectric barriers on breakdown development in short air-insulated rod-plane gaps. 1.2/50 µs lightning impulses (LI) are used as they are dimensioning in typical MV switchgear type tests [8].

Manuscript received on 11 September 2017, in final form 1 February 2018, accepted 2 February 2018. Corresponding author: H.K. Hygen.

2 BREAKDOWN OF INHOMOGENEOUS AIR GAPS

2.1 STREAMER INCEPTION

The discharge process of inhomogeneous air gaps begins with an electron avalanche of critical size. The space charge left by the avalanche turns into a filamentary discharge, a *streamer*. One dielectric design strategy is to avoid field strengths capable of initiating streamers. To calculate these field strengths, the streamer inception integral

$$\int_{\Gamma} \alpha\,(E(x))\mathrm{d}x \geq \ln N \tag{1}$$

is used. The field-dependent effective ionization coefficient $\alpha(E(x))$ can be estimated with empirical fit functions [2]. The integral is typically evaluated along a critical field line Γ, where $\alpha > 0$, until a critical background field E_{cr} where $\alpha(E_{\mathrm{cr}}) = 0$ is reached. $E_{\mathrm{cr}} = 2.5\ \mathrm{kV/mm}$ for atmospheric air [9]. Inception occurs when the critical number of electrons exceeds $N = 10^8$ [10]. A design approach based on avoiding inception can, however, be overly cautious as inception does not necessarily lead to breakdown.

2.2 STREAMER PROPAGATION

Streamers require a non-zero background field strength to propagate as they dissipate some energy in the process. Another design approach is therefore to allow inception, but inhibit propagation. Positive withstand voltage $U_{\mathrm{W}} = U_{50\%} - 3\sigma$ [10] of inhomogeneous gaps increases linearly with shortest discharge path $\mathrm{x_S}$ [3]:

$$U_{\mathrm{W}} = U_0 + E_{\mathrm{st}} x_{\mathrm{S}} \tag{2}$$

where the constant $E_{\mathrm{st}} = 0.5$–0.54 kV/mm can be interpreted as the internal streamer channel field. E_{st} therefore represents the minimum background field required for stable streamer propagation. $U_0 =$ 20–30 kV can be viewed as the excess potential needed to cause breakdown after the streamers have bridged the gap [3].

Propagation of streamers has been explored with fluid simulations, e.g. [11]–[14]. The large computational burden of such models have, however, limited their application so far, especially for 3D.

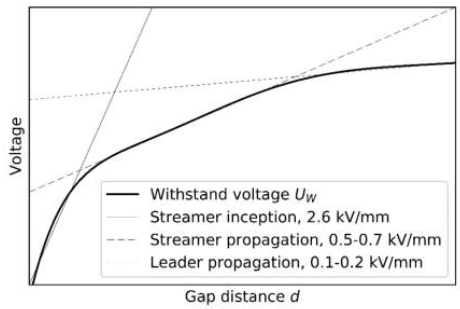

Figure 1. Typical relation between breakdown voltage and gap distance in inhomogeneous fields with fixed radius of curvature [3].

2.3 LEADERS/LEADER-TYPE CHANNELS

Crossing of streamer discharges is not a sufficient condition for breakdown in short rod-plane gaps. Secondary streamer channel heating or "leader-type channels" are needed [15]. Leader-type channels resemble *leaders*, but leaders are traditionally considered to occur in gaps >0.5–1m only [10], [16], [17]. For such large gaps, breakdown voltage typically increases with 0.1–0.2 kV/mm as illustrated in Figure 1. 1.2/50 µs impulse overvoltages are considered too short to support leader breakdown for long gaps due to the slow leader propagation speed (0.02 mm/ns) [16]. A positive leader breakdown typically happens in the following way [17], [18]

1. Primary streamers occur, leaving residual space charges that distort the field distribution
2. Dark period without discharge activity
3. Inception of stems/secondary streamers at the anode
4. Joule heating of stems, leading to temperatures exceeding 1500 K, reduction of gas density
5. Detachment of negative ions due to higher gas temperature. This increases the stem conductivity and field strength at its tip
6. Development of streamers at the stem (leader) front, due to the high field at the leader tip
7. Leader propagation into the gap as Joule heating extends the channel
8. Leader reaching counter-electrode, with subsequent arc

High-speed images of leader-type channels indicate that the above list could apply to leader-type channels as well [15], [19]. The two terms are therefore used interchangeably in the following.

The leader velocity v_{L} depends on the ionization activity at its front, and is typically proportional to leader channel current I_{L} [17], [18]:

$$v_{\mathrm{L}} = \frac{1}{q} I_{\mathrm{L}} \tag{3}$$

where $q =$ 20–50 µC/m represents the average charge necessary for a unit length advancement of the leader channel. The ionization activity depends on the field strength at the channel front, E_{F}, which in turn depends on the applied voltage U and the leader channel field E_{L}. E_{L} decreases with leader length in the range $E_{\mathrm{L}} = 0.5$–0.1 kV/mm, but the reduced field $E_{\mathrm{L}}/n_{\mathrm{n}}$ is constant due to channel expansion and decreasing gas density n_{n}.

2.4 NEGATIVE BREAKDOWN

Less is known about negative lightning impulse breakdown in air. This is partly because positive breakdown occurs at lower voltage magnitudes, and is therefore more critical in high voltage applications. Negative breakdown voltage is higher than positive as negative streamers have less effective propagation mechanisms, and require a higher background field E_{st} =1–1.15 kV/mm [10].

Negative breakdown of longer gaps is known to often involve a system of streamers and leaders of both polarities after the dark period [20]. Typically, the negative leader propagation is driven by *space stems*, bright spots from which streamers of both polarities propagate. A dense network of streamers

Table 1. Rod-plane gap with a dielectric barrier, parameters.

	Parameter	Used
Electrical	Voltage shape	1.2/50 µs LI
	Voltage magnitude U	50-120 kV
	Polarity	Both
	Barrier initial charge	Cleaned (<300 V)
Ambient	Gas mixture	Ambient air
	Temperature (*logged*)	20-24 ºC
	Pressure (*logged*)	0.997 to 1.020 bar
	Rel. humidity (*logged*)	33 to 44 %
	Background radiation	Cosmic
Geometrical	Rod height d	60 mm
	Rod shape	Hemispheric
	Rod radius r	3.5 mm
	Barrier height $d - a$	40 mm
	Barrier overhang b	0-80 mm
	Barrier shape	Square 600x600x5 mm
Material	Barrier material	Polycarbonate (Lexan)
	ϵ_r @ 50 Hz	2.96 [21]
	Surface cond. σ_s	$< 10^{-17}\ \Omega^{-1}\text{cm}^{-1}$ [21]
	Bulk cond. σ_B	$< 10^{-17}\ \Omega^{-1}\text{cm}^{-1}$ [21]
	Barrier roughness	Unknown
	Electrode material	Aluminum
	Electrode roughness	Unknown

connects the negative leader and stem. These stems can sometimes become leaders, which then approach the main leader with increasing velocity.

2.5 ROD-PLANE GAPS WITH DIELECTRIC BARRIERS

Rod-plane gaps are often used to study effects of field inhomogeneity. While being polarity dependent, it is a simple arrangement, which facilitates analysis and validation of breakdown models. However, there are many parameters involved. As can be seen in Table 1, adding a dielectric barrier introduces at least five new parameters and a history effect if the barrier is not completely discharged between impulses.

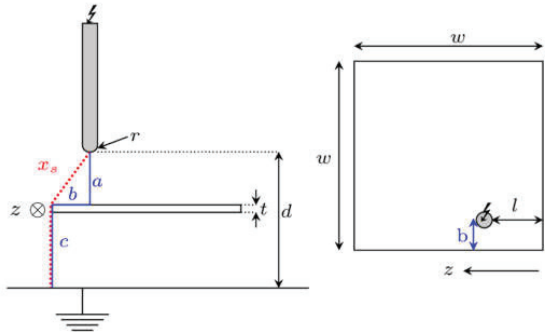

Figure 2. Rod-plane gap with insulating barrier seen from the side and from above. The ratios w/b and l/b were chosen relatively large to ensure that streamer and leader propagation would occur inside the frame and transverse to the camera axis z.

With dielectric barriers in the discharge path, streamers typically propagate along and around the barrier to ground [11], [22]. Barriers can also inhibit secondary streamer development [23], cause leaders to propagate a longer path in the gas phase [24] or stop them [25].

Charges on the barrier will alter the field distribution as shown in Figure 3, with different implications depending on applied voltage and dielectric barrier charge polarity. In Figures 3a and 3b, the rod tip is shielded and the field stress is shifted to the barrier-plane gap. These situations typically occur under DC or during an impulse right after the barrier has been charged by initial streamers. In Figures 3c and 3d, the stress is highest in the rod-barrier gap. These situations can occur during AC or at the declining impulse tail, when the field between the rod and residual charge on the barrier becomes reversed. Reverse discharges from the rod can neutralize charge on the barrier surface in these cases [25].

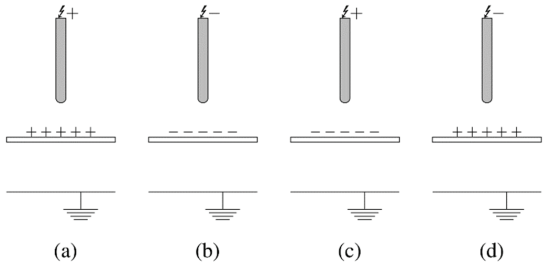

Figure 3. Applied rod voltage and dielectric barrier charge polarity configurations. a) and b) rod voltage same as dielectric barrier charge polarity. c) and d) different polarity between rod and barrier.

3 EXPERIMENTAL

3.1 CAMERA AND PMT

A rod-plane gap with a hemispheric rod tip of radius $r = 3.5$ mm placed 60 mm over a 1x1 m ground plane and 20 mm over a polycarbonate (Lexan) barrier was stressed with 1.2/50 µs lightning impulses using a 1.2 MV impulse generator, see Figure 4. The experiments were performed in ambient air with the temperature, pressure and relative humidity being logged. The barrier was cleaned with isopropyl alcohol between impulses to remove charge. An electrostatic voltmeter was used to verify that this procedure results in a surface potential below 500 V.

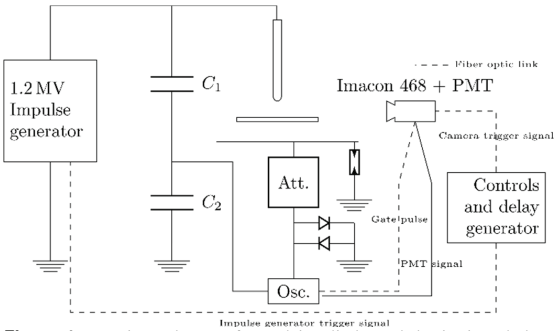

Figure 4. Experimental set-up for studying discharge behavior in rod-plane gaps. Impulse generator, camera, PMT, current measurement using attenuators (Att.) and current measurement protection (spark gaps and diodes) are shown.

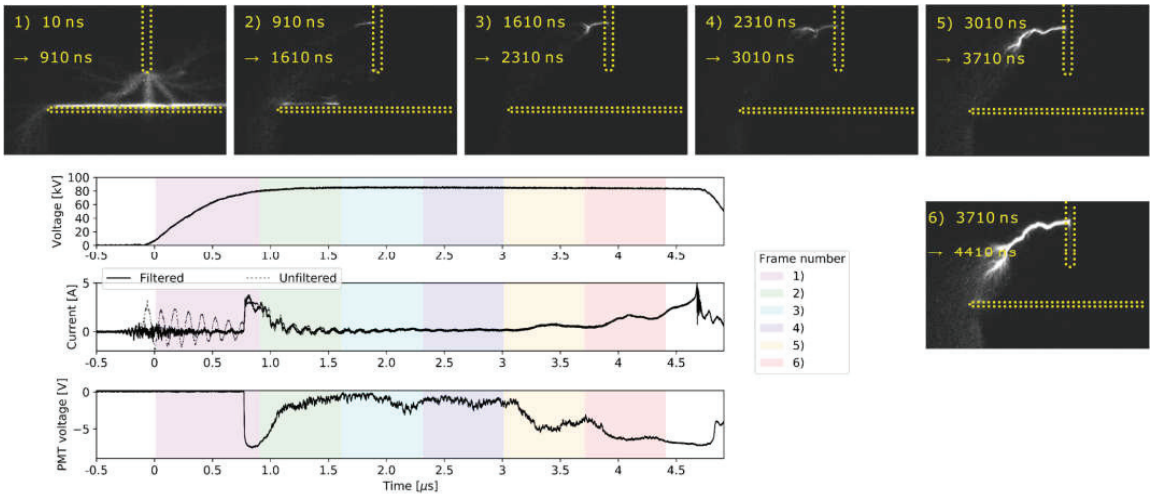

Figure 5. $d = 60$ mm rod-plane gap with barrier at $c = 40$ mm with $b = 60$ mm overhang (see Figure 2), 1.2/50µs LI 86 kV applied. PMT wavelength detection range 495-850 nm.

An Imacon 468 ICCD camera with 7 frames of 10 ns minimum exposure time each was triggered with a delay generator to capture the spatiotemporal discharge development. An 85 mm f/1.8 Nikkor lens was used with the camera which was placed inside a Faraday cage about 1 m away from the rod. A continuous signal of the light intensity was obtained using a PMT about 2 m away. A Philips 56AVP/TVP PMT was used with 2.5 kV supply voltage. A low-pass filter blocking light with wavelength < 495 nm and a paper-layer filter were used in the experimental work to limit PMT saturation. The PMT filter type used is indicated in the figure texts.

3.2 CURRENT MEASUREMENT SYSTEM

The current was measured through a signal cable (RG-214) with bandwidth of about 400 MHz connected to the ground plane. The signal cable was matched at the oscilloscope end after passing through a series of 13 GHz T-type attenuators with a damping of up to 59.8 dB. To protect the oscilloscope from breakdown currents, a 430 V spark gap was placed close to the ground plane, see Figure 4. Two diodes were placed in anti-parallel close to the oscilloscope to arrest the fastest voltage transients. The spark gap voltage or attenuation can be modified to measure different current ranges, but a practical upper limit is given by the thermal rating of the first attenuator, 5000 V for 400 ns.

3.3 DIGITAL POST-PROCESSING

The propagation times in the PMT, current and voltage measurement cables were found using a pulse generator. These cable delays and the internal PMT delay were compensated in the digital post-processing of the oscilloscope recordings. The correct timing of the camera monitor pulse was found using a PMT and a fast light-emitting diode. A Python script that filters out the current measurement noise and capacitive current was made. The script subtracts a scaled measurement where no discharge activity was seen in the gap on the camera or PMT. The original current measurement is also plotted in the results. The same script also integrates the current measurement during each frame to evaluate the validity of equation (3).

As the discharges are faint, the image brightness and contrast were enhanced with photo-editing software. These parameters were adjusted to the same levels in all image series to normalize the evaluation of discharge intensity. Images of background light were subtracted to normalize the intensities of the ICCDs.

3.4 BREAKDOWN VOLTAGES

The 50 % breakdown voltages of the different configurations were estimated using the “up-and-down” method [10] with n = 20 shots and steps of 0.5 kV. The results were corrected for pressure, temperature and humidity according to [8].

In addition to the experiments with dielectric barriers, breakdown voltages of 60-120 mm rod-plane gaps without barriers were found.

4 RESULTS

4.1 ROD-PLANE GAP WITH BARRIER UNDER POSITIVE LI

Figure 5 shows a typical positive breakdown. In frame 1, positive streamers propagate from the rod to ground, without causing breakdown. These streamers move around the barrier with ca. 2 mm/ns [22]. After the streamer propagation and crossing, a leader channel stem appears about 25 mm over the rod tip stretching horizontally out from the rod. The channel heats up sufficiently to become a leader discharge, moving in a tortuous and branched path around the barrier toward the grounded electrode. Streamers connect the leader channel tip to the ground plane, supporting a current of around 0.25–1.5 A (Figure 7).

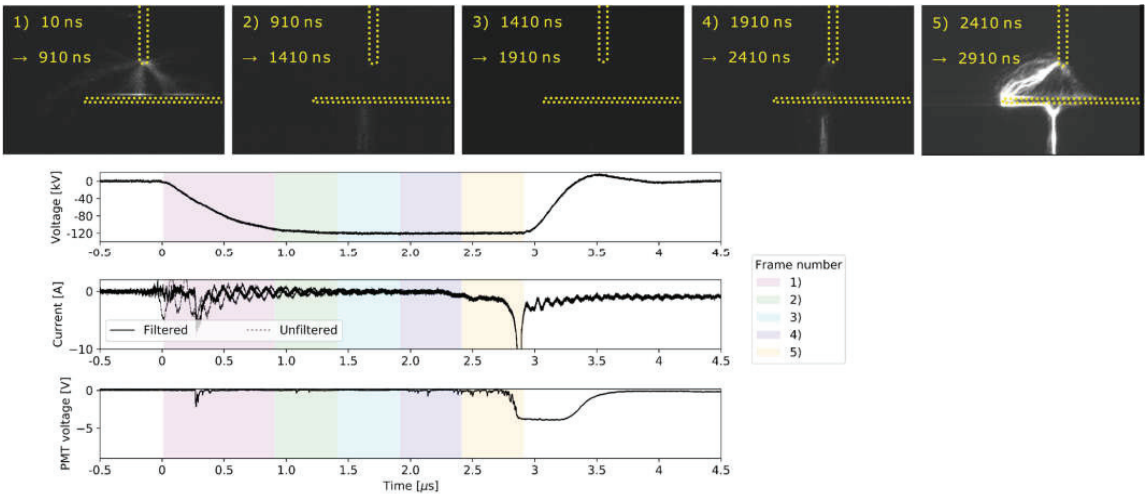

Figure 6. $d = 60$ mm rod-plane gap with barrier at $c = 40$ mm with $b = 40$ mm overhang (see Figure 2), 1.2/50μs LI -124 kV applied. PMT wavelength detection range 360-650 nm with paper filter.

The current during the initial streamer discharges is around 4 A with a rise and fall time of around 30 ns and 500 ns respectively (frame 1 and 2 in Figure 5). The leader current ramps up slowly after the dark period. There is significant light activity in the 495-850 nm range during the initial streamers. The light then fades before returning during the stem development, where a slight increase in PMT voltage is observed in the last part of the cyan color-shaded part of the graph. In the yellow and red frames 5 and 6 the PMT voltage rises close to saturation levels as the leader channel grows in length, thickness and intensity.

The positive breakdown voltages (see Figure 9) fall within the range predicted by equation (2). The positive breakdown voltages of gaps with cleaned barriers are marginally higher than those of rod-plane gaps with similar shortest paths x_S. Positive leader-type channel speeds (Figure 7) generally fall within the expected range of equation (3).

4.2 ROD-PLANE GAP WITH BARRIER UNDER NEGATIVE LI

The image series in Figures 6 and 8 confirm that negative breakdown involves a system of discharge mechanisms of both polarities. Under negative lightning impulse, the negative streamer discharges do not always seem to propagate all the way to ground (see frame 1 in Figure 6). Instead, positive streamers (frame 2) and a leader (frame 5) propagate from the grounded plane right below the rod around the barrier in Figure 6 or directly from the grounded plane to the rod as in frame 3 of Figure 8. The positive and negative streamer channels re-illuminate in frame 4 of Figure 6. The whole leader path is best seen in frame 5 of Figure 6. It starts below the rod and propagates along the lower side of the barrier. As it reaches the end of the barrier, it continues along the shortest path to the rod. Figure 8 reveals that the leader is not necessarily launched from right underneath the rod. Negative leaders were not observed, although a stem appears at the rod electrode during frame 3 in Figure 8.

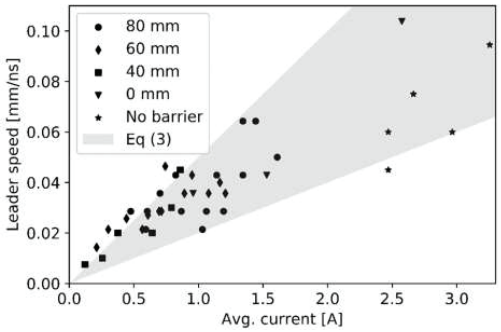

Figure 7. Positive leader speed vs. current, estimated from pictures, $d = 60$ mm rod-plane gaps with and without barrier at $c = 40$ mm (see Figure 2). 41 data points, compared with equation (2). Marker shape indicates barrier overhang b. Each point represents an image with known exposure time, such as frame 6 in Figure 5. During that frame, the leader propagates approximately 30 mm. The average current during the frame (red color-shaded area) is 1.11 A.

The current development during negative and positive LI are similar. The first current pulse during the negative streamer propagation (frame 1 in Figures 6 and 8) has similar amplitude and shape as the positive streamer pulse in Figure 5, but with opposite polarity. After a dark period, the current quickly rises to breakdown as the leader connects the plane to the rod. The over-current protection is activated at the end of frame 5 in Figure 6 and frame 3 in Figure 8. Light is recorded at the same time as the current. In Figure 6, the paper filter ensures that the PMT is not saturated before the arc phase. The PMT in Figure 8, however, is almost saturated directly during the initial streamers. The re-saturation during frame 2 indicates the inception time of the positive streamer or stem from the ground plane.

Negative breakdown voltages increase with roughly 1.2 kV/mm for gaps without barriers, and 0.9 kV/mm for gaps with

barriers (see Figure 9). These are typical field strengths required for negative streamer propagation [10].

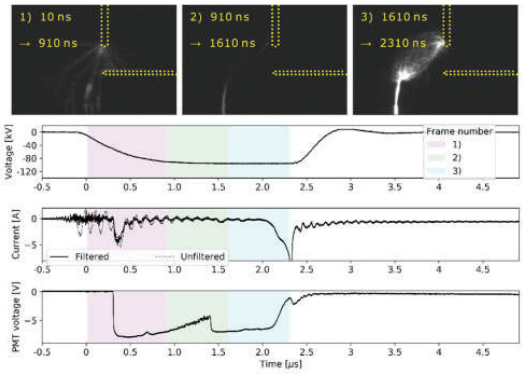

Figure 8. $d = 60$ mm rod-plane gap with barrier at $c = 40$ mm with $b = 0$ mm overhang (see Figure 2), 1.2/50µs LI -124 kV applied. PMT wavelength detection range 360-850 nm.

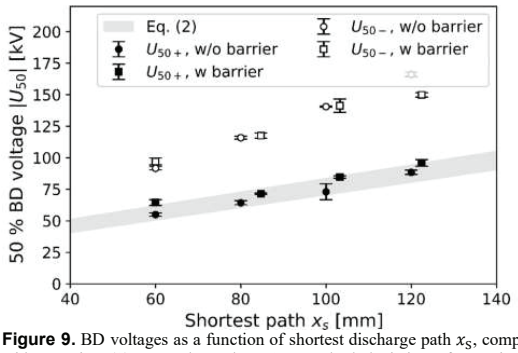

Figure 9. BD voltages as a function of shortest discharge path x_S, compared with equation (2). Error bars show 1σ standard deviation of experimental values. Round markers represent barrier-less gaps, squares gaps with barriers. Black and white color indicate positive and negative polarity respectively. All breakdowns were leader-like.

5 DISCUSSION

5.1 DISCHARGE DEVELOPMENT UNDER POSITIVE IMPULSE

Although the surface charge from initial streamers should amplify the field in the barrier-plane gap (Figure 3a), it is apparently not enough to support streamer discharges in this region. Instead, the charge shields the rod, resulting in the inception of a leader higher up on the rod, following the "leader-type channel" breakdown development described in [15].

The influence of the barrier is therefore mainly geometrical, increasing x_S (Figure 2). An additional increase in x_S is achieved as the leader inception point shifts up on the rod as in Figure 5. This shift is a result of residual charge from the initial streamers on the barrier and in the air. The effect is also seen in rod-plane gaps without barriers [19], [23], but it is more pronounced with barriers as the surface charge is less mobile than the space charge. The longer leader discharge path could explain why breakdown voltages of rod-plane gaps with dielectric barriers tend to be higher than rod-plane gaps with similar x_S (Figure 9).

It can be concluded from Figure 7 that the leader-type channels exhibit similar current-velocity relationships as leaders. This supports the view that leader discharges are not restricted to large gaps only, i.e. that leaders and "leader-type channels" are the same.

When the distance between leader and ground is short, there is more intense discharge activity at the leader front. This explains the somewhat higher average current and leader speed in gaps without a barrier, or when the barrier is at $b = 0$ mm (see Figure 7).

5.2 DISCHARGE DEVELOPMENT UNDER NEGATIVE IMPULSE

The negative charges on the barrier (see Figure 3b) cause positive streamer development from the ground plane up to the barrier. The field amplification on the ground plane is likely largest just below the rod, where the streamer starts in Figure 6. In Figure 8, however, the positive streamer starts at a distance from the barrier, to the left in the image.

Negative leaders and space stems as described in [20] are not observed, and probably require larger gaps to form. The fact that breakdown voltage is higher for negative polarity (Figure 9) is within expectations.

For a positive polarity and a given shortest discharge path x_S, the barrier measurements are associated with a slightly higher breakdown voltage than the corresponding data points of the pure air gap. The negative polarity does not show this consistency (Figure 9). A possible explanation is that the negatively charged barrier facilitates development of positive streamers and leaders from the ground plane when the barrier charge is negative.

6 CONCLUSIONS

Lightning impulse breakdown mechanisms of short rod plane air gaps with a dielectric barrier have been studied. With positive polarity applied, the breakdown mechanism constitutes positive primary streamers and the subsequent inception and propagation of a leader. Under negative impulses, negative streamers charging the barrier are followed by the inception of positive streamers propagating from the ground plane towards the barrier. A leader discharge, which propagates from the ground plane along the lower side of the barrier to the rod, is the ultimate cause of breakdown. Positive breakdown development is similar to that of leaders in larger gaps. The findings have implications for breakdown prediction models for short air gaps, which are typically based on assumptions of breakdown by streamer inception and propagation only. The dielectric barriers increase breakdown voltage by elongating the leader path and shifting the point of leader inception away from the barrier.

7 ACKNOWLEDGEMENT

This work is part of the project "Electrical insulation with low-GWP gases" (project number: 245422) funded by the

Research Council of Norway and the industrial partners ABB AS, Norway and ABB Switzerland Ltd.. The authors would also like to thank Dag Linhjell at SINTEF Energy Research, Norway, for all his help with the experimental set-up.

REFERENCES

[1] S. Solomon, D. Qin, M. Manning, Z. Chen, M. Marquis, K. B. Averyt, M. Tignor, H. L. Miller, and others, " Contribution of working group I to the fourth assessment report of the intergovernmental panel on climate change, 2007". Cambridge University Press, Cambridge, 2007.

[2] Petcharaks, Komson, "Applicability of the streamer breakdown criterion to inhomogenous gas gaps," PhD thesis, 1995, Swiss Federal Institute of Technology, Zürich

[3] A. Pedersen and A. Blaszczyk. "An Engineering Approach to Computational Prediction of Breakdown in Air with Surface Charging Effects," IEEE Trans. Dielectr. Electr. Insul., vol. 24, pp 2775-2783, 2017

[4] Z. Qiu, J. Ruan, C. Huang, W. Xu, L. Tang, D. Huang, and Y. Liao, "A method for breakdown voltage prediction of short air gaps with atypical electrodes," IEEE Trans. Dielectr. Electr. Insul., vol. 23, pp. 2685–2694, 2016.

[5] F. Mauseth, J. S. Jørstad, and A. Pedersen, "Streamer inception and propagation for air insulated rod-plane gaps with barriers," in *Annual Report IEEE Conference on Electrical Insulation and Dielectric Phenomena (CEIDP)* 2012, pp. 739–732.

[6] S. M. Lebedev, O. S. Gefle, and Y. P. Pokholkov, "The barrier effect in dielectrics: The role of interfaces in the breakdown of inhomogeneous dielectrics," IEEE Trans. Dielectr. Electr. Insul., vol. 12, pp. 537–555, Jun. 2005.

[7] T. Kouno, "Breakdown of Composite Dielectrics: The Barrier Effect," IEEE Trans. Dielectr. Electr. Insul., vol. 15,pp. 259–263, 1980.

[8] International Electrotechnical Commission, "IEC 62271-1 High voltage switchgear and controlgear Part 1: Common specifications," 2008.

[9] I. Gallimberti, "The mechanism of the long spark formation," Journal De Physique, Colloquium C, 1979, vol. 7, pp. 193–250.

[10] A. Küchler, *High Voltage Engineering: Fundamentals-Technology-Applications*. Springer, 2017.

[11] S. Singh, Y. V. Serdyuk, and R. Summer, "Streamer propagation in hybrid gas-solid insulation," in *Annual Report IEEE Conference on Electrical Insulation and Dielectric Phenomena (CEIDP)*, 2015, pp. 387–390.

[12] J. Qin and V. P. Pasko, "On the propagation of streamers in electrical discharges," J. Phys. D: Appl. Phys., vol. 47, p. 435202, 2014.

[13] G. Wormeester, S. Pancheshnyi, A. Luque, S. Nijdam, and U. Ebert, "Probing photo-ionization: Simulations of positive streamers in varying N 2 : O 2 -mixtures," J. Phys. D: Appl. Phys., vol. 43, p. 505201, 2010.

[14] G. E. Georghiou, A. P. Papadakis, R. Morrow, and A. C. Metaxas, "Numerical modelling of atmospheric pressure gas discharges leading to plasma production," J. Phys. D: Appl. Phys., vol. 38, p. R303, 2005.

[15] H. Kojima *et al.*, "Classification of impulse breakdown mechanisms under non-uniform electric field in air," IEEE Trans. Dielectr. Electr. Insul., vol. 23, no. 1, pp. 194–201, Feb. 2016.

[16] A. Haddad and D. F. Warne, *Advances in High Voltage Engineering*. IET, 2004.

[17] I. Gallimberti, G. Bacchiega, A. Bondiou-Clergerie, and P. Lalande, "Fundamental processes in long air gap discharges," Comptes Rendus Physique, vol. 3, pp. 1335–1359, 2002.

[18] A. Bondiou and I. Gallimberti, "Theoretical modelling of the development of the positive spark in long gaps," J. Phys. D: Appl. Phys., vol. 27, p. 1252, 1994.

[19] H. K. H. Meyer, F. Mauseth, A. Pedersen, M. Husøy, and J. Ekeberg, "Breakdown in short rod-plane air gaps under positive lightning impulse stress," in *Proceedings of the Nordic Insulation Symposium,* 2017.

[20] V. Cooray, *The Lightning Flash*. IET, 2003.

[21] J. E. Mark, *Polymer data handbook*. Oxford University Press, 2009.

[22] H. K. Meyer, F. Mauseth, A. Pedersen, and J. Ekeberg, "Streamer propagation in rod-plane air gaps with a dielectric barrier," in *Annual Report on IEEE Conference on Electrical Insulation and Dielectric Phenomena*, 2016, pp. 1037–1040.

[23] T. Kitamura, H. Kojima, N. Hayakawa, K. Kobayashi, T. Kato, and T. Rokunohe, "Influence of space charge by primary and secondary streamers on breakdown mechanism under non-uniform electric field in air," in *Annual Report IEEE Conference on Electrical Insulation and Dielectric Phenomena*, 2014, pp. 122–125.

[24] I. Gallimberti, G. Marchesi, and L. Niemeyer, "Streamer corona at an insulator surface," in *7th international symposium on High voltage engineering*, 1991, pp. 26–30.

[25] H. K. Meyer, F. Mauseth, A. Pedersen, and M. Husøy, "Surface charging of dielectric barriers by positive streamers," in *Annual Report IEEE Conference on Electrical Insulation and Dielectric Phenomena, 2017, pp. 802–806*

Hans Kristian Meyer received his MSc degree in Electric Power Engineering from the Norwegian University of Science and Technology (NTNU) in Trondheim, Norway. He is now a PhD Candidate at NTNU.

Frank Mauseth received his MSc degree in Electrical Engineering from Delft University of Technology, The Netherlands, in 2001. Since then he has been with the Norwegian University of Science and Technology (NTNU) in Trondheim, Norway, where he received his PhD degree in 2007 and is now an Associate Professor. Main fields of interest are high voltage insulation materials and systems, measurement methods and testing. Is currently active within the IEEE DEIS TC "HVDC Cable Systems" and CIGRÉ WG D1.48

Atle Pedersen received the M.Sc. degree and the PhD degree in electrical power engineering from the Norwegian University of Science and Technology (NTNU), Trondheim, Norway in 1994 and 2008 respectively. He has worked at ABB Distribusjon in Skien, Norway from 1994 – 2001. He has been in SINTEF Energy Research since 2006. His fields of interest include high voltage switchgear, power cables, and testing of high voltage apparatus. His research work also includes dielectric, electromagnetic and electro thermal simulations of power devices.

Jonas Ekeberg received his MSc degree in engineering physics from Uppsala University, Sweden, in 2003 and his PhD degree from Umeå University, Sweden, in 2011. He then joined ABB Corporate Research in Switzerland as a scientist with focus on high voltage insulation phenomena.

Paper V

presented at the IEEE International Conference on High Voltage Engineering and Application (ICHVE) 2018, Athens

Surface charging of dielectric barriers in short rod-plane air gaps – experiments and simulations

Hans Kristian Meyer*, Andreas Blaszczyk†, Michael Schueller‡, Frank Mauseth* and Atle Pedersen§
*NTNU – Norwegian University of Science and Technology, Trondheim, Norway
†ABB Ltd., Baden-Dättwil, Switzerland
‡University of Applied Sciences Rapperswil, Institute for Energy Technology, Switzerland
§SINTEF Energy Research, Trondheim, Norway

***Abstract*—Surface charge on dielectric surfaces can alter the field conditions of insulation systems substantially. In this work, lightning impulse experiments are compared with a simulation model for surface charging in rod-barrier-plane geometries. The model is based on the saturation charge assumption, i.e. zero normal electric field in air pointing onto the dielectric surface, which prevents further charging. This hypothesis holds well for most geometries, as long as there are no leader discharges or restrikes (also known as back discharges). Restrikes are discharges that occur on the lightning impulse tail when the active electrode is close to zero potential. A method is proposed to compute the charge distribution after a restrike. Furthermore, the model can predict discharges on both sides of the barrier. Saturation charge fields can be computed efficiently, so the results are encouraging for dielectric design applications.**

I. Introduction

Accurate modelling of surface charging phenomena is important for the development of SF_6-free insulation systems for the next generation of medium voltage switchgear. Discharges can be tolerated during lightning impulse tests as long as they do not lead to breakdown. Surface charging effects can suppress discharges under such conditions. In this work, experiments are compared with variations of the saturation charge model described in [1]. Lightning impulses are applied to rod-plane air gaps with a dielectric barrier (see fig. 1), and the resulting surface potential is measured. A range of short ($< 100\,\mathrm{mm}$) rod-barrier-plane geometries are used to test the model and obtain an overview of the charging phenomena involved.

II. Experiments

A. Voltage and current

Rod-barrier-plane gaps (fig. 1 and table I) were stressed with 1.2/50 µs lightning impulses (LI). The earth current was monitored using a Pearson 6585 current monitor to ensure that there was a discharge. No breakdowns were observed.

B. Surface potential measurements

A Trek 3455ET probe with a $20\,\mathrm{kV}$ Trek 341B high voltage amplifier was used to measure surface potential after a discharge. The probe zeroes the electric field between itself and the surface by adjusting its potential. After the impulse, the barrier and ground plane were moved along a rail and positioned $5\,\mathrm{mm} \pm 3\,\mathrm{mm}$ from the probe tip. The surface potential on the barrier was then scanned along the center line using a robot stage. In some cases a 2D raster scan was also performed. The barrier was subsequently cleaned with isopropyl alcohol before the next experiment, resulting in a residual surface potential magnitude below $300\,\mathrm{V}$.

Local potential differences smaller than the surface area seen by the probe are not resolved [2]. This circular area can be assumed to be around 6–18 mm diameter [3]. Local charge peaks or sharp gradients are therefore smoothened. To mimic this effect in the simulations, a moving average filter was applied. While the robot is scanning the surface with a speed of $30\,\mathrm{mm\,s^{-1}}$, the surface potential values are sampled

This work is part of the project "Electrical insulation with low-GWP gases" (project number: 245422) supported by the Research Council of Norway and the industrial partners ABB AS, Norway and ABB Switzerland Ltd.

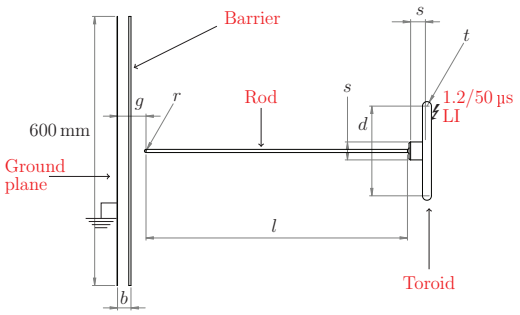

Fig. 1. Rod-barrier-plane model. See table I for parameters. The Lexan barrier was 600x600x5 mm, the ground plane of 600x1000x1 mm. Toroid dimensions: $d = 200\,\mathrm{mm}$, $t = 20\,\mathrm{mm}$, $s = 40\,\mathrm{mm}$.

TABLE I
Rod-barrier-plane configurations in this work (see fig. 1 for parameter illustration)

Parameter	Configuration					
	1	2	3	4	5	6
g [mm]	15	20	10	60	35	60
b [mm]	5	15	5	5	15	40
r [mm]	3.5	3.5	2	3.5	3.5	3.5
l [mm]	590	590	288	ca. 600	590	ca. 600
V [kV]	35	−50	35	54	±50	−100

with 100 samples/s. The moving average filter averages 50 samples, which corresponds to a resolution of 15 mm.

C. Measurements on both barrier sides

In some negative impulse configurations (5 and 6 in table I), multiple discharge events were observed on the measured current, and it was suspected that there could be positive streamers between the barrier and the ground plane (as observed in [4]). To initiate such discharges repeatably, a small protrusion (ca. 1 mm radius copper wire protruding ca. 2 mm) was placed on the ground plane. In addition to the initial surface potential measurement, the barrier was turned around carefully to measure the surface potential on the side that was hypothetically charged by positive streamers starting from the protrusion. Consequently, the side with negative charge delivered from the rod was facing the ground plane during this second measurement.

III. Simulations

First principles simulations of electrical discharges (see e.g. [5]) are still too computationally heavy to be used in everyday insulation design. Simplified calculations are therefore needed. One approach is to assume that surfaces exposed to discharges are charged to saturation, i.e. that the normal electric field component vanishes at the surface facing the air [1].

The advantage with this method is that it can be quickly calculated for arbitrary 3D and 2D geometries. The calculation procedure used in this work is as follows (see also fig. 2 and 3):

1) Calculate background field with zero surface charge and applied voltage U.
2) Evaluate discharge propagation paths (as field lines) and the streamer inception voltage U_i .
3) If a streamer collides with a dielectric surface, assume on an area A_σ of this surface the saturation charge boundary condition and compute the unknown saturation charge σ_sat according to (1) and (2). The outer border of A_σ is determined from the maximum streamer propagation range calculated as applied voltage U divided by the stability fields $E_\mathrm{st,+} = 0.5\,\mathrm{kV\,mm^{-1}}$ for positive and $E_\mathrm{st,-} = 1\,\mathrm{kV\,mm^{-1}}$ for negative polarities.
4) Calculate saturation inception voltage $U_\mathrm{i,sat.}$. If $U_\mathrm{i,sat.} > U$, scale down U until $U_\mathrm{i,sat.} = U$. For the reduced voltage the discharge, and therefore also the surface charging, will be suppressed.
5) Evaluate whether there are new critical field lines that will lead to inception and charging of other surfaces.
6) Ground the active electrode and calculate restrike inception voltage $U_\mathrm{i,res}$. For $U_\mathrm{i,res} \leq U$, the prediction is that there will be restrikes between the dielectric surface and the electrode when it is grounded.
7) If there is a restrike, remove a fraction of the surface charge and calculate the new shape assuming that the normal field is equalized in the region where charge is removed. Change the fraction iteratively until the restrike is suppressed, i.e. $U \leq U_\mathrm{i,res}$.

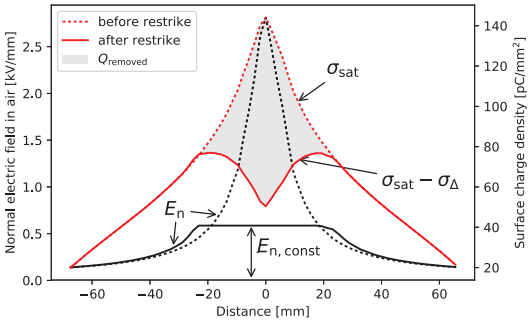

Fig. 2. Charge density and normal field distributions before and after a simulated restrike. The presented values correspond to the configuration 3 in table I. The value of Q_removed is equal to 5 % of the total saturation charge and has been estimated iteratively so that $U = U_\mathrm{i,res}$.

8) Recalculate the field without the active electrode and extract the surface potential for comparisons with experiments.

The following equations are formulated for a point j representing a surface element affected by charging

$$E_\mathrm{n,air},_j - E_\mathrm{n,const} = 0 \tag{1}$$

$$\epsilon_\mathrm{ins} E_\mathrm{n,ins},_j + \sigma_\Delta,_j - \epsilon_\mathrm{air} E_\mathrm{n,const} = \sigma_\mathrm{sat},_j \tag{2}$$

$$\Sigma S_j \sigma_\Delta,_j = Q_\mathrm{removed} \tag{3}$$

These equations allow computation of the ”volcano”-shaped surface charge distribution after a restrike, as shown in fig. 2. S_j is the surface area of a surface element j and $\sigma_\Delta,_j$ is the charge density removed for this element. $E_\mathrm{n,const}$ is an unknown value of the equalized normal field onto the surface. $\sigma_\mathrm{sat},_j$ is the saturation charge accumulated on the surface element j before the restrike occurred. Q_removed is the total removed charge by a restrike, see fig. 2. For the computation of saturation charge, only equations (1) and (2) are used where $E_\mathrm{n,const}$ and $\sigma_\Delta,_j$ are set to zero. $\sigma_\mathrm{sat},_j$ is then moved to the left side of (2) since it is an unknown quantity.

The barrier turning procedure described in sect. II-C was also reproduced in the simulations for comparisons.

IV. Results and Discussion

A. Agreement with saturation charge

The measured surface potential shape is generally close to the simulated potential distribution, see fig. 4. There is some spread within each configuration.

It is often seen that the discrepancy is highest at the center. This is mainly because of *restrikes* (also called back discharges), which create a ”volcano” shape. The discharges have previously been observed by the authors as pulses with some 100 kHz at the tail of the lightning impulse [3]. Five other tested configurations, not included in table I, show similar agreement with the simulation model.

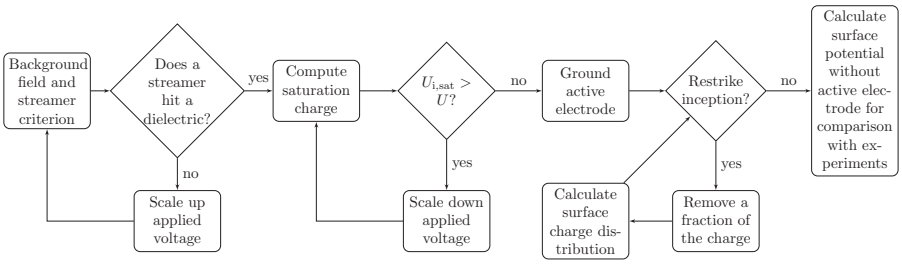

Fig. 3. Flow chart for calculating surface charge distributions, see sect. III.

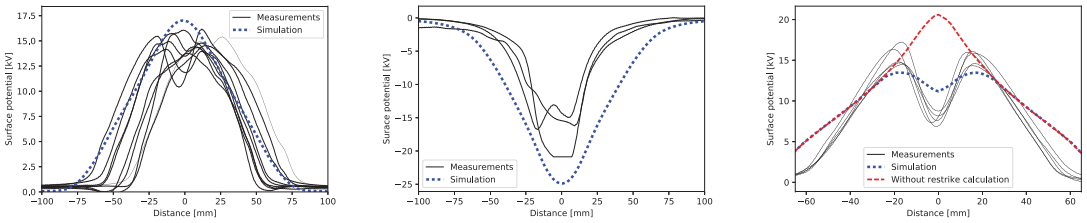

(a) (b) (c)

Fig. 4. The surface potential measured (solid lines) and simulated (dotted and dashed lines) for: a) configuration 1. b) configuration 2, c) configuration 3 (table I for details on the configurations). Due to inception suppression, the simulation voltage has been reduced to 93 % in a). Both the saturation stage and restrike stage computations are shown in c).

The surface charge density distribution variation is primarily due to the following factors:

- Statistical time lag for inception and the stochastic nature of discharge propagation. The effect is especially strong when the inception occurs after the lightning impulse peak.
- Time lag between the impulse and the measurement – this time varied within the range of 2-3 minutes. Ideally the results should be corrected with a decay coefficient that can be found from fig. 6.
- Measurement and positioning errors, which are in the range of 2-3 mm in this work.

B. Charging by leaders

Leaders will charge the surface to a greater extent [6]. This was observed in experiments partly published in [3], see fig. 5. There, the leader discharge leads to higher surface potential than predicted by the simulation model.

As the leader is highly conductive, it can approximately be considered as an extension of the HV electrode. A new saturation charge computation might then give a better fit with the measured charge distribution.

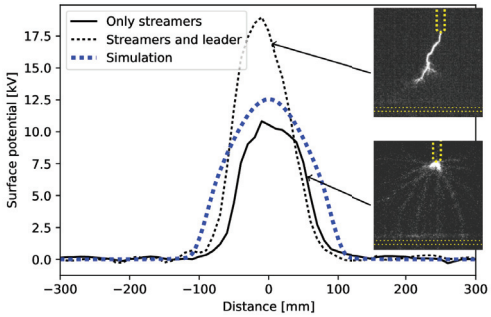

Fig. 5. Leader discharges cause charging above background field saturation charge. Surface potential along the center line and saturation charge after a leader-less discharge. The measurements are taken from a previous publication where a high-speed camera was also used [3]. Image of the discharge with only streamers and image of the measured discharge with an arrested leader inset. Barrier and rod position indicated with dotted yellow lines. Configuration 4 (see table I).

C. Surface potential decay

As can be seen in fig. 6, the potential decays within a couple of hours. When the probe was left near the surface, the decay was slowed down substantially. The probe was therefore moved away between measurements.

As the probe was seen to halt the decay, it seems plausible that the probe stops neutralization by gas ions. The potentials measured are probably slightly lower than those seen during the discharge, as it took around two minutes to move the barrier to the measurement position.

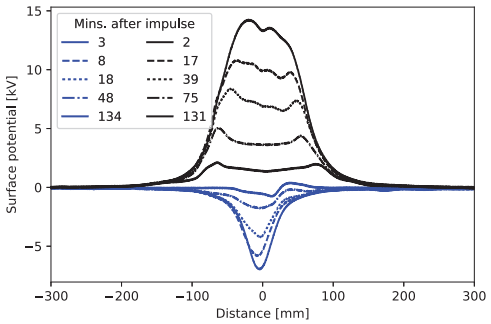

Fig. 6. The surface potential disappears almost completely within two hours. Configuration 5 (see table I). Decay after both a positive and a negative impulse are shown. Interestingly, the amount of charge is smaller for the negative than for positive impulse (at the same applied voltage). This can be explained by larger stability field required for negative streamers to propagate.

D. Restrike prediction

Although there are likely restrikes in several of the measurements in fig. 4, the restrike shape was only computed for one geometry, shown in fig. 4c.

E. Discharges on both sides

Discharges on both sides of the barrier have been previously observed by the authors with a high-speed camera (see fig. 7e and [4], [7]). Experimental scans and simulation of the surface potential on both sides of the barrier after such an event are presented in fig. 7a to 7d.

On the rod side, fig. 7a and 7c, the surface potential is, as expected, negative (similar to the result in fig. 4b). More surprising is the potential distribution on the opposite side (after turning the barrier). There is a significant positive potential in the middle, which confirms the existence of the positive charge. However, the positively charged area is limited since it is surrounded by a negative potential originating from the negative charge on the other barrier side. The simulation, fig. 7d, could well reproduce the trends observed in experiment, fig. 7b. It should be noted that the measurement in fig. 7a was partly out of the probe range (which is ca. 21 kV), so the prediction in fig. 7c could not be reached.

V. Conclusion

This work presents experiments and simulations of charging of a dielectric barrier in rod-plane gaps under lightning impulse stresses. The experimental results are compared with a simulation model based on the assumption of zero normal electric field on the dielectric surface. The model is extended to predict the influence of restrikes and discharges on both sides of the barrier. There is, in general, good agreement between experiments and simulations. The simulation model is computationally inexpensive and applicable to real-life switchgear insulation systems. The reader is referred to [8] for details about the software architecture.

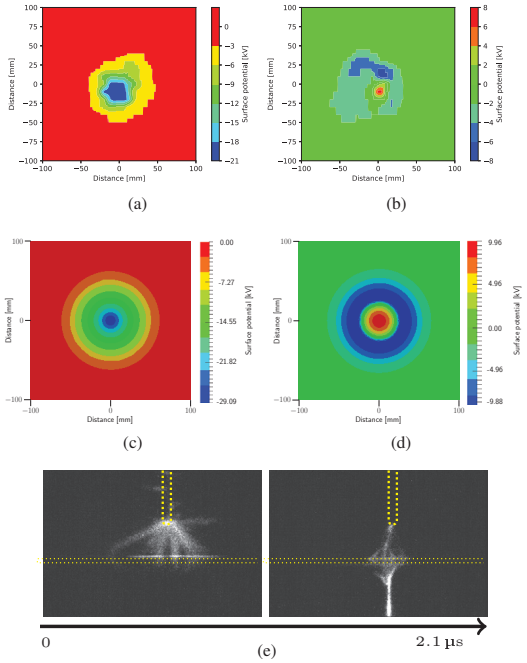

Fig. 7. Discharges on both sides. Configuration 2, with a small protrusion placed centrally on the ground plane to provoke a discharge on the ground side. a) measured on the rod side, b) barrier turned and measured. c) and d) simulations (corresponding to a) and b) respectively). e) High speed image example of discharge development from both the rod and the ground plane (configuration 6, previously published in [7]). Barrier and rod position indicated with dotted yellow lines. Camera frame timing also indicated.

References

[1] A. Pedersen and A. Blaszczyk, "An engineering approach to computational prediction of breakdown in air with surface charging effects," *IEEE Transactions on Dielectrics and Electrical Insulation*, vol. 24, no. 5, pp. 2775–2783, Oct. 2017.

[2] M. A. Noras, "Non-contact surface charge/voltage measurements: capacitive probe—principle of operation," *Trek Application Note*, no. 3001, pp. 1–8, 2002.

[3] H. K. Meyer, F. Mauseth, M. Husøy, and A. Pedersen, "Surface charging of dielectric barriers under positive lightning impulse stress," in *2017 IEEE Conference on Electrical Insulation and Dielectric Phenomenon (CEIDP)*, Oct. 2017, pp. 802–806.

[4] H. K. Meyer, F. Mauseth, A. Pedersen, and J. Ekeberg, "Breakdown mechanisms of rod-plane air gaps with a dielectric barrier subject to lightning impulse stress," *IEEE Transactions on Dielectrics and Electrical Insulation*, vol. 25, no. 3, pp. 1128–1134, Jun. 2018.

[5] A. A. Dubinova, "Modeling of streamer discharges near dielectrics," Ph.D. dissertation, TU Eindhoven, 2016.

[6] J. Deng, H. Mu, G. Zhang, S. Matsuoka, A. Kumada, and K. Hidaka, "Residual Charge Distribution of Surface Leader Discharge Under Positive Impulse Voltage," *IEEE Transactions on Plasma Science*, vol. 41, no. 4, pp. 999–1004, Apr. 2013.

[7] M. Husøy, "Streamer Charging of Dielectric Barriers in Inhomogeneous Air Gaps," Master's thesis, NTNU, Jun. 2017.

[8] A. Blaszczyk, J. Ekeberg, S. Pancheshnyi, and M. Saxegaard, "Virtual High Voltage Lab," in *Scientific Computing in Electrical Engineering - SCEE 2016*, ser. Mathematics in Industry, U. Langer, W. Amrhein, and W. Zulehner, Eds. Heidelberg: Springer, 2018.

Paper VI

presented at the 12th International Conference on Scientific Computing in Electrical Engineering, Taormina

The final published version is available at https://doi.org/10.1007/978-3-030-44101-2_1

Surface Charging Formulations for Engineering Applications. Validation by Experiments and Transient Models

Andreas Blaszczyk, Thomas Christen, Hans Kristian Meyer, and Michael Schueller

Abstract Electrostatic BEM (Boundary Element Method) formulations are presented for the calculation of dielectric surface charging, including saturation and restrike phenomena. The simulation results turn out to be in agreement with surface potential measurements in a simple rod-barrier-plane configuration, where lightning impulses initiate streamers and charge accumulation on the barrier. The usefulness of the given BEM-formulation is additionally supported by transient charging simulations in the framework of an electric carrier drift model.

1 Introduction

Surface charges (SC) on solid insulator surfaces can significantly influence the dielectric performance of medium and high voltage power devices. They can mitigate discharge inception effects during a lightning impulse test, as well as enhance them for applied voltages with reversed polarity. Unfortunately, the simulation of the intrinsically transient charging, which may occur via a zoo of different gas discharge processes like streamers, leaders, ion motion and combinations thereof, is a complex task and thus requires simplified approaches for application to real devices.

Recently a simplified engineering approach based on the saturation-charge boundary-condition has been proposed [1]. It works because saturation is a rather robust extremal stage of SC accumulation that allows assessment of possible changes in field

Andreas Blaszczyk, Thomas Christen
ABB Corporate Research 5405 Baden-Dättwil, Switzerland, e-mail: Andreas.Blaszczyk@ch.abb.com, Thomas.Christen@ch.abb.com

Hans Kristian Meyer
Norwegian University of Science and Technology (NTNU), Trondheim, Norway, e-mail: hans.meyer@ntnu.no

Michael Schueller
University of Applied Sciences Rapperswil, Switzerland, e-mail: michael.schueller@hsr.ch

distribution without performing the full analysis of the charging process. By neglecting the influence of the space charge, a simple electrostatic computation based on integral approach is possible (without meshing the gas volume).

In this paper we present a new formulation of the saturated SC for the 3D boundary element method (BEM), which can be efficiently applied in an industrial design environment. In addition to the saturation stage, computational models for modification of the accumulated charge due to restrikes (back discharges after changes of electrode potentials) are considered. The new formulation is validated based on experiments and transient models. We present results for an example of a rod-barrier-plane arrangement in atmospheric air.

2 BEM Formulation

The formulations presented in the following subsections are focused on new equations enabling surface charging computations. The other parts of the traditional BEM formulation including the Fredholm integral equation of the first order for electrode boundaries as well as the second order for the dielectric boundaries without charge are formulated in the same way as described in [2] and [3] .

All presented formulations are applicable to arbitrary 3D geometries. However, in this paper we explain and validate them for a simple arrangement of rod-barrier-plane shown in Fig. 1a and Fig. 3c. If the applied voltage U_{appl} is larger than the inception voltage U_{inc} at the rod tip (estimated according to [1]) a discharge will start to propagate and initiate the charge accumulation along the barrier surface. All equations are formulated for points i (corresponding to mesh nodes) on the boundary of the dielectric barrier affected by surface charging.

2.1 Saturation

We assume that the saturation stage at the dielectric boundary is achieved when the amount of accumulated SC is so large that the normal component of the electric field in the gas is zero. In order to fulfill the Gauss law, the saturation charge density must then be equal to the flux density on the solid insulation side. In the traditional BEM formulation ([2], [3]), both relationships can be expressed for a collocation point i on a dielectric surface as follows:

$$E_{ni}^{-} + \frac{\sigma_i}{2\varepsilon_0} = 0 \tag{1}$$

$$E_{ni}^{-} - \frac{\sigma_i}{2\varepsilon_0} - \frac{\sigma_{sati}}{\varepsilon_0 \varepsilon_{r,Ins}} = 0 \tag{2}$$

where σ_i and σ_{sati} are unknown densities of the virtual and saturation charges, $\varepsilon_{r,Ins}$ is the relative permittivity of the solid insulation, and E_{ni}^{-} is based on Green's function integration over all surfaces of the model:

$$E_{ni}^{-} = \frac{1}{4\pi\varepsilon_o}\sum_j \int_{S_j} \frac{\mathbf{n_i}\cdot\mathbf{r_{ij}}}{r_{ij}^3}\sigma_j dS \tag{3}$$

where $\mathbf{n_i}$ is the normal vector at collocation point i pointing into the gas and r_{ij} is the distance between collocation point i and the surface element represented by the integration point j. An example of the computed saturation charge distribution σ_{sati} has been shown in Fig. 1b (bell-shaped curve).

2.2 Subsaturation

Saturation is considered as an extremal charging stage, which can be achieved only if a sufficient amount of charge is delivered. However, the accumulated charge may decrease the field strength at original inception points and extinguish the discharge before a saturation is achieved. The reduced value of the density of accumulated charge can be defined as

$$\sigma_{si} = k_{si}\sigma_{sati} \cong k_{sConst}\sigma_{sati} \tag{4}$$

where the reduction factor k_{si} is approximated for simplification by a constant $k_{sConst} \leq 1$ (to be independent of location i). The value of k_{sConst} needs to be estimated iteratively so that at the original inception points $U_{incS} = U_{appl}$, where U_{incS} is calculated with the presence of surface charge. If in the saturated stage $U_{incS} < U_{appl}$ then $k_{sConst} = 1$ and no iterations are required.

In order to solve the subsaturation case, the σ_{si} can be applied to the continuity equation as follows ([2], [3]):

$$E_{ni}^{-} - \frac{\varepsilon_{r,Ins}+\varepsilon_{r,Gas}}{\varepsilon_{r,Ins}-\varepsilon_{r,Gas}}\frac{\sigma_i}{2\varepsilon_0} = \frac{\sigma_{si}}{\varepsilon_0(\varepsilon_{r,Ins}-\varepsilon_{r,Gas})}. \tag{5}$$

2.3 Restrikes

Restrikes, called also back discharges, may occur due to changes of the applied voltage. For example, the maximum voltage applied to the rod during the standard lightning impulse test 1.2/50 μs lasts approximately a few microseconds. The rod is grounded after a few hundreds microseconds. Due to the charge accumulated on the barrier a new inception may be initiated at the grounded rod tip. The new discharge will bring the charge of the opposite polarity to the dielectric, which will recombine with the previously accumulated charge reducing its total amount by a

value of $Q_{removed}$. We assume that in the new equilibrium the normal field strength component at the dielectric will converge to a constant value E_{nConst} within a surface region affected by the charge removal. For a collocation point i within this region the following equations can be formulated:

$$E_{ni}^{-} + \frac{\sigma_i}{2\varepsilon_0} - E_{nConst} = 0 \tag{6}$$

$$E_{ni}^{-} - \frac{\sigma_i}{2\varepsilon_0} - \frac{\sigma_{\Delta i}}{\varepsilon_0 \varepsilon_{r,Ins}} - E_{nConst} \frac{\varepsilon_{r,Gas}}{4\pi\varepsilon_0} = \frac{\sigma_{si}}{\varepsilon_0} \tag{7}$$

The unknown value of E_{nConst} requires an additional equation specifying the amount of removed charge as a fraction of the total accumulated charge:

$$\sum_i \sigma_{\Delta i} S_i = Q_{removed} = (1 - k_{rConst}) Q_{total} \tag{8}$$

where $\sigma_{\Delta i}$ is the surface charge density removed in a point i and S_i is the surface area assigned to point i. The factor k_{rConst}, representing the fraction of the remaining charge, has a value in the range between 0 and 1, which has to be estimated iteratively using the similar criterion like in subsection 2.2: the inception voltage initiating the re-strike U_{incR} should be equal to U_{appl}. The whole restrike computation can be skipped if initially $U_{incR} > U_{appl}$. Examples of the computed charge density (volcano-shaped curve) and normal field distributions are shown in Fig. 1b.

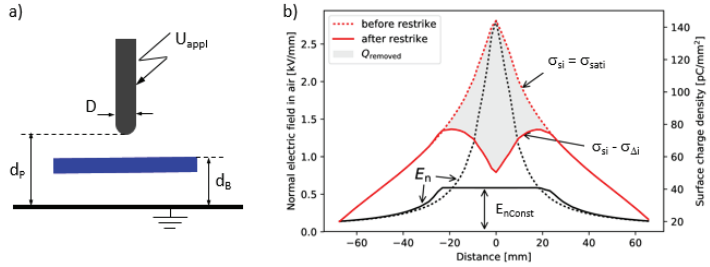

Fig. 1 (a) Rod-barrier-plane configuration. (b) distributions of charge density and normal field strength before and after the restrike calculated for: U_{appl}=35 kV, D=4 mm, d_P=10 mm, d_B=5 mm.

2.4 Surface Potentials

The last step in evaluation of surface charging is the computation of measured surface potentials. Typically a measurement has to be performed in a different geometrical configuration, which may significantly differ from the initial one used

for background field, saturation and re-strikes. This requires re-computation of the whole model while preserving the already computed surface charge. For all charged points i the equations (4) and (5) can be used with the factor $k_{sConst} = 1$ or smaller if decaying effects should be considered.

3 Iterative Procedure

Using a static approach only snapshots of the final or intermediate charging stages can be evaluated. For complex geometrical configurations such an analysis is not straightforward and may require several computational steps in order to properly reflect the process of surface charge accumulation and the related discharge development. We propose an iterative procedure consisting of the following steps:

1. Compute electrostatic background field without any surface charge.
2. Find location of saturation boundary condition and compute the corresponding saturation charge density according to (1)-(3):
   a. Evaluate the critical spots and identify points with the lowest inception voltage
   b. Select a discharge path starting from the most critical point and ending at a dielectric
   c. Find and verify the surface patch for saturation boundary condition. This patch must fulfill the following criteria:
      - it must include the point where the discharge arrived (”seed point”)
      - the initial patch includes all neighboring points with the same orientation of the normal field component as in the ”seed point”
      - the polarity of the resulting charge density must be the same as the polarity of the discharge; points with the opposite polarity of surface charge density must be rejected
      - surface patches detached from the ”seed point” must be rejected
      - all points within the patch must fulfill the stability field criterion [1]: distance from the discharge start point is not larger than $U_{appl}/E_{stability}$.

      Note: For complex geometries the above procedure may require several steps (typically 2-4) including re-computation of saturation charge for the corrected patch. For simple examples like in Fig. 1 the surface patch represented by a circle of approximately 70 mm radius ($= 35kV/0.5kVmm^{-1}$) could be correctly defined within the first iteration.
3. Compute sub-saturation according to (4)-(5) if required.
4. Repeat steps 2 and 3 above if new inception points and possible discharges appeared due to computed surface charge. For example, the charge accumulated on the top of the barrier in Fig. 1a can trigger a new inception bellow the barrier, which will bring the charge of opposite polarity to the barrier bottom.
5. Compute re-strikes according to (6)-(8) if required.
6. Compute surface potentials for comparison with measurements.

4 Experimental Validation

The experimental test arrangement includes a HV rod with diameter D=7 mm (or 4 mm), a dielectric barrier 600x600x5 mm with $\varepsilon_{r,Ins}$=3, and a grounded plate electrode. The rod-barrier distance, d_B, and rod-plate distance, d_p, vary between 0 and 100 mm. A standard lightning voltage impulse (LI) with 1.2/50 μs and a peak value in the range between 20 and 100 kV is applied to the rod. The positive streamer discharge initiated at the spherical rod tip r=3.5 mm (or 2 mm) deposes SC at the barrier surface. After the impulse and a possible restrike the barrier together with the grounded plane are moved to another location where the surface potential due to accumulated charge is scanned by a robot-driven measurement probe. Before applying the next impulse the barrier is cleaned with alcohol in order to remove the SC.

For comparison between computations and experiment we selected 3 geometrical configurations representing different combinations of computational steps in the iterative procedure from section 3: **(a)** subsaturation with k_{sConst} = 0.975, Steps: 1,2,3,6 **(b)** re-strike with k_{rConst} = 0.95, Steps: 1,2,5,6 **(c)** charge accumulated on both barrier sides due to inception triggered by a small protrusion placed at grounded plate under the rod, Steps: 1,2,4,6. The corresponding comparisons presented in Fig.2 show reasonable agreement. Multiple measurement curves illustrate the statistical behavior obtained when repeating the experiments. More experimental results are included in [4].

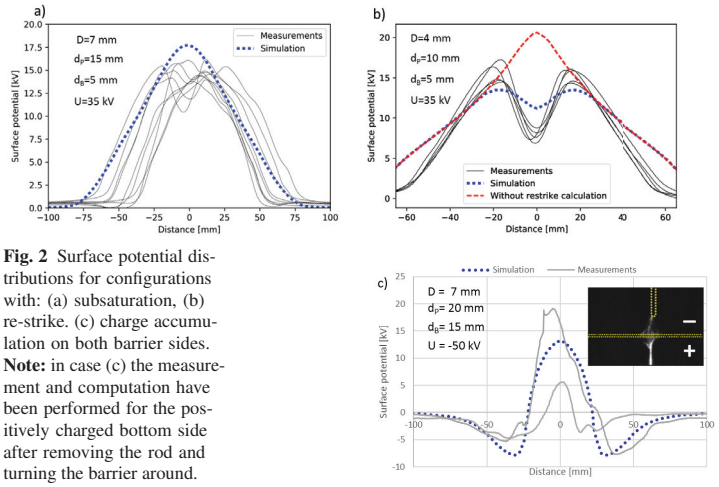

Fig. 2 Surface potential distributions for configurations with: (a) subsaturation, (b) re-strike. (c) charge accumulation on both barrier sides. **Note:** in case (c) the measurement and computation have been performed for the positively charged bottom side after removing the rod and turning the barrier around.

5 Validation with a Transient Drift-Diffusion Model

Surface charging is, in general, a dynamic process, and should thus be simulated with a transient simulation. Note that the iterative procedure discussed in Sect. 3 mimics a kind of transient charging. Of course, there are different types of charging processes, e.g., by streamers, Corona, or DC ion drift, etc. with different physics and which may thus lead to different details of the final charge distributions. Here we show for a specific illustrative example that the previous approach reproduces well the result, which is obtained from a drift-diffusion model for space charge. The details of the drift-diffusion model are described in Refs. [5, 6] and will not be re-iterated here. It consists of the drift-diffusion equation for charge carriers with a mobility μ, which are injected from the contact. In principle, one can take into account in this model [5, 6] the effect of space charge in the Poisson equation, the effect of suppression of the inception in the electrode boundary condition model for charge injection, and the stability field in the carrier drift model. But we will only include here the effect of the surface charge density, σ, in the Poisson equation, disregard all other effects, and compare the result with the approach of Sect. 3. Surface charging is modeled by a local surface-charge source term on the solid dielectric surface, $d\sigma/dt = j$, where j is the normal component of the current density onto the dielectric surface. The surface charge density is thus just the time integral of the current density.

The cylindrically symmetric geometry allows to perform the simulations in 2d

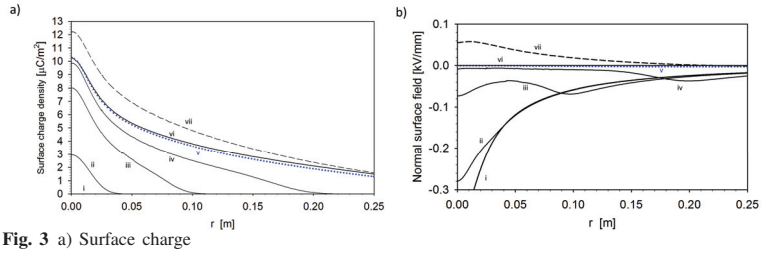

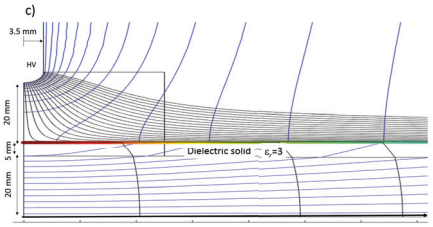

Fig. 3 a) Surface charge and b) normal surface field at different times during the transient charging up. i: capacitive state, ii: 0.2 μs, iii: 1 μs, iv: 10 μs, v: 100 μs, vi (blue dots): exact normal field nullification (Sect. 3), vii (dashed): with space charge (see text). c) Simulated final state: equipotential curves (blue), field lines (black), and surface charge (color) (the box contains a refined mesh).

cylindrical coordinates (r,z). Furthermore, although we will not discuss details of the charging dynamics, we mention that there are two quantities which affect the duration of the charging process: the speed of the charge propagation, and the injection current density. The speed is generally very high for streamers as compared to, e.g., ion drift velocities. Although it is rather artificial to model streamers by a charge density cloud, we will assume a carrier mobility of $\mu \approx 0.1$ m^2/Vs, which leads in fields of the order of a few kilo-volts per millimeter to velocities which are comparable to typical streamer velocities. Nevertheless, due to the artificiality of the model, the mobility value should not be taken too serious but rather as a mean to control the characteristic time scale.
The simulation results are shown in Fig. 3. Parts a) and b) provide the space charge and field distributions, respectively, at different times during charging up. The final saturated state (curve v) is in good accordance with the normal field nullification approach obtained from a separate simulation, shown as curve vi. Of course, if one includes further phenomena, like space charge effects, the normal field component does not necessarily vanish on charged surfaces. As an example, the dashed curves in Fig. 3a and 3b show the result for a case study, where the transient is simulated with taking space charge into account. The presence of space charge increases the accumulated saturation charge density by approximately 20 % (curve vii in Fig. 3a). After charging (steady state) the space charge is removed, such that the final field distribution is only due to the applied voltage and the surface charge. The normal field, which nullifies in presence of space charge, leads to a nonzero reversed field when the positive space charge is removed (curve vii in Fig. 3b). However, the inclusion of space charge can lead to a strongly nonlinear behavior (e.g., the formation of space charge limited currents [5,6]), and requires additional justification and validation which is not the purpose here.

6 Conclusion

A comparison with experiments and transient modelling indicates that the numerically efficient steady-state surface charging model based on the discussed saturation concept can be used for a reasonable prediction of electric fields during high voltage tests.

References

1. A. Blaszczyk, J. Ekeberg, S. Pancheshnyi, and M. Saxegaard. Virtual High Voltage Lab. SCEE 2016, Springer ser. Mathematics in Industry, Heidelberg 2018.
2. N. De Kock, M. Mendik, Z. Andjelic and A. Blaszczyk. Application of 3D boundary element method in the design of EHV GIS components. *IEEE Mag. on Electrical Insulation*, Vol.14, No. 3, pp. 1722, May/June 1998.

3. A. Blaszczyk, Region-oriented BEM formulation for numerical computations of electric fields SCEE 2008, Springer ser. Mathematics in Industry, Heidelberg 2010.
4. H.K. Meyer, A. Blaszczyk, M. Schueller, F. Mauseth, A. Pedersen. Surface charging of dielectric barriers in short rod-plane air gaps - experiments and simulations. *IEEE Conf. on High Voltage Engineering and Application, .* ICHVE September 2018, Athens, Greece.
5. T. Christen. FEM Simulation of Space Charge, Interface and Surface Charge Formation in Insulating Media. *XVth International Symposium on High Voltage Engineering*, Ljubliana, Slovenia, 2007, 7, T8-54, 2007.
6. T. Christen. Nonstandard High-Voltage Electric Insulation Models. *Comsol Conference, Milano, Italy, (2012).*

Paper VII

to appear in IEEE Transactions on Dielectrics and Electrical Insulation, August 2019

Streamer and Surface Charge Dynamics in Non-Uniform Air Gaps with a Dielectric Barrier

Hans Kristian Meyer and **Frank Mauseth**
NTNU – Norwegian University of Science and Technology
Department of Electric Power Engineering
Trondheim, Norway

Robert Marskar and **Atle Pedersen**
SINTEF Energy Research
Trondheim, Norway

Andreas Blaszczyk
ABB Ltd.
Baden-Dättwil, Switzerland

ABSTRACT

Streamer behaviour near dielectric surfaces is an important characteristic of air-solid electrical insulation systems. Accurate predictions are important for dielectric design, but dynamic aspects such as surface charging during streamer propagation are not well understood. A drift-diffusion model is used here to simulate positive streamer behaviour in non-uniform fields. The 2D-planar simulation domain includes air gaps between a tip of a HV electrode and a dielectric barrier laying on a grounded plane. The resulting surface charge distributions approach saturation charge conditions, i.e. zero normal electric field on the air side of the boundary. Such charging behaviour was also reported in lightning impulse (LI) experiments. The simulations are also aligned with empirical streamer propagation range estimates. It is demonstrated that saturation charge levels are reachable within a few tens of nanoseconds of exposure to positive streamer channels. Ion drift is shown to be the dominating mechanism of surface charging during positive streamer propagation, although photoemission also plays an important role. Discharge suppression by streamer-deposited surface charge is also demonstrated. Furthermore, the influence of back discharges at the LI tail on the surface charge distribution is shown. Simulating realistic streamer surface charging behaviour with arbitrary electrode and dielectric shapes is an important step toward first principles discharge prediction models.

Index Terms — **gas discharges, gas insulation, dielectrics, surface charging, air gaps, surface discharges, electron emission, plasma simulation**

1 INTRODUCTION

PREDICTING discharge behaviour is important in many high voltage applications. Charging of dielectric surfaces may affect the insulation properties of a high voltage device significantly. Recent experiments on rod-barrier-plane air gaps under lightning impulse voltage (LI) have shown that charging by streamers can be estimated with a zero (saturation) or equalized normal electric field at the charged surface [1]. Such conditions can be computed with electrostatic simulations. They can therefore be used to evaluate surface charging during voltage tests in complex geometries [2]. If surface charge effects are predictable, they can be used to the benefit of the insulation system. It is, for example, conceivable that surface charging by streamers may inhibit the secondary discharge phenomena necessary for LI breakdown [3-5]. Such aspects can only be explored in detail with dynamic simulation models and experiments.

The dynamics of surface charging by streamers are in general not well known. The streamer-exposed surface is charged by drifting ions or electrons from the streamer channel and by electron emission processes from the dielectric surface [5]. These mechanisms occur in different regions of the streamer and on different time scales, and their relative importance is not clear. The aim of this work is therefore to investigate, using drift-diffusion simulations, the dynamics of

Manuscript received on 12 November 2018, in final form 12 February 2019, accepted 14 February 2019. Corresponding author: H.K. Meyer.

streamer-dielectric interaction in short non-uniform air gaps. Specifically, to clarify the time scale, range and mechanisms of surface charging during positive surface streamer propagation. Also, to understand how saturation charge levels can be reached during a LI. Another aim is to demonstrate discharge suppression by streamer-deposited surface charge, as this is an important insulation system feature. Furthermore, it is an aim to reproduce the influence of back discharges at the LI tail on surface charge distributions [1,6].

Comparisons of drift-diffusion models with experiments are few when it comes to streamer-dielectric interaction and surface charge accumulation [7,8]. An overarching goal of this work is therefore to demonstrate that drift-diffusion models can reproduce experimentally observed characteristics of streamer discharges near dielectrics.

2 SIMULATIONS OF STREAMERS NEAR DIELECTRIC SURFACES IN AIR

2.1 STREAMER DISCHARGES

If an electron avalanche grows to a critical size (10^6-10^8 electrons), its internal field can sustain discharge processes in relatively low background fields. The field strength around the space charge head is then high enough ($E_{cr} \approx 2.6$ kV/mm for 1 bar air) to support further electron avalanche processes in the vicinity [9]. These so-called streamer discharges can be either cathode-directed (positive) or anode-directed (negative). For positive streamers, the electrons from the secondary avalanches are neutralized by positive charges in the streamer head, leaving behind new positive charge a little closer to the cathode. The secondary electrons are generated by impact ionization and photo-ionization. As the process continues, the space charge wave propagates until it meets the cathode or until the electric field is not able to sustain the ionization processes.

Electron avalanches from negative streamers start from the negative space charge head and propagate toward the anode, into a lower field region. Negative streamers therefore require higher background fields in air than positive ones to propagate. Detailed information on characteristics of negative streamers, which are not the focus of this paper except of back discharges discussed in Section 5.6, can be found in [10].

2.2 DRIFT-DIFFUSION MODELING OF STREAMERS

Drift-diffusion models are widely used to simulate streamers in air [4, 7, 8, 11-19]. They are based on a set of drift-diffusion-reaction continuity equations describing the evolution of each type of charged species i:

$$\frac{\partial n_i}{\partial t} + \nabla \cdot (\mathbf{v}_i n_i - D_i \nabla n_i) = S_i, \tag{1}$$

where n_i is the density of the charged species i. Three species are used in this work: electrons (i=e), positive and negative ions $i = \pm$. $\mathbf{v}_i$ is the drift velocity and D_i the diffusion coefficient. Ion diffusion is usually neglected as it is slow on streamer propagation time scales. The expressions for source terms S_i are given below. If it is assumed that streamer channel currents are low, magnetic fields can be disregarded, and the remaining Maxwell equation for the evolution of the electromagnetic field is Poisson's equation

$$\nabla \cdot (-\epsilon \nabla \Phi) = \rho_f, \tag{2}$$

where Φ is electric potential, ε is permittivity, and ρ_f is the free charge density. The way used to incorporate surface charges in Equation (2) is explained in [16].

Additionally, solutions to a set of radiative transfer equations (RTE) are approximated with the Eddington and three-group approximation [20] to model photo-ionization.

Equations (1) and (2) and the RTEs are coupled through S_i, D_i, and $\mathbf{v}_i$ with the streamer plasma kinetics model described in [11], which has been widely used (e.g. in [15,19]). The source terms S_i are given by:

$$\begin{aligned} S_e &= S_{ph.} + n_e \alpha \,|\, \mathbf{v}_e \,| - n_e \eta \,|\, \mathbf{v}_e \,| - n_e n_+ \beta \\ S_+ &= S_{ph.} + n_e \alpha \,|\, \mathbf{v}_e \,| - n_e n_+ \beta - n_- n_+ \beta \\ S_- &= n_e \eta \,|\, \mathbf{v}_e \,| - n_- n_+ \beta \end{aligned} \tag{3}$$

where α, β, and η are ionization, attachment, and recombination coefficients respectively, for which simplified empirical expressions are given in [11]. Note for example that the same β is used for ion-ion and electron-ion recombination. More accurate reaction rates relevant to streamers in air can be found in e.g. [21] and references therein. $S_{ph.}$ is the photo-ionization source term, see [20] for details.

A charge-neutral uniform density of positive ions and electrons, 10^{10} m^{-3}, which is a typical level inside buildings [21], is applied as a simplified initial condition (same approach as in [7, 12, 18]). Other typical initial conditions in such simulations are constant background ionization rates [15], stochastic charge carrier densities [17] or initial plasma clouds [20–22]. Either way, the initial conditions used here are justified since the goal of computation is the surface charging and not the initial stage of the discharge. One should nevertheless keep in mind that the measured surface charge shows statistical deviations when repeating the same experiment (see measured surface charge in Figure 1). One of the reasons explaining such a behavior may be initial conditions. At the electrodes, there is a free outflow of charged species.

2.3 DIELECTRIC SURFACES IN DRIFT-DIFFUSION MODELS

As the streamer propagates near a dielectric surface, there is a net charge flux (current density)

$$J_\sigma = d\sigma / dt = q_e (F_e - F_+ + F_-) \tag{4}$$

into the surface. J_σ is integrated over time and becomes surface charge σ. q_e is the electron charge, F_e, F_+, and F_- are fluxes of charged species onto the surface. The software (see section 2.4) uses embedded boundaries, so the fluxes are extrapolated from the air to the surface (see [16] for details). Charged species are not emitted from the surface if the extrapolated flux points out of the dielectric:

$$\begin{aligned} F_+ &= \max(0, \tilde{F}_+) \\ F_- &= \max(0, \tilde{F}_-) \\ F_e &= \max(0, \tilde{F}_e) - A(\gamma F_{ph} + \kappa F_+) \\ A &= \begin{cases} 1, & \text{if } \mathbf{E} \cdot \mathbf{n} \le 0 \\ 0, & \text{otherwise} \end{cases} \end{aligned} \tag{5}$$

Here $\tilde{F}_+$, $\tilde{F}_-$, and $\tilde{F}_e$ are linearly extrapolated fluxes from the air to the surface, $\mathbf{E} = -\nabla\Phi$ is the electric field and $\mathbf{n}$ is the surface normal pointing into the air. F_{ph} is the photon flux into the surface (the method of calculating photon fluxes is based on the gradient of the radiative density [16]). Two electron emission mechanisms are implemented in the electron flux F_e: photoemission (γ electrons released per incident photon) and positive ion bombardment (κ electrons released per incident positive ion). These only contribute when the electric field points into the dielectric, hence the conditional A. Emission mechanisms contribute to surface charging, as every emitted electron leaves behind an electron hole, which is equivalent to an immobile, positive surface charge in the model.

Positive and negative ions are not emitted from the surface in the model. If the extrapolated flux is positive, the respective charge carriers are flowing onto the dielectric (becoming surface charge according to Equation (4)). If, on the other hand, the extrapolated flux is negative, the respective charge carriers would normally flow out of surface. To avoid such emission, max() functions are used in Equation (5). The charge exchange at the dielectric surface in the model is limited to charged species drifting onto the dielectric, and emission of electrons due to photon and positive ion bombardment. For ion bombardment, a high value of $\kappa = 0.1$ is used here as in [7, 18]. A low value of $\kappa = 10^{-4}$ was also briefly tried. This parameter does not alter the streamer characteristics in the model, but it accelerates the surface charging rate (the surface charging rate is ca. 10 % higher with $\kappa = 0.1$). γ (photoemission efficiency), depends on both the material and gas properties. Experimental data on photoemission from dielectrics is limited, especially in the presence of a discharge. Estimates for γ fall in the large range from 10^{-7} to 1 for polymers (references can be found in [22]). The photoionization model in this work models only UV-photons around 100 nm, as those are considered to be responsible for photoionization in air. Longer wavelength photons may contribute to photoemission from dielectric surfaces in air, but the effect is small as γ decreases with decreasing photon energy. In this study, γ was set to 10^{-6} and 10^{-1} to study its influence on the surface charge accumulation and positive streamer dynamics.

2.4 IMPLEMENTATION AND COMPUTATIONAL RESOURCES

A finite volume code [16] was used for the dynamic simulations. The implementation uses Cartesian cut cell grids to handle material boundaries and adaptive mesh refinement to limit the grid size. The local mesh size is mainly controlled by the relative electric field strength and its gradient in this work. The same refinement criteria as in [16] are used.

Drift-diffusion simulations of streamers in atmospheric air in realistic geometries are computationally demanding. Streamers span several spatial and temporal scales, with typical minimum resolutions in the low or sub µm and ps range when streamers propagate on dielectric surfaces [22]. The main computational bottleneck is the Poisson's equation [17]. 3D simulations with branching (see e.g. [17]) are required to realistically model streamers, but they are currently too computationally expensive for larger domains with sub µm grids and complex geometries. The simulations here were therefore in 2D, and used up to 512 computer cores when the mesh size was 0.61 µm at the finest level and 312.5 µm at the coarsest. The number of cells varied from a few million to 14 million. The minimum time steps were around 0.3-0.6 ps, mainly controlled with the Courant-Friedrichs-Lewy condition (see [16] for details).

3 ENGINEERING SIMULATIONS BASED ON SATURATION CHARGE

Predicting the influence of surface charge on the dielectric strength of gas-insulated high-voltage devices is still outside of the capabilities of drift-diffusion models. Therefore, a simplified approach based on a saturation boundary condition has been suggested as an engineering approach for complex geometries [1, 2]. The saturation is defined by zero normal field on the air side of a dielectric interface:

$$E_{n,air} = 0, \tag{6}$$

whereas the unknown saturation charge σ_{sat} is balanced by the electric flux density on the solid dielectric side

$$\epsilon_{ins} E_{n,ins} - \sigma_{sat} = 0 \tag{7}$$

Here ε_{ins} is the permittivity of the dielectric and $E_{n,ins}$ the normal field inside the dielectric at the gas-dielectric interface.

The region of the surface where this condition is applied is estimated by assuming that the propagation is limited by the maximum streamer range

$$s_r = U / E_{st}, \tag{8}$$

where E_{st} is the background field required for streamer propagation along insulating surfaces in atmospheric air and U is the applied voltage. For positive streamers along insulating surfaces, $E_{st} \approx$ 0.4-0.6 kV/mm [23]. E_{st} = 0.5 kV/mm is used here.

Commercial finite element method (FEM) software

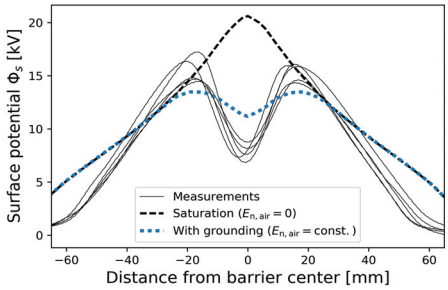

Figure 1 Surface potential measurements on rod-barrier-plane gaps stressed with 35 kV 1.2/50 µs LI [1]. The measured potentials (grey solid lines) are partly close to the predicted saturation (black dashed line based on equations (6)-(8)). The characteristic volcano shape can be explained by back discharges at the LI tail. They can be computed according to [1] by removing a part of the accumulated charge and equalizing the normal electric field (blue dotted line). 2 mm rod radius, tip 10 mm above ground. 5 mm thick polycarbonate barrier resting on the ground plane. 5 independent measurements, surface cleaned and discharged between experiments.

(COMSOL Multiphysics) and an in-house ABB engineering tool called VHVlab based on the boundary element method (BEM) [2] were used to compute saturation charge conditions in this work and in [1]. In [1], the procedure described above (Equations (6)-(8)) was tested with experimental results on rod-barrier-plane gaps under LI (see Figure 1).

4 SIMULATION CASES

Blade-barrier-plane gaps were used for the dynamic and engineering simulations. Since the dynamic code does not support cylindrical coordinates and the 3D code is computationally too heavy, we cannot obtain dynamic results that can be directly compared with the experiments in [1]. Instead, an indirect approach has been applied: for an equivalent 2D-planar arrangement the results of the dynamic code are compared with the results of the experimentally validated engineering codes.

Two simulation geometries were used, see Table 1 and Figure 2. Throughout, the dielectric was 5 mm thick with $\varepsilon_r = 3$, resting on the ground plane and centered. The barrier is assumed to be ideally insulating. The assumption is that on the time scale of the streamer, conduction through the dielectric slab is negligibly slow compared to the conduction in the streamer-ionized air. The barrier edges were rounded with 0.2 mm radius.

A constant potential U was applied in the simulations instead of a 1.2/50 µs LI pulse. The total duration of the simulations was only between 15 and 115 ns. If it is assumed that the first electron avalanche will appear close to the LI peak, the voltage level variation during 115 ns is only a few percent, so a constant potential is a reasonable approximation.

Table 1. Simulation parameters. See also Figure 2.

Parameter	Geometry	
	G1	G2
Domain [mm^2]	40x40	80x20
Blade tip radius [mm]	2	0.5
Blade potential U [kV]	35	14/35
Barrier width [mm]	22	72
Photoemission efficiency γ	10^{-6}/10^{-1}	10^{-6}

5 RESULTS AND DISCUSSION

5.1 COMPARISON WITH SATURATION CHARGE

The drift-diffusion simulations typically show a streamer initiated from the blade tip, propagating vertically, and then hitting the dielectric. It then continues horizontally along the dielectric surface (see illustration in section 5.4, Fig 7). Finally, the streamer propagates around the barrier edge, detaches partly from the surface, and then propagates toward the ground plane. Meanwhile, the surface charge density distribution on the dielectric surface evolves toward saturation levels, see Figure 3.

The streamers in geometry G1 reached the ground plane after around 15.5 ns, whereas the simulations in G2 were stopped before the streamers reached ground. The position of the optical streamer head at the simulation end is indicated in

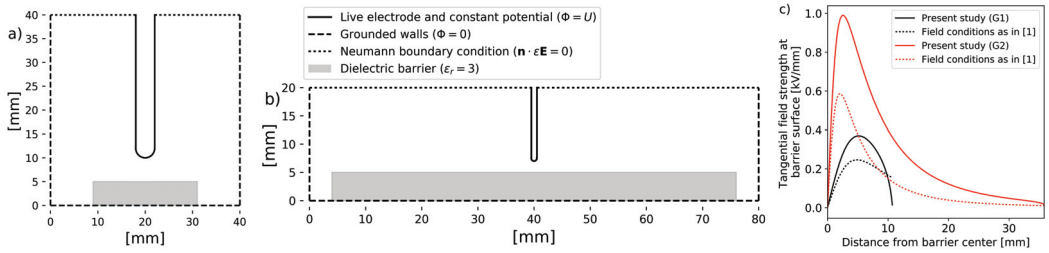

Figure 2 Simulation domains with boundary conditions for the electric field. The simulations are 2D planar, meaning that the dimensions are infinite into and out of the paper. So the geometries are blade-barrier-plane gaps. a) Geometry G1 b) Geometry G2 (See also Table 1). c) distribution of the tangential background field strength E_t along the barrier surface with 35 kV applied to the live electrode. Note: The grounded vertical wall reflects the experimental condition in HV labs. Therefore, we keep the same conditions for both cases in spite of the fact that the computational domain is limited to a rather small area. E_t is higher in the blade-barrier-plane simulations here than in the corresponding rod-barrier-plane gaps in [1]: not due to the reduced distance to vertical grounded walls but because of differences between background field surrounding live electrodes (blade versus rod).

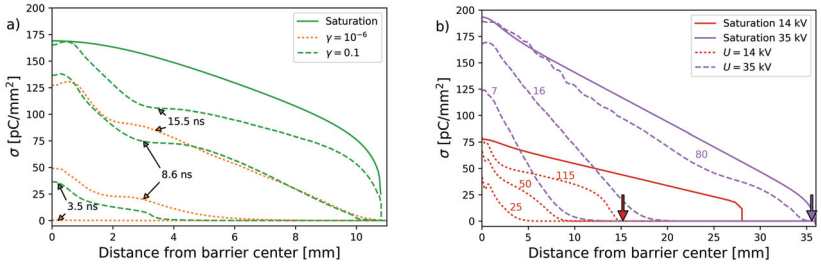

Figure 3 Surface charge density distribution σ (dotted and dashed lines) evolves toward saturation charge σ_{sat} (solid lines) on the dielectric surface. Numerals indicate elapsed simulation time in ns. a) Geometry G1, photoemission increases surface charging rate b) Geometry G2, effect of applied voltage level. Small vertical arrows indicate the optical streamer head position in G2. The simulations in G2 were stopped due to excessive computation time before the streamer reached the edge of the dielectric barrier. The reason is that the streamer slows down in the low-field regions (especially for the 14 kV case). This requires much more time steps that remain small (below 1 ps) and consequently the simulation needs up to a few days on a computer cluster.

Figure 3b. It is the point of the most intense photon production and is obtained from the photon source term.

For the positive ions in the streamer channel to charge the surface up to saturation, the number of positive charge carriers in the streamer channel must exceed the total saturation charge Q_{sat} (negative charge carriers drift away from the dielectric surface and do not contribute to surface charge). The value of Q_{sat} in geometry G1 (Figure 3a) is 2.8 µC/m. so $n_{+,sat}$ = 1.75 x 10^{13}/m positive charge carriers are needed (the values of surface charge and carriers are given here per m due to the 2D planar approximation). Integrating the positive species density in the streamer channel at the time instant in Figure 4a, it contains 4 x 10^{14}/m > $n_{+,sat}$, so there are sufficient charge carriers to reach saturation (ca. 20 times more than needed). Similarly, it was found that there are sufficient charge carriers to reach saturation in the streamer channels in geometry G2.

Charge levels above saturation are also possible, if the electric field distortion from the streamer space charge density (Figure 4b) is substantially higher than the field distortion from the saturation charge density. Most of the streamer channel is a quasi-neutral, i.e. apparently charge neutral, plasma. There are high densities of charge carriers of both polarities in the channel, but they cancel out. However, there is a ca. 20 µm thick layer of space charge partly surrounding the quasi-neutral streamer channel (Figure 4b). All in all, the electric field contribution from the streamer space charge is not high enough to achieve significant super-saturation in the simulations here.

5.1 CHARGING DYNAMICS

The charge carriers must reach and cover the surface within the relevant time scale to charge it. Firstly, the streamer must cross the air gap. The time of crossing depends on the applied field strength (see section 4.4).

As the streamer propagates along the dielectric surface, the comparatively slow positive ions need time to drift onto it. The surface charge decay mechanisms are slow on streamer propagation time scales, so the charge accumulation rate depends mainly on ionization rates, surface emission rates and

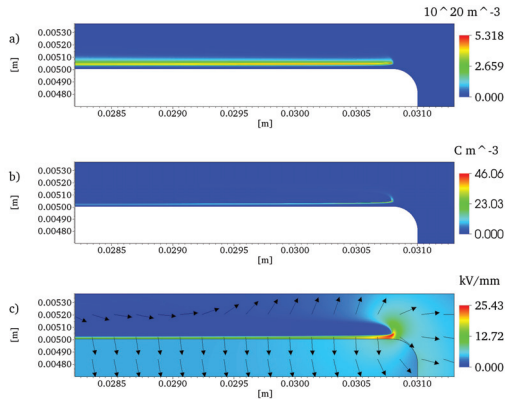

Figure 4 Streamer at the barrier edge in geometry G1 at t = 11.56 ns, with γ = 10^{-6}. a) Density of positive ions in 10^{20} m^{-3} b) Space charge density in Cm^{-3} c) Electric field strength in kV/mm with a few field vectors.

positive ion drift velocities

$$\mathbf{v}_+ = \mu_+ \mathbf{E} = 2.34 \cdot 10^{-4}\ [\mathrm{m}^2 / \mathrm{Vs}] \cdot \mathbf{E} \qquad (9)$$

In the first few tens of µm above the surface in Figure 4c, the field points into the dielectric with a strength of around 10 kV/mm. Such a region with comparatively high field strength and low charge carrier density is typically observed when simulating positive streamer propagation along dielectrics [13]. Its thickness is sensitive to photoemission efficiency as shown in Figure 5. With 10 kV/mm, the positive ion drift speed towards the surface according to equation (9) is around 2 µm/ns. The time needed for the ions to drift onto the surface through the 20-40 µm layer is therefore in the tens of ns, which is fast on a 1.2/50 µs LI timescale. The outer parts of the barrier did not reach saturation before the simulation ended (Figure 3), as they are only exposed to the streamer channel for a few ns.

Charged species are neutralized through recombination, see equation (3) (recombination coefficient β = 2 x 10^{-13} m^3/s [11]). If the recombination in the trailing streamer channel is too fast, the charged species recombine before they can charge the surface to saturation. In the present simulations, the positive species in the quasi-neutral streamer channel are initially being neutralized at a rate of a few 10^{28} $/m^3s$, see Figure 5. As the positive species density behind the streamer head is a few 10^{20} $/m^3$ (see Figure 5), the charged species will be reduced considerably by recombination during some tens of ns. Nevertheless, saturation charge levels are reached before the charged species in the channel are neutralized in the simulations here.

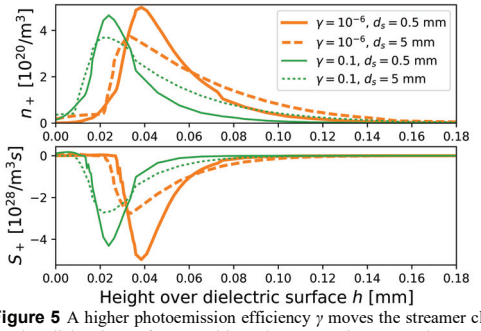

Figure 5 A higher photoemission efficiency γ moves the streamer closer to the dielectric surface. Positive charge species n_+ and source S_+ (equation (3)) above the dielectric surface shown, d_s = 0.5 mm and d_s = 5 mm behind the streamer head. The source is negative since positive species are recombining in the channel. The streamer has propagated 10 mm along the barrier surface (same as in Figure 6). Geometry G1.

5.2 EFFECT OF PHOTOEMISSION

Photons release electrons from the surface in a highly localized region near the streamer head, where the photons are produced (see green solid line in Figure 6). The surface charging contribution from ion drift (dotted lines in Figure 6) therefore dominates in most of the streamer channel. A higher photoemission efficiency γ leads to a quicker charging of the surface (see Figure 3a). Also, the streamer moves closer to the surface (see Figure 5). Therefore, the ion flux into the surface

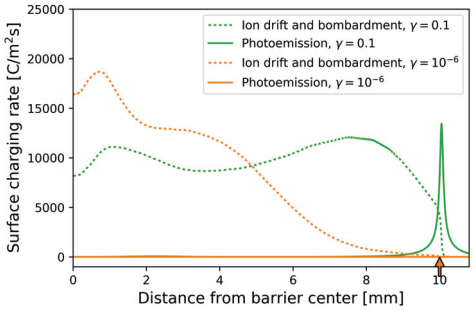

Figure 6 Surface charging by photons (solid lines) is dominant at the streamer head when γ = 0.1, but charging by ion drift (dotted lines) dominates in the rest of the streamer channel. Small vertical arrow indicates streamer head position, which is at 10 mm from the barrier center. γ = 0.1: t = 8.7 ns, green lines. $\gamma = 10^{-6}$: t = 9.9 ns, orange lines. Geometry G1.

is higher in first few mm behind the head of the streamer channel when γ = 0.1 (see green dotted line vs. orange dotted line within the distance range 5-10 mm in Figure 6). With $\gamma = 10^{-6}$, charging by photoemission is negligible along the whole streamer path (orange solid line).

5.3 STREAMER VELOCITY AND STABILITY FIELD

Streamer velocities from 0.1 up to a few mm/ns are typical experimental values in high voltage literature [10], [23], and similar velocities are seen here (see Figure 7 and 8). The velocities increase with voltage and decrease with distance from the live electrode. Positive streamers generally move faster along insulating surfaces than in air, and it has been suggested that photoemission is responsible for this effect [23]. The streamer speed in geometry G1 is a few percent higher when γ = 0.1 than when $\gamma = 10^{-6}$. Another explanation for increased streamer velocity along insulating surfaces in uniform fields is that surface streamers are thinner (Figure 7). This promotes a higher streamer head field, and therefore higher ionization intensity and streamer velocity. In the non-uniform fields used here, however, the streamer slows down along the insulator, as it is moving into regions with low background fields (Figure 7 and 8).

The accuracy of the velocity computation for a streamer propagating along a dielectric surface is sensitive to mesh size. An acceptable accuracy level has been observed for mesh size in the range of 1 µm [14]. Reduction of the mesh size below

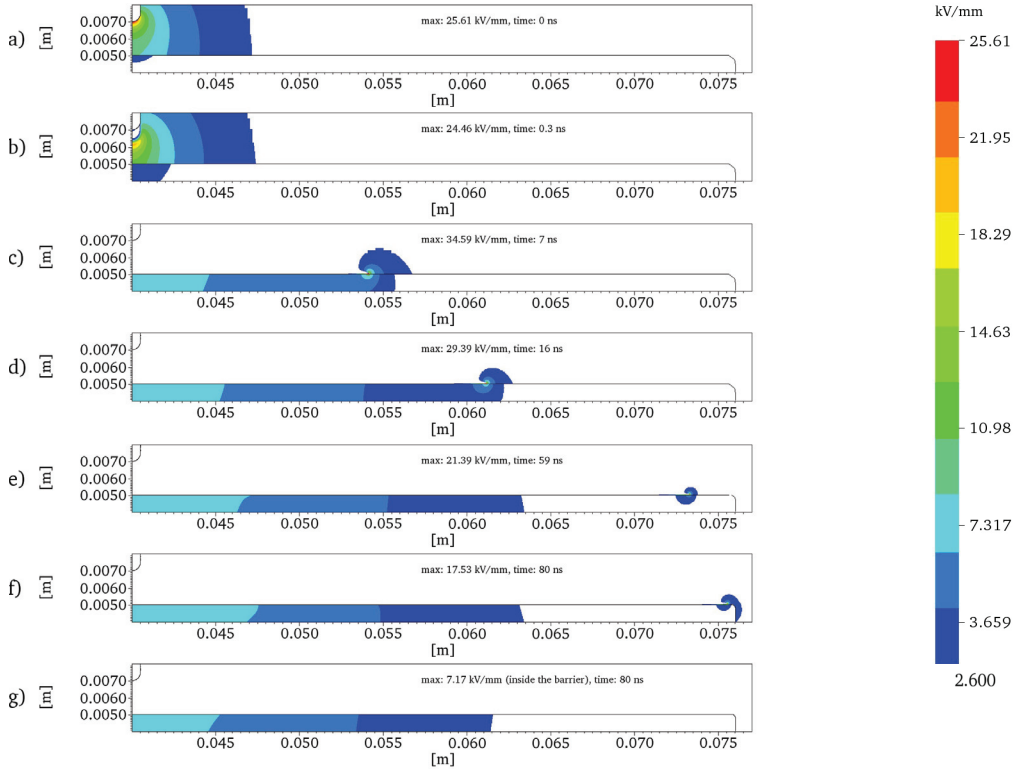

Figure 7 Electric field strength along streamer propagation path for geometry G2, U = 35 kV: a) t = 0 ns (background field), b) t = 0.3 ns (streamer initiated from the blade tip, propagating towards the barrier), c) t=7 ns (streamer propagation along barrier) d) t = 16 ns, e) t = 59 ns, f) t = 80 ns (streamer at the barrier edge) g) electric field after removing the space charge and restarting the simulation at 80 ns (the surface charge is shielding the blade tip, see section 4.5), The field is only plotted in regions where $|\mathbf{E}| \geq 2.6$ kV/mm. Maximum field strength indicated in each plot. The maximum field strength in air is located at the streamer head. Note: As the streamer propagates along and charges the barrier, the electric field strength in air behind the streamer head is reduced below the ionization threshold in air E_{cr} = 2.6 kV/mm (except in the 20-40 µm thin high-field region between the streamer and the surface discussed in section 4.2).

1 µm does not significantly improve accuracy. In the present work a minimum size of 0.61 µm is used.

According to the stability field rule (equation (8)) the streamer in the 14 kV simulation cannot propagate over a distance larger than 28 mm. Consequently, the saturation charge condition has been applied along the barrier surface up to this distance only (red solid curve in Figure 3b). The 14 kV simulation could not be run long enough to confirm that the streamer stops at 28 mm (Figure 8).

However, it can be assumed that the streamer will continue to slow down, as in the 35 kV simulation. Even if it keeps the same speed as it had at the simulation end, it will reach the stability limit for the 14 kV simulation after ca. 400 ns. Considering that the streamer will likely slow down further, it may reach a distance close to the 28 mm limit predicted from equation (8) in a few µs, which fits in to the timescale of 1.2/50 µs LI. Such arrested streamers along insulating surfaces due to low background fields have been observed in pulse voltage experiments [23]. Furthermore, the radius of the surface charged region after a 1.2/50 µs LI was well approximated with equation (8) in [1].

Another confirmation of the stability field concept is provided in the results shown in Figure 9. The average field gradient along the first 15 mm of the surface streamer is 1.2 kV/mm for the 35 kV case, and 0.35 kV/mm for the 14 kV case. Gradient values lower than 0.5 kV/mm indicate that the positive streamer stagnates, and its propagation may stop before reaching the opposite electrode.

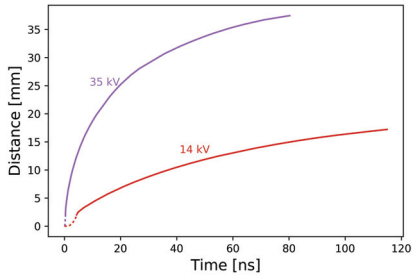

Figure 8 Streamer distance vs time, geometry G2. The 35 kV streamer reaches the barrier edge, but the 14 kV simulation was not run for long enough, and slows down significantly, in support of the stability field concept (equation (8)). Dotted lines indicate propagation in the air gap, solid lines along the barrier.

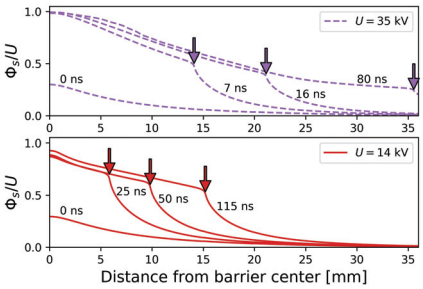

Figure 9 Potential drop along the surface streamer. Surface potential Φ_s on the dielectric surface, normalized to electrode potential U . Elapsed time in ns indicated on each curve. Streamer head position indicated with arrows. Upper plot 35 kV, lower plot 14 kV. Geometry G2.

5.4 DISCHARGE SUPPRESSION BY SURFACE CHARGE

The accumulated surface charge on dielectric barriers can contribute to the LI strength of the insulation system if the exposed points are shielded sufficiently by the streamer-deposited surface charge. Streamers do not automatically cause breakdown, even if they reach the opposite electrode [3]–[5]. If the first streamer does not induce breakdown, the surface charge it deposits on dielectric surfaces may inhibit further discharge activity. The streamer channel will then decay and eventually disappear, leaving surface charge but zero space charge (the surface charge needs a few hours to decay considerably [1]).

Discharge suppression by streamer-deposited surface charge was observed in experiments by the authors (see [1], [3] for description of the experimental setup). For some rod-barrier-plane configurations, an initial LI produced inception (observable with current and surface charge measurements, photo-multipliers and cameras) but additional LIs without discharging and cleaning the surface would not lead to inception.

This effect was investigated in the present work as well. Starting a new simulation with the same initial conditions (resetting the volume charge to a uniform, neutral distribution of 10^{10} m^{-3}), but with the acquired surface charge distribution at the end of the 35 kV simulation (see Figure 7g) did not lead to new discharges, as the field was below the ionization threshold everywhere in air. The field reduction in air due to streamer propagation is evident in Figure 7. As the streamer propagates along the barrier, it shifts the initial high-stress region around the blade tip (Figure 7a) to the insulator and to the streamer head (Figures 7b-7f). The ionization is therefore only sustained near the streamer head and directly behind the head in the thin high-field region between the channel and surface (see section 4.2 and Figure 4c).

Whether and how the streamer-deposited surface charge can inhibit breakdown mechanisms such as leader inception is not investigated here. The streamer-deposited surface and space charge will likely play an important role, as it alters the field distribution considerably [5] (see also Figure 7) .

5.5 BACK DISCHARGE (NEGATIVE STREAMER)

Starting a new simulation with initial conditions for volume charge, but with the acquired surface charge and a grounded HV electrode can lead to a back discharge (negative streamer) initiating from the grounded blade tip. Such a simulation is shown in Figure 10, where the surface charge distribution of the 14 kV geometry G2 simulation is used. Back discharges have also been observed experimentally under LI conditions [1], [6]. They are not disruptive, but they affect the surface charge distribution. Both the resulting volcano-shaped surface potential and negative charging beneath the electrode presented in Figure 10 have been observed in experiments (see Figure 1 and references [1], [6]). Negative streamers (like the back discharge simulated here) differ from positive ones in a number of ways. Importantly, they attach to the surface, leaving no high-field region between the streamer channel and surface. An analysis of the surface charge dynamics of negative streamers is, however, left to another study.

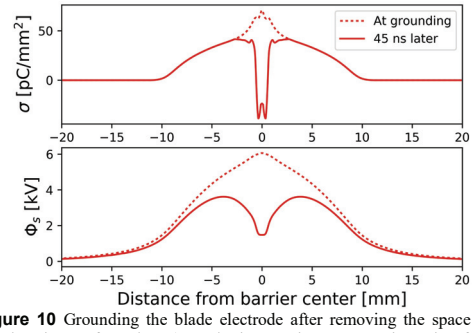

Figure 10 Grounding the blade electrode after removing the space charge (but keeping surface charge) results in negative streamer inception from the blade tip, which changes the surface charge density σ (upper plot) and surface potential Φ_s (lower plot). The resulting characteristic volcano-shaped surface potential is qualitatively consistent with experiments (see Figure 1). Geometry G2,14 kV. Grounding t = 61.2 ns after simulation start.

6 CONCLUSIONS AND NEXT STEPS

In this paper, simulations of positive streamer propagation in 2D planar non-uniform electric fields near dielectric barriers are presented. The results obtained using the drift-diffusion model are compared with surface charge predictions by an engineering tool. The engineering tool uses a saturation charge model that has been validated with experiments in simple rod-barrier-plane geometries stressed with lightning impulse voltages. It is shown that the drift-diffusion simulations reproduce the characteristics of the observed charging behaviour. Simulated streamer ranges are consistent with empirical streamer stability field estimates. In the obtained simulation results, ion drift is the dominating surface charge accumulation mechanism, and saturation is achievable within tens of ns. Furthermore, photoemission from the surface increases the charge accumulation rate in the model. Moreover, surface charge deposited by the streamer suppresses further discharge activity in the simulated geometries.

As drift-diffusion simulation models and computer capabilities are improving, such models may become highly useful in dielectric design applications in the near future. Further steps in the development of such models include computation of streamer-dielectric interaction in atmospheric air, in 3D and in larger 2D domains, and improving plasma kinetics models. An important next step is to model surface charging by a single streamer channel in 3D. Other further steps include simulation of negative streamer-dielectric interaction, simulation of leader inception and simulating the influence of surface roughness on streamer-dielectric interaction.

ACKNOWLEDGMENT

This work is part of the project ”Electrical insulation with low-GWP gases” (project number: 245422) funded by the Research Council of Norway and the industrial partners ABB AS, Norway and ABB Switzerland Ltd..

REFERENCES

[1] H. K. Meyer, A. Blaszczyk, M. Schueller, F. Mauseth, and A. Pedersen, “Surface charging of dielectric barriers in short rod-plane air gaps – experiments and simulations,” in *International Conference on High Voltage Engineering and Application (ICHVE)*, Athens, 2018.

[2] A. Pedersen and A. Blaszczyk, “An engineering approach to computational prediction of breakdown in air with surface charging effects,” *IEEE Trans. Dielectr. Electr. Insul.*, vol. 24, no. 5, pp. 2775–2783, Oct. 2017.

[3] H. K. Meyer, F. Mauseth, A. Pedersen, and J. Ekeberg, “Breakdown mechanisms of rod-plane air gaps with a dielectric barrier subject to lightning impulse stress,” *IEEE Trans. Dielectr. Electr. Insul.*, vol. 25, no. 3, pp. 1128–1134, Jun. 2018.

[4] H. Kojima *et al.*, “Classification of impulse breakdown mechanisms under non-uniform electric field in air,” *IEEE Trans. Dielectr. Electr. Insul.*, vol. 23, no. 1, pp. 194–201, Feb. 2016.

[5] I. Gallimberti, G. Marchesi, and L. Niemeyer, “Streamer corona at an insulator surface,” in *7th international symposium on High voltage engineering*, 1991, pp. 26–30.

[6] M. A. Abdul-Hussain and K. J. Cornick, “Charge storage on insulation surfaces in air under unidirectional impulse conditions,” *IEE Proc. - Phys. Sci. Meas. Instrum. Manag. Educ. - Rev.*, vol. 134, no. 9, pp. 731–740, Nov. 1987.

[7] P. Viegas *et al.*, “Investigation of a plasma–target interaction through electric field characterization examining surface and volume charge contributions: modeling and experiment,” *Plasma Sources Sci. Technol.*, vol. 27, no. 9, p. 094002, 2018.

[8] V. R. Soloviev and V. M. Krivtsov, “Surface barrier discharge modelling for aerodynamic applications,” *J. Phys. Appl. Phys.*, vol. 42, no. 12, p. 125208, 2009.

[9] I. Gallimberti, “The mechanism of the long spark formation,” in *Journal De Physique, Colloquium C*, 1979, vol. 7, pp. 193–250.

[10] A. Küchler, *High Voltage Engineering: Fundamentals-Technology-Applications*. Springer, 2017.

[11] R. Morrow and J. J. Lowke, “Streamer propagation in air,” *J. Phys. Appl. Phys.*, vol. 30, no. 4, p. 614, 1997.

[12] B. Bagheri *et al.*, “Comparison of six simulation codes for positive streamers in air,” *Plasma Sources Sci. Technol.*, 2018.

[13] V. R. Soloviev and V. M. Krivtsov, “Mechanism of streamer stopping in a surface dielectric barrier discharge,” *Plasma Phys. Rep.*, vol. 40, no. 1, pp. 65–77, Jan. 2014.

[14] W. Hua and K. Fukagata, “Influence of grid resolution in fluid-model simulation of nanosecond dielectric barrier discharge plasma actuator,” *AIP Adv.*, vol. 8, no. 4, p. 045209, Apr. 2018.

[15] S. Singh and Y. V. Serdyuk, “Simulations of Nonthermal Electrical Discharges in Air Over Solid Insulating Barrier,” *IEEE Trans. Plasma Sci.*, pp. 1–7, 2018.

[16] R. Marskar, “An adaptive Cartesian embedded boundary approach for fluid simulations of two- and three-dimensional low temperature plasma filaments in complex geometries,” *ArXiv180903745 Phys.*, Sep. 2018.

[17] R. Marskar, “Adaptive multiscale methods for 3D streamer discharges in air,” *Plasma Res. Express*, vol. 1, no. 1, p. 015011, Jan. 2019.

[18] F. Pechereau, J. Jánský, and A. Bourdon, “Simulation of the reignition of a discharge behind a dielectric layer in air at atmospheric pressure,” *Plasma Sources Sci. Technol.*, vol. 21, no. 5, p. 055011, 2012.

[19] G. E. Georghiou, A. P. Papadakis, R. Morrow, and A. C. Metaxas, “Numerical modelling of atmospheric pressure gas discharges leading to plasma production,” *J. Phys. Appl. Phys.*, vol. 38, no. 20, p. R303, 2005.

[20] A. Bourdon, V. P. Pasko, N. Y. Liu, S. Célestin, P. Ségur, and E. Marode, “Efficient models for photoionization produced by non-thermal gas discharges in air based on radiative transfer and the Helmholtz equations,” *Plasma Sources Sci. Technol.*, vol. 16, no. 3, p. 656, 2007.

[21] S. Pancheshnyi, “Role of electronegative gas admixtures in streamer start, propagation and branching phenomena,” *Plasma Sources Sci. Technol.*, vol. 14, no. 4, p. 645, 2005.

[22] A. A. Dubinova, “Modeling of streamer discharges near dielectrics,” TU Eindhoven, 2016.

[23] N. L. Allen and P. N. Mikropoulos, “Streamer propagation along insulating surfaces,” *IEEE Trans. Dielectr. Electr. Insul.*, vol. 6, no. 3, pp. 357–362, Jun. 1999.

Appendix A

Additional surface potential measurements

Here, surface potential measurements at HSR that were not included in the papers or in the main text are shown. The different configurations are summarized in table A.1. Measurements on configuration 4, 7, 6, 9 and 5 shown previously in figs. 5.12a, 5.12b and 5.13 to 5.15 respectively.

Table A.1: Surface potential measurements at HSR: Parameters (see fig. 3.1). g: rod height, b: barrier surface height, l : rod length. r : rod radius. U : applied voltage.

Param.	Configurations								
	1	2	3	4	5	6	7	8	9
g [mm]	60	60	80	15	35	20	10	25	60
b [mm]	40	30	40	5	15	15	5	5	5
l [mm]	590	590	590	260/590	590	590	288	590	590
r [mm]	3.5	3.5	3.5	3.5	3.5/2	3.5/2	2	3.5	3.5
U [kV]	50	50	50	35	$\pm$50	$\pm$50	35	50	65

A.1 Line plots

In fig. A.1, a few more surface potential measurements that were not discussed in the papers or in the main text are included. Although the measurements are statistically spread out, the simulation results are decent approximations of the maximum surface charge.

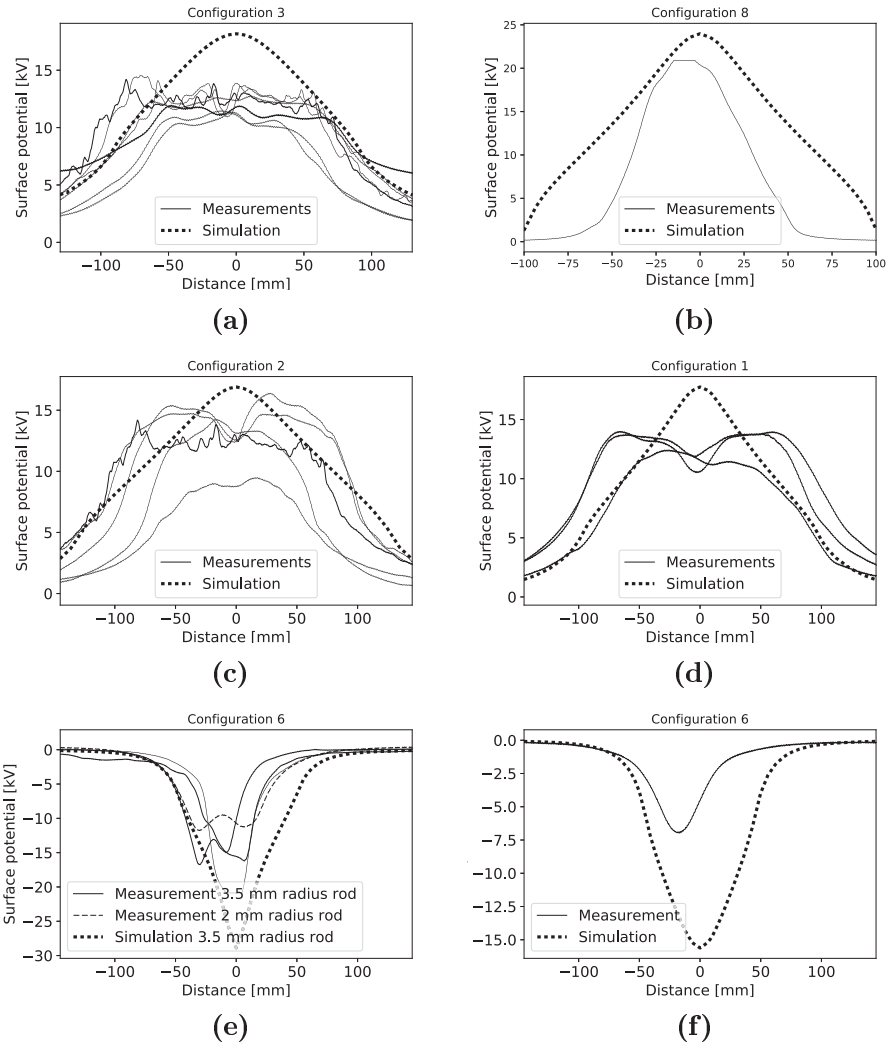

Figure A.1: Additional surface potential measurements (see table A.1 for description of geometries) a) Config 3 b) Config 8 c) Config 2 d) Config 1 e) Config 6 (negative impulse) f) Config 5 (negative impulse)

A.2 2D scans

A few 2D scans are shown here in fig. A.2 to give a qualitative impression of the 2D surface potential distribution. The measurements are taken in a ca. 600x400 mm rectangle (see fig. 3.4b for illustration of the scanning pattern). Each scan took ca. 15 min.

It can be observed that the distribution is relatively symmetrical around the rod position, and that the different geometries give different spread in the surface potential. Sometimes "volcano"-like shape (e.g. fig. A.2c) are seen where back discharges have occurred. A quantitative comparison with simulations is not included here (see fig. A.1 or section 5.2 for quantitative comparisons).

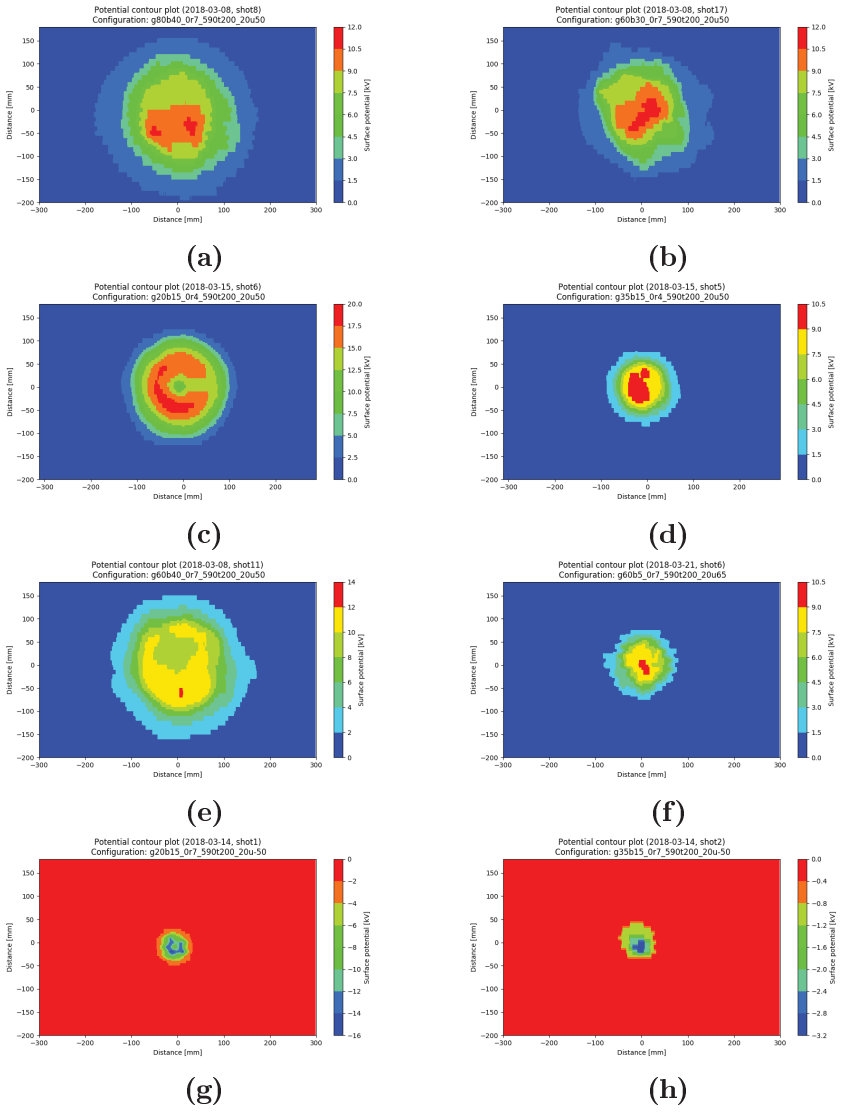

Figure A.2: A few 2D surface scans (see table A.1 for description of geometries) a) Config 3 b) Config 2 c) Config 6 (2 mm rod radius) d) Config 5 (2 mm rod radius) e) Config 1 f) Config 9 g) Config 6 (negative impulse) h) Config 5 (negative impulse)

Appendix B

Signal propagation times in cabling

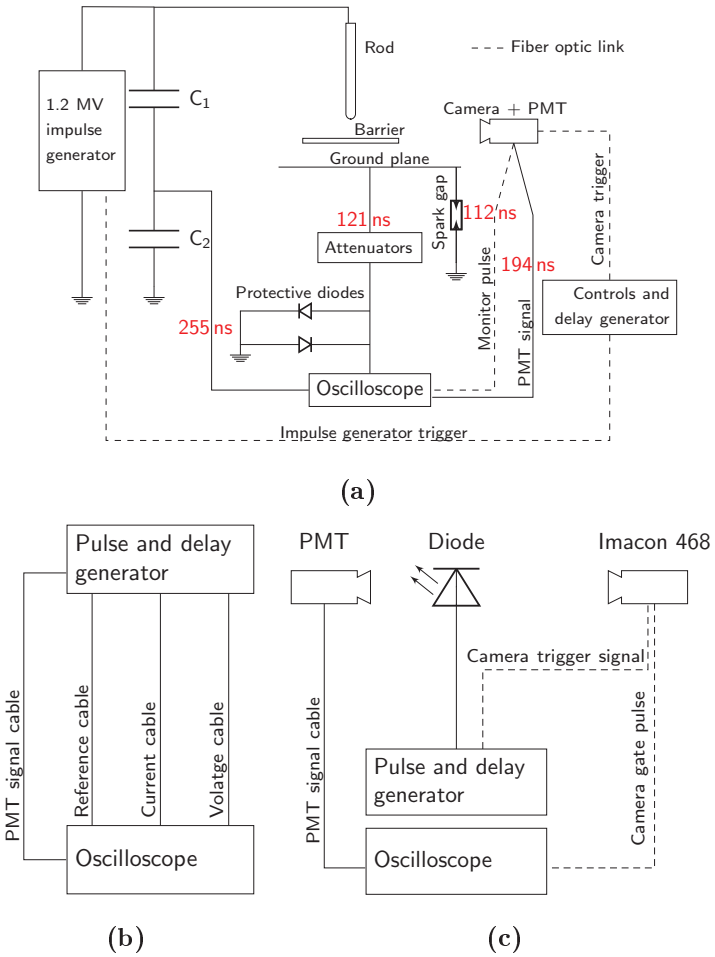

Figure B.1: Signal propagation times in the different cabling to the oscilloscope in the NTNU high voltage lab (see also fig. 3.2). a) To obtain correct timing of current, PMT, voltage and camera gate signals, these delays must be compensated for, for example by prolonging cables or by post-processing the oscilloscope recordings (measured delays in red). In RG-58 signal cables, the signal uses ca. 5 ns per meter cable. b) In this work the propagation times were found with a signal generator, and a reference cable of known length. c) For the camera frames, a fast diode and PMT was used to find the delays.